

TEMPORAL LIMITS ON THE HABITABILITY OF ROCKY WORLDS

by

ELIZABETH ANNE FRANK

B.S., Rensselaer Polytechnic Institute, 2009

A thesis submitted to the  
Faculty of the Graduate School of the  
University of Colorado in partial fulfillment  
of the requirement for the degree of  
Doctor of Philosophy  
Department of Geological Sciences  
2014

This thesis entitled:  
Temporal limits on the habitability of rocky worlds  
written by Elizabeth Anne Frank  
has been approved for the Department of Geological Sciences

---

Stephen Mojzsis, Thesis Advisor

---

William Bottke, Committee Member

---

Joseph Smyth, Committee Member

---

Shijie Zhong, Committee Member

Date\_\_\_\_\_

The final copy of this thesis has been examined by the signatories, and we find that both the content and the form meet acceptable presentation standards of scholarly work in the above mentioned discipline.

Frank, Elizabeth Anne (Ph.D., Geological Sciences)

Temporal limits on the habitability of rocky worlds

Thesis directed by Professor Stephen J. Mojzsis

The epoch of habitability on a rocky world is dictated by the suite of geological events and processes it experiences. A planet may be habitable for a long stretch of its history, but that period has limits. When is too soon for life to arise on a planet, and when is it too late for it to continue? Limits for habitability on Earth-like planets can be defined by extracting Earth's history from the geochemical record to infer that of the rocky planets lying far beyond the reaches of our solar system.

The Late Veneer was the last recorded impact event capable of melting the Earth's crust—and extinguishing any extant life. Eoarchean ultramafic schists (metakomatiites) from Greenland and Canada show highly siderophile element depletions consistent with a deep mantle that had yet to be fully contaminated by Late Veneer material. Whether it was one impactor or multiple, it is clear that the iteration of life from which we originate must have arisen no earlier than the Late Veneer.

Planetary accretion stymies the emergence of life, but geophysics might provide its eventual demise. Plate tectonics operates on Earth as a globate climate moderator, keeping Earth's surface temperate. Geological activity is maintained largely by the long-lived, heat-producing radionuclides  $^{40}\text{K}$ ,  $^{232}\text{Th}$ ,  $^{235}\text{U}$ , and  $^{238}\text{U}$ , whose concentrations decline as Earth ages. Eventually, these isotopes will no longer be able to provide the heat required for mantle convection, and plate tectonics will shut down, calling into question Earth's ability to maintain habitability on a global scale.

Here, the Late Veneer is proposed for the first time as a hard constraint for when life could have arisen on Earth, and age is shown to be a key player in the long-term thermal regimes of conventionally defined Earth-like exoplanets. Provided with limits on the reign of life on Earth, the habitability of rocky exoplanets can be evaluated: those that are too young will still be experiencing surface-sterilizing impact events, while those that are too old will possess cool mantles incapable of sustaining the geological activity that supports the only life we know of in the Universe.

*for Mom and Dad*

# CONTENTS

Title page.....	i
Signature page.....	ii
Abstract.....	iii
Dedication.....	v
Contents.....	vi
<b>Chapter 1: Introduction .....</b>	<b>1</b>
1.1. Galactic chemical foundations for a habitable solar system.....	3
1.1.1. Setting the galactic stage .....	3
1.1.2. From gas cloud to rocky planet .....	5
1.1.3. The tail end of accretion .....	6
1.2. Earth: Geochemistry of a habitable planet .....	9
1.2.1. Compositions in the solar system .....	9
1.2.2. Differentiating the Earth .....	12
1.2.3. Radiogenic heating.....	14
1.2.3.1. Radioactive decay .....	14
1.2.3.3. Long-lived species.....	17
1.2.4. Highly siderophile elements .....	20
1.3. Exoplanet geochemistry .....	21
<b>Chapter 2: Radiogenic heating trends in cosmochemically Earth-like planets .....</b>	<b>22</b>
2.1. Introduction .....	22
2.2. Galactic chemical evolution.....	26
2.3. Model.....	28
2.3.1. An analytical approach .....	28
2.3.2. Assumptions .....	29
2.3.3. Relevant equations.....	31
2.4. Results .....	35
2.4.1. Gas mass evolution.....	35
2.4.2. Mass fractions .....	37
2.4.3. Scaling to planets .....	39
2.4.4. Results for solar systems at time of formation .....	44
2.4.4.1. Concentrations .....	44
2.4.4.2. Heating .....	44
2.4.5. Results for solar systems today .....	46
2.4.5.1. Concentrations .....	48
2.4.5.2. Heating .....	48
2.5. Discussion .....	50

2.5.1. Testing against observations.....	50
2.5.2. Heat budgets .....	53
2.6. Conclusions .....	57
<b>Chapter 3: The geochemical record and dynamics of the Late Veneer .....</b>	<b>60</b>
3.1. Geochemistry .....	60
3.1.1. Introduction .....	60
3.1.2. Late Veneer vs. Late Heavy Bombardment .....	64
3.1.3. Samples and analytical techniques.....	66
3.1.3.1 Komatiites as an HSE archive.....	66
3.1.3.2. Eoarchean rocks of komatiite protolith .....	67
3.1.3.2.1. Akilia association: GR9703, GR97M22, GR0019, GR0020, GR0030, GR0031.....	72
3.1.3.2.2. Innersuurtuut: GR04064, GR04065 .....	72
3.1.3.2.3. Nuvvuagittuq: IN05047, IN08016.....	73
3.1.3.2.4. Mafic samples from Nuvvuagittuq.....	73
3.1.3.3. Analytical techniques.....	78
3.1.4. Results .....	78
3.1.4.1. Protolith identification.....	78
3.1.4.2. Highly siderophile elements in komatiites .....	83
3.1.5. Discussion .....	92
3.1.5.1. Tungsten isotope systematics and the Late Veneer.....	92
3.1.5.2. Archean “trickle-down” geodynamics.....	95
3.1.5.3. Late Veneers beyond Earth.....	97
3.1.5.4. Alternate hypotheses to the Late Veneer .....	99
3.2. Dynamical modeling .....	101
3.3. Conclusions .....	105
<b>Chapter 4: An integrated perspective on habitability .....</b>	<b>110</b>
4.1. Space-limited habitability in the solar system .....	110
4.2. Time-limited habitability in the cosmos .....	114
4.2.1. Its rise .....	114
4.2.2. Its demise.....	115
4.3. Habitability case study: H <sub>2</sub> -oxidizing biomass on Europa .....	118
4.3.1. Introduction .....	119
4.3.2. Heat Production.....	121
4.3.3. Hydrothermal vents .....	123
4.3.4. H <sub>2</sub> -oxidation .....	126
4.3.5. Discussion and conclusions .....	128
4.4. Earth-like exoplanets .....	130
4.5. Galactic habitability.....	131
4.6. Concluding remarks.....	132
<b>Chapter 5: Future directions.....</b>	<b>135</b>
5.1. Radiogenic heating in exoplanets.....	135
5.2. The Late Veneer.....	136

References .....	139
Appendix 1: Running the galactic chemical evolution calculations .....	161
Appendix 2: Useable thermal data for exoplanet models.....	166
List of tables.....	ix
List of figures.....	x



## LIST OF TABLES

### **Chapter 2: Galactic chemical evolution and planetary geochemistry**

- 2.1. Constants assumed in the model
- 2.2. Chemical abundances assumed for the bulk solar system and Earth's mantle
- 2.3. U/Th observations and age estimates of ancient, metal-rich halo stars

### **Chapter 3: The geochemistry and dynamics of the Late Veneer**

- 3.1. Whole rock geochemistry for the ultramafic samples.
- 3.2. Whole rock geochemistry for the mafic samples
- 3.3. HSE data for all samples
- 3.4. Normalized HSE data for all samples
- 3.5. HSE concentrations in the Earth, meteorites, and other planetary bodies

### **Chapter 4: An integrated perspective on habitability**

- 4.1. Comparison of biomass calculations for Earth and Europa from Lowell and DuBose (2005) and this study

## LIST OF FIGURES

### Chapter 1: Introduction

- 1.1. Mass delivered by the Giant Impact, Late Veneer, and Late Heavy Bombardment
- 1.2. CI-normalized mantle abundances of selected trace elements
- 1.3. Earth's declining radiogenic heat production with time

### Chapter 2: Galactic chemical evolution and planetary geochemistry

- 2.1. Schematic showing the flow of mass through the galactic disk
- 2.2. The evolution of mass in the galactic disk with time
- 2.3. Mass fraction evolutions of several major mantle-forming elements in the galactic disk
- 2.4. Mass fraction evolution of Fe in the galactic disk
- 2.5. Mass fraction evolution of  $^{40}\text{K}$  in the galactic disk
- 2.6. Initial concentrations of  $^{40}\text{K}$ ,  $^{232}\text{Th}$ ,  $^{235}\text{U}$ , and  $^{238}\text{U}$  in cosmochemically Earth-like mantles
- 2.7. Initial heat productions of  $^{40}\text{K}$ ,  $^{232}\text{Th}$ ,  $^{235}\text{U}$ ,  $^{238}\text{U}$ , and their total
- 2.8. Heat production for 4.5 Gyr in planets that formed 0, 4, 8, and 12.5 Gyr after Galaxy formation
- 2.9. Concentrations of  $^{40}\text{K}$ ,  $^{232}\text{Th}$ ,  $^{235}\text{U}$ , and  $^{238}\text{U}$  in exoplanets today as a function of their age
- 2.10. Current heat production in exoplanets as a function of their age.
- 2.11. Nucleocosmochronology data superimposed with the predicted U/Th ratio evolution
- 2.12. Si/Fe mass fraction ratio over galactic history.
- 2.13. Total heat output from radiogenic heating as a function of a planet's mass and core size

### Chapter 3: The geochemical record and dynamics of the Late Veneer

- 3.1. Schematic of the late accretion scenario proposed by Maier et al. (2009)
- 3.2. Timeline showing the Late Veneer in the context of early solar system history
- 3.3. Chromium abundances in samples
- 3.4. 2D kernel density plots for komatiite identification
- 3.5. Normalized trace element concentrations of mafic samples
- 3.6. Normalized concentrations of Pt and Ru in komatiites over time

- 3.7. Linear regressions of Pt and Ru concentration trends in komatiites
- 3.8. HSE abundances normalized to primitive mantle
- 3.9. HSE abundances normalized to CI

#### **Chapter 4: An integrated perspective on habitability**

- 4.1. Number of exoplanet host stars as a function of age and the putative heat production of their rocky planets
- 4.2. A hypothetical euroman hydrothermal vent system from McCollom (1999)
- 4.3. Heat production over time from  $^{26}\text{Al}$

# Chapter 1: Introduction

The initial properties and subsequent evolution of a planet are set by indelible processes that operated long before its solar system's building blocks of gas and dust condensed from the source cloud. Galaxies, solar systems, and planets are not fixed entities: after they form, they evolve both physically and chemically. While many studies have explored the relationships between galaxies and solar systems, and solar systems and planets, little attention has been paid to the effects of galactic evolution on planets. This is not surprising, as the two systems operate on vastly different orders of scale in terms of both size and time. Nonetheless, integrating the three scales of processes makes sense as the suite of detected but otherwise poorly understood "exoplanets" continues to expand.

The primary goal of these exoplanet observations is to hunt for the elusive Earth-like world, where "Earth-like" is conventionally defined as such in terms of mass, radius, and the planet's location relative to its host star's habitable zone. Given that our singular sample of Earth-based life limits our imagination for other plausible life forms, it is prudent to focus on those planets that are most conducive to the development of life like ours. I will argue, however, that to solely consider the physical properties of a planet is insufficient and that the

chemistry of a planet should be taken into account as well.

Simultaneously, we must explore what is known about life on Earth in the context of geological history since it hosts the only known example of a biosphere. Given that rocky planets provide the platform for life, understanding their geological evolution is key to evaluating their likelihood for supporting hospitable environments over geologic timescales (i.e., billions of years). As the only planet known to support life—and the most accessible to study—I will consider Earth as a baseline for a geochemically habitable world. Furthermore, in order to fully evaluate habitability, we must consider it in both time and space. By peering into the past through geochemical signatures recorded in some of the most ancient rocks on Earth, I have explored the nature of a bookend event termed the “Late Veneer” that I argue provides a minimum constraint for when life—or at least our iteration of it—could have arisen.

The work described herein presents both a top-down and bottom-up approach to the exploration of the geochemistry of habitable planets in general and silicate-metal worlds like our own in particular. I have used both Earth-based data and galactic chemical evolution models to predict exoplanet geochemistry and used among ancient mantle-derived rocks on Earth to infer events that brought Earth to its present state. In this dissertation, I will report the results of my work, which addresses four main questions:

- (1) How does galactic chemical evolution manifest itself in the geochemistry and heat production of rocky exoplanets?
- (2) What can the geochemical record of Earth’s mantle tell us about temporal bookends for its habitability?
- (3) How does the surface chemistry of an icy planetary body inform us about its formation and evolution?

- (4) What implications do the answers to the above questions have for understanding the requirements and limits of habitability?

Tackling these problems has led me to integrate multiple fields into a holistic interpretation of the importance of planetary geochemistry to habitability.

## **1.1. Galactic chemical foundations for a habitable solar system**

### **1.1.1. Setting the galactic stage**

The chemical composition of the universe is not static. Three minutes into its existence, the baryonic matter of the universe was composed exclusively hydrogen, helium, and some lithium (e.g., Copi et al., 1995); the remaining "metals," a term conventionally used by astronomers to describe elements heavier than helium, were generated in the intervening 13.7 Gyr (Spergel et al., 2003), primarily via stellar nucleosynthesis. Beryllium and boron can be generated through cosmic-ray interactions with interstellar atoms, while the remainder of elements can attribute their abundances to stars, where new elements are generated from the pre-existing nucleons of lighter elements.

Galaxies emerged—and continue to emerge—from the gas created by the Big Bang. Our Galaxy, the Milky Way, is classified as a spiral bar galaxy having a spheroidal central bulge and an estimated four arms circling it in a disk, with the solar system residing on the Orion Arm approximately 8 kpc away from the galactic center (Reid, 1993). The disk is enveloped by a spheroidal halo of old stars and globular clusters. Like the bulge, star formation no longer occurs in this region, as little gas remains. As such, all active star formation—and solar system formation—is currently occurring in the disk (Madau et al., 1998).

While the initial abundances of and ratio between H and He were set during Big Bang nucleosynthesis, the majority of metals have been generated in stellar nucleosynthesis and supernova nucleosynthesis. Stellar nucleosynthesis occurs in the cores of stars. As they age, stars "burn" the elements from which they formed, generating heavier species. Upon depleting their fuel, they explode, ejecting their mass back into the ISM and augmenting its metallicity. Major rock-forming elements—O, Si, Al, Mg, Ca, Fe—are made during hydrogen fusion and helium burning, but any nuclides heavier than  $^{56}\text{Fe}$  hit a bottleneck wherein the maximum binding energy of an atom's nucleus is reached and the nucleosynthetic reactions become endothermic rather than exothermic. As a result of this bottleneck, elements heavier than Fe cannot be generated in the core of stars. Rather, they require high-energy environments such as Type Ia supernovae, in which a white dwarf in a binary system pulls mass from its accompanying star, raising its core temperature enough for carbon fusion to begin (Hoyle and Fowler, 1960). This kickstarts runaway nuclear fusion, r-process nucleosynthesis, and s-process nucleosynthesis. In r-process (rapid-process) nucleosynthesis, seed nuclei at the Fe peak experience a series of neutron captures that occur rapidly relative to the rate of decay if the nucleus is unstable; in s-process (slow-process), neutron capture occurs slowly relative to decay (e.g., Cowan et al., 1991).

There are multiple flavors of nucleosynthesis, but the outcome is the same: with time, galaxies become increasingly enriched in heavy elements. The quantification of that evolving enrichment is termed galactic chemical evolution (GCE). The continued increase of galactic metallicity is reflected in the composition of solar systems and the planets that form in them. This relationship has been relatively poorly studied in cosmochemistry and is completely absent in discussions of exoplanets. I address this problem in §2 by integrating a rigorous

analytical GCE model (Clayton, 1985) with geochemical and cosmochemical constraints to explore the chemical effects of time on exoplanets.

### **1.1.2. From gas cloud to rocky planet**

Solar systems are derived from molecular clouds, regions of the interstellar medium (ISM) with sufficient gas densities to permit molecule formation. If the internal outward pressure of a region of the cloud fails to counterbalance its gravity, that segment will collapse under its own mass. Through the conservation of angular momentum, it will form a rotating circumstellar disk around a protostar. There, dust grains will clump together to form increasingly large particles, eventually forming planets (e.g., Weidenschilling, 1977). For our solar system, this process began  $4568.5 \pm 0.5$  Ma, as recorded in the oldest components of the calcium aluminum-rich inclusions (CAIs) found in chondritic meteorites (Bouvier and Wadhwa, 2010).

While constructing large particles from smaller ones may sound straightforward, it is actually quite complex, challenging formation modelers to reconcile the mass, chemistry, and location of each planet (e.g., Bond et al., 2010). At the horizontal center of the protoplanetary disk is the midplane, upon which dust and gas above and below will condense during the first phase of planet formation. The dynamical leap from micron-size dust grains to planetesimal-size bodies remains a long-standing problem in planetary science, however. When the accreting particles are less than a centimeter in size, they are bound by electrostatic forces; at larger scales, gravity takes over. What happens at the confluence of the two forces is a modeling challenge complicated by the gas drag drawing material into the protostar (Weidenschilling, 1977). At a transition size of approximately a meter, there appear to be more forces breaking particles apart (collisions, gas drag) than keeping them together



(electrostatic forces, self-gravity; Weidenschilling, 1977). Recent models accounting for disk turbulence appear to overcome the "meter-size barrier problem" to make planetesimals on the order of 100 km in the second phase of planet formation (Cuzzi et al., 2008; Johansen et al., 2007).

Subsequent runaway growth of the planetesimals into planetary embryos composes the third stage. As the embryos grow larger, they accrete planetesimals more rapidly (Greenberg et al., 1978), reaching lunar to martian masses ( $\sim 1000$  km in diameter) within  $10^5$  to  $10^6$  years (Morbidelli et al., 2012). Runaway growth ceases when the embryos become large enough to ramp up the velocities of the remaining planetesimals. This period is called "oligarchic growth" (Kokubo and Ida, 1998). In the last phase of coalescence, no gas or dust remains in the disk, and the burgeoning planets sweep up most of the remaining planetesimals (Chambers, 2004). During this period, resonances of the planetesimals with large planets (i.e., Jupiter) rapidly increased their eccentricities, ejecting some from the asteroid belt—which is known to be depleted in mass—into the Sun, outside the solar system, or into the inner region occupied by the less eccentric and slower moving embryos (Petit et al., 2002). By no later than 100 Myr, the planets completed accretion (Chambers, 2004).

### **1.1.3. The tail end of accretion**

Accretion did not end suddenly, however, but rather tailed off, sometimes spiking with discrete impact events from lingering planetesimals. There are two endmember scenarios for this decline as ascertained by the lunar impact history: (1) a smooth exponential decrease in impactor flux with time (Neukum and Wilhelms, 1982) and (2) a much more rapid drop with a cataclysmic impact spike 3.8 to 4.1 Gyr ago, termed the "lunar cataclysm" or more commonly, Late Heavy Bombardment (e.g., Tera et al., 1974). Morbidelli et al. (2012)

reviewed the history of the controversy between different scenarios and modeled the impact flux on the Moon, calibrating the results to existing dynamical, geochemical, and crater density constraints. The authors point out that Neukum and Wilhelms (1982) assumed particular values for poorly constrained parameters such as the age of Nectaris Basin on the Moon and the crater density of the lunar highlands. On the other hand, while many studies corroborate the lunar cataclysm hypothesis, there are uncertainties as to whether the required planetesimal population was actually present at that time (Fassett et al., 2012). The integrated model of Morbidelli et al. (2012) proposed an intermediate trend, showing a "sawtooth"-shaped impact flux decline with a muted spike 4.1 to 4.2 Gyr ago that itself declined smoothly.

Whatever the trend was, some impacts had more lasting effects on the planets than others. The leading hypothesis for the origin of the Moon requires that one of those stray planetary embryos, a Mars-sized body  $\sim 10\%$  of Earth's mass dubbed "Theia," possessed a metastable orbit that resulted in its Earth-crossing and eventual collision with the nascent Earth (e.g., Canup and Asphaug, 2001) between 30 and 100 Myr after solar system formation (Jacobson et al., 2014; Rudge et al., 2010). The event, referred to as the Giant Impact, resulted in a debris disk of the shattered Theia and some of Earth's mantle that together reaccreted to form the Moon (Canup, 2008, 2004). This widely accepted scenario is able to reconcile many physical observations about the Earth-Moon system, including its angular momentum, their masses, and the Moon's apparent Fe depletion (Canup, 2008, 2004). Conceptually, it also explains why the Earth and Moon have identical O isotope ratios (Wiechert et al., 2001), either due to isotopic equilibration in the debris disk and Earth's post-impact atmosphere (Pahlevan and Stevenson, 2007) or an impactor with an identical O ratio as the Earth. Complicating the story, however, the impact simulations of Canup (2008, 2004) show that most Moon-forming material in the debris disk actually derives from the impactor,

presenting a hurdle to the idea of O isotope equilibration between Earth's mantle and the impactor. An alternative impact model showing that most of the Moon derives from Earth's mantle may solve this problem (Ćuk and Stewart, 2012). Despite the challenges in reconciling dynamics and geochemistry, the Giant Impact hypothesis remains the most viable scenario for the formation of the Moon.

Even more mysterious than the Giant Impact is the postulated Late Veneer. There exists an excess of highly siderophile elements (HSE; see §1.2.4) in Earth's mantle relative to what is expected following core formation (Chou, 1978; Kimura et al., 1974). That they are in chondritic relative proportion points toward an extraterrestrial explanation requiring an impactor  $\sim 0.5\%$  of Earth's current mass, assuming CI composition (Chou, 1978; Walker, 2009). This event would have occurred after the Giant Impact, which disrupted the core, resetting any HSE signature in the mantle; simultaneously, it must have occurred prior to the formation of lingering evidence of the first continental crust, the oldest of which is a ca. 4.37 Ga zircon from the Narryer Gneiss Complex in Western Australia (Harrison, 2009; Valley et al., 2014). Dynamical models of the solar system at that time indicate that there was indeed enough material remaining in planetesimals to provide the needed mass (Bottke et al., 2010). While the Moon as well as other rocky bodies likewise show HSE enrichments (Day, 2013), the scale of the enrichment relative to Earth's deviates strongly from the standard Earth:Moon impactor flux ratio of  $\sim 20$  (Bottke et al., 2007), being closer to  $\sim 1200$ . Hence, a stochastic single impactor was ruled the most likely explanation (Bottke et al. 2010). The evolution of the Late Veneer HSE signature in Earth's mantle and the nature of the impact are explored in §3.

The lunar cratering record shows that the Late Heavy Bombardment (LHB) delivered approximately 0.003% of Earth's current mass (Hartmann et al., 2000; Ryder et al.,

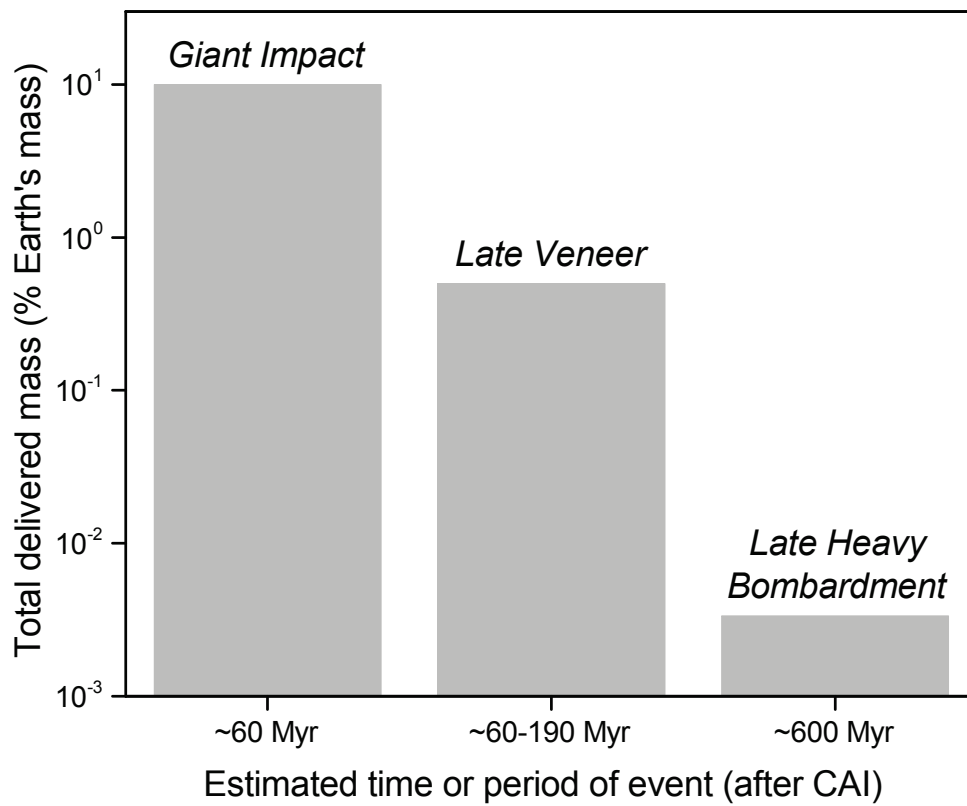
2000), far less than that delivered during the Late Veneer. Radiometric ages of Apollo impact melt samples show that most ages cluster between 3.8 and 4.1 Ga (Tera et al., 1974), suggesting widespread melting during this period. While the Late Veneer on Earth is likely to have been a stochastic event with one or several large impactors, the LHB has been tied to planetesimals scattered from the asteroid belt during giant planet migration (Gomes et al., 2005). The very different timings and mass deliveries of the Giant Impact, Late Veneer, and Late Heavy Bombardment are illustrated in **Figure 1.1**. Whatever accretion's overarching trend might be—exponential, spiked, sawtoothed—it clearly does not have a hard deadline.

## **1.2. Earth: Geochemistry of a habitable planet**

### **1.2.1. Compositions in the solar system**

The bulk chemistry of the solar system, which is measured using the nearly identical compositions of the solar photosphere and carbonaceous chondrites excluding volatiles (Anders and Grevesse, 1989; Lodders, 2003), largely matches the composition of the molecular cloud from which it formed. On the solar system scale, a radial compositional gradient occurs during planet formation based on species volatility, which can be quantified by condensation temperatures (Dodson-Robinson et al., 2009), though heterogeneities due to turbulence complicate this simple picture (Cuzzi et al., 2008; Johansen et al., 2007). Volatile species are unable to condense at the relatively high temperatures present near the young star, creating the "snow line" at approximately 2.7 AU, beyond which water can condense as ice (Hayashi, 1981). It is in these distant regions that the giant planets and ice giants are able to retain gaseous envelopes of H and He, but the inner planets are left with solid surfaces devoid of the most volatile species.

**Figure 1.1.** Mass delivered by the three main impact events in early Earth history for which there are still records.



The asteroid belt, within which lies the snow line, has proven itself in recent years to be more diverse and complex in its population than originally thought. The discovery of a population of so-called "main-belt comets" has blurred the line between asteroids and comets (Hsieh and Jewitt, 2006). These main-belt comets have asteroid-like orbits but show comet-like comae and tails, indicating the presence of volatile species not seen on the archetypical asteroid. Although the presence of ice on those bodies was a surprise, 1 Ceres, the first asteroid ever discovered, has long been known to have a water-ice crust atop its rocky mantle, perhaps with an iron core (McCord and Sotin, 2005; McCord et al., 2011). Based on density estimates, it may be up to 25 wt% water (McCord and Sotin, 2005 and references therein), and Earth-based observations strongly suggest the presence of minerals known only to be the products of hydrothermal alteration (Milliken and Rivkin, 2009; Rivkin et al., 2006). This icy anomaly in the asteroid belt will be further explored during the *Dawn* spacecraft's upcoming approach in early 2015. Predictions for putative early water/rock interactions linked to formation scenarios are presented in §4.

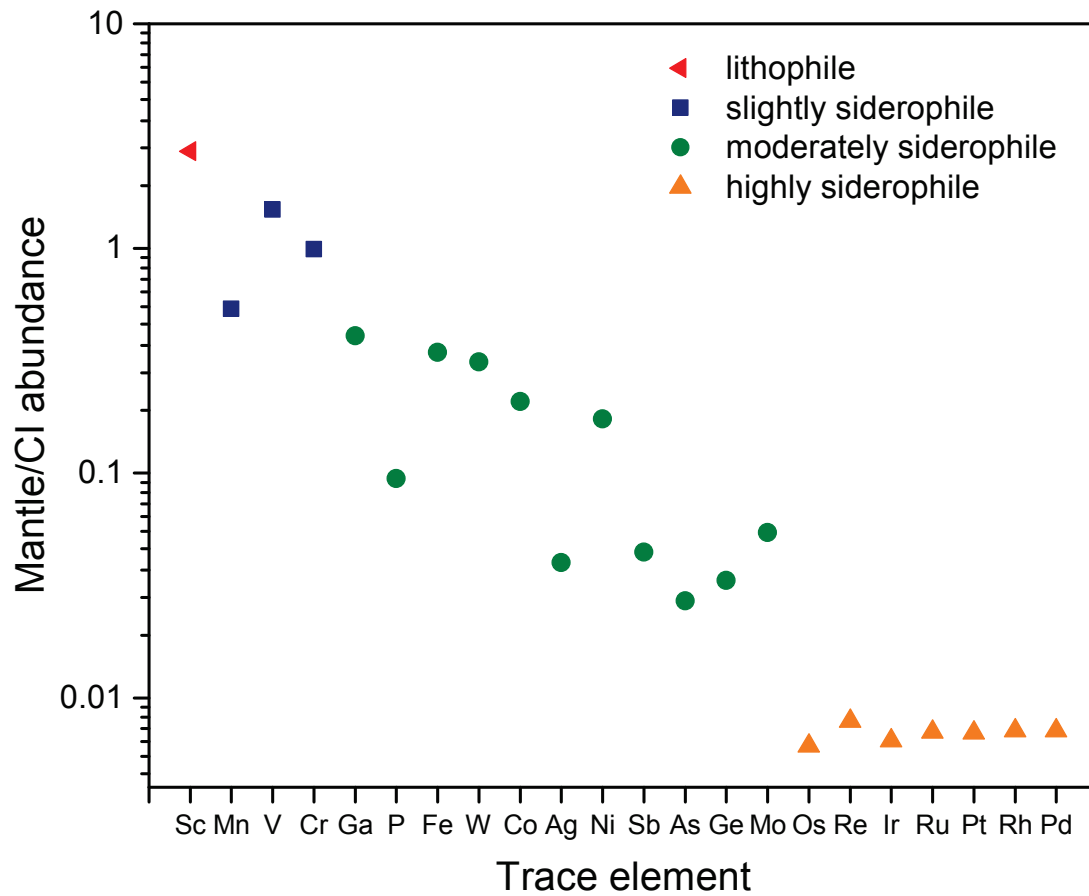
While there is a clear delineation in composition between the rocky and gaseous planets, there is no distinct radial chemical gradient across the inner solar system itself, implying that the region experienced significant radial mixing during solar system formation (Palme and O'Neill, 2003). Without direct deep mantle and core samples, it is an insurmountable challenge to definitively determine the bulk composition of the Earth, but best guesses have been made. Most commonly, carbonaceous chondrites, primitive solar system materials that match the solar photosphere excluding volatiles, have been used as an estimate for Earth's bulk composition. Palme and O'Neill (2003) pointed out that by assuming Earth has a CI composition, subtracting out the Fe, Ni, and S in its core leaves a bulk silicate Earth (BSE) comparable in composition to rocks known to come from the upper mantle.

This assumption, however, is not universally agreed upon. Drake and Righter (2002) note that there is no known reservoir that entirely matches the Earth in chemistry, including CI chondrites. They evaluated different chemical suites and systems in the Earth, comparing the major element, O and Os isotope, noble gas, and D/H compositions from Earth, Mars, primitive meteorites, and comets, coming to the conclusion that Earth must have formed from some unsampled reservoir of "Earth chondrite" or "Earth achondrite" composition. An alternate option is enstatite chondrites, which share the O isotope ratios of the Earth-Moon system (Javoy et al. 2010), but again, this solution is not universally accepted due to other elemental and isotopic inconsistencies (Fitoussi and Bourdon, 2012). The precise chemistry of the building blocks that made the Earth remains a mystery.

### 1.2.2. Differentiating the Earth

A nascent rocky planet's geochemical and geophysical evolution is dictated by the chemical behavior of the elements and isotopes that compose it. Species fractionate in a particular reservoir in a planet—core, mantle, crust, hydrosphere, atmosphere—based on their chemical proclivities. Lithophile ("rock-loving") elements preferentially go into rock, siderophile ("iron-loving") elements fractionate into metal phases, and volatile species have low melting points that make them unstable unless bound within a mineral's crystal structure (Goldschmidt, 1954). The post-differentiation structure of a planetary body is dictated by these behaviors and the conditions (temperature, pressure, mass, relative abundances of the elements) of its formation. **Figure 1.2** shows the behavior of selected lithophile, slightly siderophile, moderately siderophile, and highly siderophile elements in Earth's mantle relative to undifferentiated CI chondrites.

**Figure 1.2.** Abundances of selected elements in Earth's mantle (Palme and O'Neill, 2003) relative to CI chondrites (Anders and Grevesse, 1989). The more siderophile the element, the more strongly it is depleted in Earth's mantle by core formation.





After it accretes, a terrestrial planet will experience an internal redistribution of its elements depending upon their chemical proclivities. The violent impacts of accretion bring massive amounts of kinetic and potential energy to a burgeoning planet, providing the extreme heat required for core formation. Molten from the heat of accretion, metal droplets will descend through silicate phases to the center of the burgeoning planet, generating a Fe-Ni core possibly populated with another light element (e.g., Wood et al., 2006). Once metal phases and the siderophile elements they contain are sequestered into the core, the planet is left with silicate phases and lithophile species in the remainder, whose composition is referred to as the "primitive mantle." This term is synonymous with "bulk silicate Earth," which refers to the crust+mantle bulk composition, although the mantle is far from homogeneous.

In fact, deviations from the expected geochemical properties of a planet serve as markers of past events, endogenic or exogenic, that it may have experienced. An example of this with anomalous highly siderophile element (HSE) profiles marking the Late Veneer is explored in §3.1. Comparisons of rocks from Earth to Apollo samples and meteorites (lunar, martian, and asteroidal) provide an opportunity to compare and contrast what is known about Earth to other planetary bodies in the solar system, including with the Late Veneer (§3.1.4.3). Both similarities and differences between terrestrial and extraterrestrial samples shed light on how solid bodies form and evolve in the inner solar system and asteroid belt.

### **1.2.3. Radiogenic heating**

#### **1.2.3.1. Radioactive decay**

Not all nuclei are stable. An unstable species, the "parent" isotope, possesses a certain well-defined probability that it will experience spontaneous decay, resulting in a new "daughter" species. On the level of a single atom, radioactive decay is stochastic: precisely if

and when a particular unstable atom will decay is entirely unpredictable. However, given a large enough number of atoms, the rate of decay is constant, denoted by the half-life, which marks the period of time it takes for one half of the original number of atoms to decay.

Radioactive decay is conveniently classified based on the emitted particle(s). Alpha ( $\alpha$ ) decay involves the loss of a He nucleus (i.e., two protons and two neutrons). In beta decay, either an electron is lost ( $\beta^-$  decay) or a positron ( $\beta^+$  decay) is lost. The former is most likely with nuclides with high neutron-to-proton ratios, while the latter is associated with nuclides that have low neutron-to-proton ratios. Electron capture occurs on a slower timescale than both alpha and beta decay. An electron from an inner orbital shell is captured by the nucleus, providing an opposing charge to a proton and creating a neutron in its place. Gamma decay features the loss of a gamma ray and has no effect on the charge or mass of the parent. Finally, in spontaneous fission, a heavy nuclide splits into lighter ones with comparable mass numbers (Krane, 1987).

Of these,  $\alpha$ -decay and  $\beta$ -decay are the decay modes experienced by the isotopes, both short-lived and long-lived, most relevant to solar system and planet processes. While much heat was provided by the energetic impacts that form planetesimals, planetary embryos, and eventually planets, the dearth of large impacts today disqualifies this as an active heat source. Internal heat production following primary accretion occurs exclusively through heat-producing isotopes in planetary mantles. As will be described in §2.1, internal heat production is key to maintaining long-term geologic activity in a planetary body, which in turn is arguably instrumental in maintaining surface environments, global or local, that may be habitable for life. An example of the impact that internal heating, with a focus on the radiogenic contribution, can have on supporting microbial biomass is explored in the case of Europa in §4.3.

### 1.2.3.2. Short-lived species

Of the short-lived, heat-producing radionuclides,  $^{26}\text{Al}$  ( $t_{1/2} = 0.704$  Myr) is the most important for early solar system processes. Originally postulated to be the primary heat source for melting planetesimals (Urey, 1956), it was discovered due to an excess relative to solar values of its daughter nuclide,  $^{26}\text{Mg}$ , in the presolar grains present in carbonaceous chondrites (Clayton, 1975). Aluminum-26 is mainly the product of hydrogen burning or explosive helium burning in novae or supernovae (Clayton, 2003). A curious problem in the formation of  $^{26}\text{Al}$  is the observation that live  $^{26}\text{Al}$  was clearly present at the time the chondrites solidified from the gas of the protoplanetary disk, but the ratio of  $^{26}\text{Al}/^{27}\text{Al}$  (where  $^{27}\text{Al}$  is stable) is higher than that expected from molecular clouds, which take 50 Myr to form from the dilute ISM, well past the lifetime of  $^{26}\text{Al}$  (Meyer and Clayton, 2000). The leading explanation is that there was a late-stage injection of  $^{26}\text{Al}$  and other radionuclides from an exploding massive star just as our solar system was starting to form (Hohenberg et al., 1967; c.f., Shu et al., 1997; Wasserburg et al., 1996).

A product of neutron capture,  $^{60}\text{Fe}$  is another contributor to the early heating of small bodies. As with  $^{26}\text{Al}$ , an excess of its daughter nuclide,  $^{60}\text{Ni}$ , in chondrites led to the prediction of its presence in early solar system bodies. While it produces less heat during decay than  $^{26}\text{Al}$ , it has a longer half-life ( $t_{1/2} = 1.5$  Myr), which means it becomes increasingly important for maintaining high internal temperatures as  $^{26}\text{Al}$  wanes. Mostefaoui et al. (2005) found that the  $^{60}\text{Fe}/^{56}\text{Fe}$  ratio in an ordinary chondrite was higher than that estimated from continuous galactic chemical evolution (Wasserburg et al., 1996) and that like  $^{26}\text{Al}$ , it too must have come primarily from a late supernova injection. The high ratio was also interpreted as evidence that  $^{60}\text{Fe}$  was able to produce enough heat to help induce planetary melting and differentiation and continue to produce heat while sequestered in the burgeoning core, which is consistent with

core formation in planetesimals within 2 to 3 Myr (Mostefaoui et al. 2005). While there are uncertainties about their origin in our solar system, there is no doubt that  $^{26}\text{Al}$  and  $^{60}\text{Fe}$  had a lasting impact on small bodies due to their short but intense heat burst during the first several Myr of solar system history (McSween et al., 2002).

### 1.2.3.3. Long-lived species

Though key to the initial thermal evolution of small bodies, the short-lived, heat-producing radionuclides are insignificant in the long-term evolution of planets, whose duration of formation exceeds the lifetimes of  $^{26}\text{Al}$  and  $^{60}\text{Fe}$ . Rather, rocky planets receive the vast majority of their radiogenic heat through the long-lived isotopes  $^{40}\text{K}$ ,  $^{232}\text{Th}$ ,  $^{235}\text{U}$ , and  $^{238}\text{U}$  ( $^{40}\text{K}$ :  $t_{1/2}=1.25$  Gyr;  $^{232}\text{Th}$ :  $t_{1/2}=14.0$  Gyr;  $^{235}\text{U}$ :  $t_{1/2}=0.704$  Gyr; and  $^{238}\text{U}$ :  $t_{1/2}=4.47$  Gyr). The thermal regime of a planetary mantle, which on Earth manifests itself via plume activity and plate tectonics, is set largely by these species, and the long-term geological activity of a planet depends heavily on the heat production from their decay on timescales of billions of years.

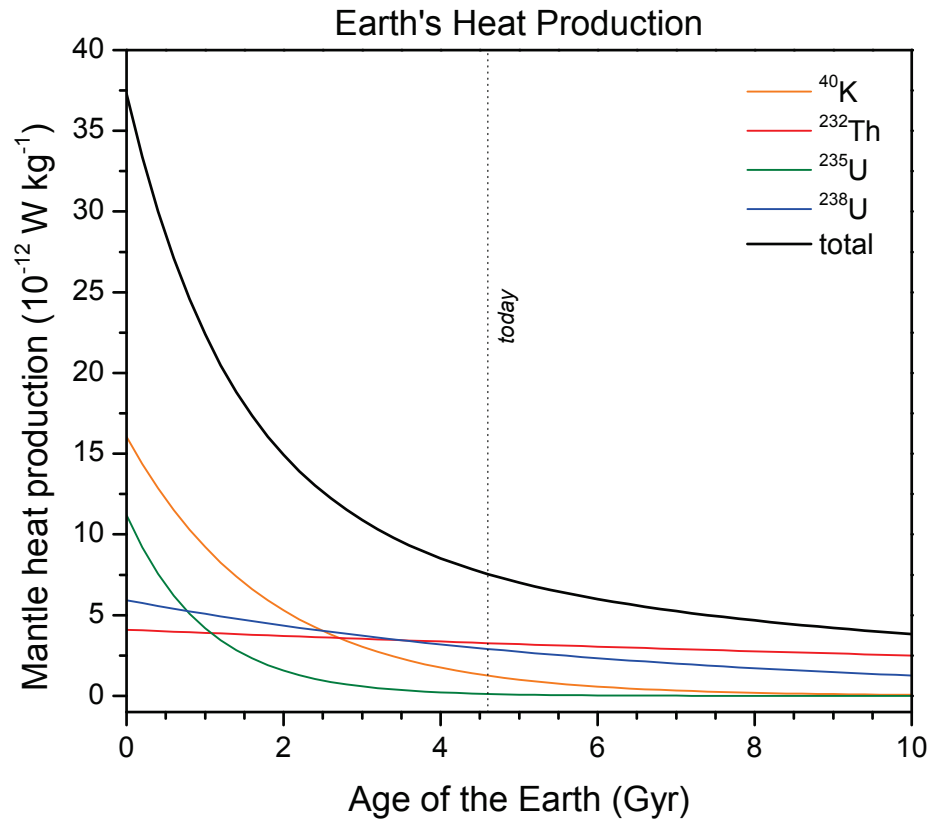
Potassium-40 is the product of oxygen burning and s-process nucleosynthesis, while the other three are pure r-process nucleosynthesis products. Together, the long-lived isotopes contribute significantly to Earth's modern heat budget, complemented by lingering heat from accretion and differentiation (e.g., Richter, 1988). Knowing the exact relative proportion between radiogenic heating and secular cooling remains a challenge. It is quantified by the Urey ratio, which is the contribution of radiogenic heat output relative to the total heat budget of a planet measured through its surface. The Urey ratio is not particularly well constrained, with estimates ranging between 0.21 and 0.74 (Lenardic et al., 2011 and references therein). Correcting for such factors as limited heating from the core and the contributions of secular cooling, one estimate for Earth's present-day radiogenic heat production in the mantle is

$7.38 \times 10^{-12} \text{ W kg}^{-1}$  (Turcotte and Schubert, 2002). Any prediction for radiogenic heat output will serve as a minimum for a planet's total heat budget.

Despite their slow decay, the concentrations of the long-lived isotopes in Earth's mantle have declined significantly over geologic time (**Figure 1.3**). For example, although  $^{235}\text{U}$  was 88 times more abundant at the time of solar system formation (4.568 Ga; Amelin et al., 2002; Bouvier and Wadhwa, 2010) than it is now, it became effectively extinct in Earth's mantle after less than  $\sim 3$  Gyr. This has left the other three isotopes to produce the radiogenic heat that helps sustain Earth's present geological activity. With a half-life comparable to the age of the universe,  $^{232}\text{Th}$  has lost a mere 20% of its original abundance since Earth formed, while  $^{40}\text{K}$  has lost  $\sim 90\%$ . When Earth reaches an age of ca. 10 Gyr, its radiogenic heat production will be  $\sim 15\%$  of what it was at formation. By then,  $^{40}\text{K}$  will no longer be a heat contributor, and  $^{232}\text{Th}$  will continue to dominate heat production as it does today. In as soon as 900 Myr from now, there may no longer be enough heat in Earth's mantle to sustain mobile-lid convection, in which case plate tectonics will shut down (Sleep, 2007).

Radiogenic heating will be a pivotal parameter to geological development of any planet, including those beyond the bounds of our solar system. Over 1500 exoplanet discoveries have been confirmed, though little is known about them besides their orbital location, radius, mass, and inferred density. Observations provide no information on the chemical composition of rocky exoplanets, but information can be gleaned from modeling the chemical evolution of the interstellar medium from which they form. The effects of age and time of solar system formation on exoplanet chemistry is explored in §2 using a galactic chemical evolution model, and the consequences of these effects for habitability are discussed in §5.

**Figure 1.3.** Earth's radiogenic heat production with time. The vertical dashed line shows the present-day heat production.



#### 1.2.4. Highly siderophile elements

As mentioned in §1.2.2, siderophile elements possess a strong affinity for metal. This is the extreme case for the highly siderophile elements (HSE), which include the platinum group elements (PGE: Os, Ir, Ru, Rh, Pt, Pd), Au, and Re. They along with moderately siderophile Fe, Ni, and Co are transition metals that have unfilled high-energy electron shells with unpaired electrons, leading to metal-metal bonding or covalent bonds with acceptors like S (Lorand et al., 2008). During primary accretion, as metallic cores grew in the large differentiated silicate planets, the HSE should have been stripped from their silicate mantles via strong partitioning into metal phases that descended through the mantle and were eventually sequestered into the core. On Earth, they are present at parts per billion (ppb) levels. Despite an obvious affinity for metal, it was recognized early on that the HSE are present in modern basalts and komatiites at concentrations several orders of magnitude higher than those predicted based on simple partitioning behavior (Kimura et al., 1974). With high metal-silicate partition coefficients ( $D_{\text{met/sil}} > 10^4$ ), approximately 99.8% of the PGE should be sequestered into Earth's core (Lorand et al., 2008). However, estimates of the Os, Pt, and Re concentrations in Earth's core suggest that these elements are three to four times more enhanced relative to the Allende CV3 chondrite values and  $10^3$  more than the primitive mantle (Day, 2013). Furthermore, they are present at chondritic relative abundances despite not having identical partitioning behavior. As will be described in §3.1, an extraterrestrial source during a late accretion event, the Late Veneer, provides the best explanation for this phenomenon, recorded by the most ancient mantle-sourced rocks on Earth.

### 1.3. Exoplanet geochemistry

While astronomers have recently developed techniques to measure the composition of giant planet atmospheres (Charbonneau et al., 2009), acquiring the geochemistry of a terrestrial exoplanet will remain a distant dream for the foreseeable future. As the methods to measure atmospheric chemistries are refined, it may one day be possible to detect atmospheres on rocky planets. Some gases may serve as spectral signatures in rocky exoplanet atmospheres that could be used to infer geological activity (Kaltenegger et al., 2010 and references therein) and others could even be indicators of life (Seager et al., 2013). For now, we are left to speculate—and model—their plausible geochemical/thermal/tectonic regimes. In §2, I will utilize an astrophysical model in order to predict the bulk geochemistry and radiogenic heating of "cosmochemically Earth-like" exoplanets.



## Chapter 2: Radiogenic heating trends in cosmochemically Earth-like planets

A planet's bulk geochemistry will dictate in large part its propensity for geological activity. The first step to examining how a terrestrial planet's chemistry is established is to reach back in time and study the composition of the material from which it formed. Here I present predictions of rocky planets' mantle chemistry and radiogenic heating in their mantles as a function of the time that they formed in galactic history.

### 2.1. Introduction

Since the first extrasolar planet orbiting a main-sequence star was verified in 1995 (Mayor and Queloz, 1995), scores more have been discovered, with >1500 confirmed, >3800 considered candidates, and more being added to the roster every day (<http://planetquest.jpl.nasa.gov>). The *CoRoT* (*CO*nvection, *RO*tation, and *planetary* *Transits*) and *Kepler* telescopes have spearheaded the current era of exoplanet discovery. The primary goal of *CoRoT* is to discover exoplanets with short orbital periods, whereas that of *Kepler* is to find rocky Earth-mass worlds in their star's habitable zone; thus far, the suite of finds runs the

gamut from super-Jupiters (e.g., Johnson et al., 2009) to sub-Mercuries (Barclay et al., 2013). Given that *CoRoT* and *Kepler* can directly measure no more than radius, mass, and orbital distance, inferring the atmospheric and geophysical regimes of exoplanets requires modeling, which itself necessitates extrapolations and inferences based on knowledge of our own solar system. Rocky (composed of silicate and metal, also called “terrestrial”) exoplanets in particular have received attention for their potential to be geologically active and thus potentially habitable to alien biomes. In the past several years, there has been a flurry of reports attempting to model the interiors of rocky exoplanets, their thermal histories, and the plausibility of present geological activity (e.g., Foley et al., 2012; Fortney et al., 2007; O’Neill, 2012; Papuc and Davies, 2008; Seager et al., 2007; Valencia and O’Connell, 2009; Valencia et al., 2007, 2006). A focus of these modeling efforts has been to determine the tectonic regimes of the so-called “super-Earths” ( $1-10 M_{\oplus}$ ; Valencia et al., 2006), and in particular, whether these worlds are capable of sustaining plate tectonics.

The geophysical state of a super-Earth or any rocky planet is dictated in part by processes that occur long before its solar system coalesced (§1.1.1). The thermal regime of a planetary mantle, which on Earth manifests itself via plume activity and plate tectonics, is set largely by the long-lived, heat-producing radionuclides that were created during nucleosynthesis and injected into the interstellar medium from which all stars and their planetary systems form. The most important of these isotopes,  $^{40}\text{K}$ ,  $^{232}\text{Th}$ ,  $^{235}\text{U}$ , and  $^{238}\text{U}$ , contribute significantly to Earth’s modern heat budget, complemented by lingering heat from accretion and differentiation (§1.2.3.3). Species half-lives and concentrations as well as other constants used in this work can be found in **Table 2.1**.

**Table 2.1.** Constants assumed in this work.

Constant	Value	Reference
Half-lives (Ga)		
$^{40}\text{K}$	1.25	Turcotte and Schubert (2002)
$^{232}\text{Th}$	14.0	
$^{235}\text{U}$	0.704	
$^{238}\text{U}$	4.47	
Milky Way age (Ga)	12.5	Dauphas (2005)
Solar system age (Ga)	4.56	Amelin et al. (2002), Bouvier and Wadhwa (2010)
Specific heat production (W per kg isotope)		
$^{40}\text{K}$	$2.92 \times 10^{-5}$	Turcotte and Schubert (2002)
$^{232}\text{Th}$	$2.64 \times 10^{-5}$	
$^{235}\text{U}$	$5.69 \times 10^{-4}$	
$^{238}\text{U}$	$9.46 \times 10^{-5}$	
Initial mantle concentrations (ppb)		
$^{40}\text{K}$	463.6	Calculated from Turcotte and Schubert (2002)
$^{232}\text{Th}$	155.0	
$^{235}\text{U}$	16.4	
$^{238}\text{U}$	62.4	
Mantle concentrations today (ppb)		
$^{40}\text{K}$	36.9	Turcotte and Schubert (2002)
$^{232}\text{Th}$	124	
$^{235}\text{U}$	0.22	
$^{238}\text{U}$	30.8	

Despite how significantly Earth’s own heat production has changed with time, exoplanet modelers assume modern Earth, primordial Earth, or chondritic values for the concentrations of the important heat-producing nuclides. This is due to the challenge of having no direct data on the chemistry of rocky exoplanets, and thus, one is forced to make assumptions based on our solar system with the understanding that it may not be representative of the hundreds of billions of others in the Galaxy. Furthermore, most exoplanet models inaccurately include a heat production rate at steady-state rather than one that declines over time. This is important to recognize because while the age of a planet plays a pivotal role in the relative heat contributions of the relevant isotopes, it is equally important to consider their initial concentrations (Gonzalez et al., 2001; Kite et al., 2009) since the ability of a planet to sustain plate tectonics changes with its initial and evolving thermal profile, which in turn affects its resulting surface convective regime (Noack and Breuer, in press). To constrain the initial radiogenic heat production of a planet, it is necessary to turn to galactic chemical evolution (GCE) models that predict the chemical composition of the gas in the galactic disk—and therefore the solar systems and planets that form from it—over the Galaxy’s history. By coupling the chemical evolution of the Galaxy with that of solar systems and their planets, we have made first-order predictions of the  $^{40}\text{K}$ ,  $^{232}\text{Th}$ ,  $^{235}\text{U}$ , and  $^{238}\text{U}$  concentrations in rocky exoplanets within the solar annulus (an annular region centered on the Sun’s orbit in the Galaxy), and in doing so, have generated radiogenic heating estimates for these exoplanets as a function of their age.

## 2.2. Galactic chemical evolution

Astrophysicists have long been faced with the challenge of trying to encapsulate the chemical evolution of the Galaxy into a single cohesive narrative (Burbidge et al., 1957). To address this problem, GCE models were formulated to address how the bulk chemistry of the Galaxy changes in both time and space as old stars perish and new generations arise (Matteucci, 2003). They quantitatively describe how the Galaxy evolves chemically as gas collapses into stars, stars generate metals via nucleosynthesis, and the new elements are then released back into the gas at the end of a star's lifetime. All GCE models share four common components: (i) boundary conditions, such as the Galaxy's initial composition and whether it is an open or closed system; (ii) stellar yields of heavy nuclides produced by nucleosynthesis; (iii) a star formation rate (SFR) and initial mass function (IMF), which describes the distribution of initial masses for a stellar population; and (iv) gas inflows and outflows to the galactic system (Pagel, 1997). Quantitative constraints on GCE models include solar and meteorite compositions derived from observation and direct measurements of solar wind, the solar photosphere, the abundance ratios of the isotopes in primitive meteorites, the metallicity of G-dwarf stars, and galactic abundance gradients (Nittler and Dauphas, 2006). The resulting output is strongly model-dependent given the uncertainties inherent in each component. Operating as they do over colossal length scales for billions of years, nucleosynthetic processes enrich the interstellar medium (ISM) with heavy elements that accumulate and mix into the mass of material that supplies star-forming regions (Cowan and Sneden, 2006).

The effectively instantaneous appearance of heavy elements was due to production in the first generation of massive stars that lived on the order of  $10^6$  years after the Galaxy

formed (Bromm and Larson, 2004), a period of time that was brief compared to the lifetime of the Galaxy. Indeed, a recent discovery of a galaxy that formed 700 Myr after the Big Bang and has a SFR >100 times our galaxy's provides evidence for the rapid heavy element enrichment of galaxies following their formation (Finkelstein et al., 2013). Due to their intrinsic instability as radioactive isotopes, the long-lived, heat-producing nuclides enter the decay process as soon as they are generated. Although it is unclear how the rate of supernova explosions has changed over time, early solar system abundances of the actinides are approximately that expected for near-uniform production since the Galaxy formed (Reeves, 1991; Wasserburg et al., 1996).

The predictions set forth in GCE models have important implications for bulk chemical properties of planets, and so the models must account for the different processes by which elements are generated. Because of the neutron densities required for the r-process to occur, it was originally suggested that this happens in the neutron-dense areas around neutron stars produced in supernovae (Burbidge et al., 1957). Other sites have been proposed such as binary neutron star or black hole mergers, quick low-mass supernova explosions, accretion-induced collapse models, and bubbles or jets produced during supernova explosions (Snedden et al., 2008). In contrast,  $^{40}\text{K}$  is created both during oxygen burning when lighter elements fuse in the cores of massive stars and s-process nucleosynthesis, and it has a different galactic accumulation history than the r-process nuclides (Clayton, 2003; Zhang et al., 2006). These different histories must be taken into account in GCE models.

## 2.3. Model

The initial chemistry of a solar system will reflect the composition of the molecular cloud from which it formed at a given time in galactic history. As such, by modeling the chemical evolution of the ISM, we can model the chemical evolution of stars and their solar systems. G-dwarf stars ( $\sim 0.9$  to  $1.1 M_{\odot}$ ) are not sites of heavy-element nucleosynthesis but have envelopes that match the composition of their source ISM (Nittler and Dauphas, 2006). Inverting this relationship, the composition of the Sun can be used as a fit to the chemistry of the gas from which it formed at solar system formation. Ignoring Li, Be, B, noble gases, and other volatile elements, we can make the implicit assumption that like our own solar system, the composition of bulk solar system materials (i.e., carbonaceous chondrites) reflects that of its star (e.g. Anders and Grevesse, 1989; Lodders, 2003). From this it follows that the bulk silicate material of an extrasolar system should have comparable abundances of the long-lived, heat-producing nuclides to its star as a function of age. This is where GCE models are required.

### 2.3.1. An analytical approach

Given that the scale and complexity of what they describe is vast, GCE models are notoriously difficult to construct. Although there are a number of detailed numerical models (Matteucci, 2003), they must take into account a myriad of processes to describe galactic chemistry. To simplify the approach but maintain the required rigor, Clayton (1985) presented a model that parameterizes galactic infall in such a way that it provides analytical solutions for disk gas mass, total star mass, and metallicity. The Clayton model is a mathematical approximation for those GCE models that do simulate the physical processes at

hand. This approach is advantageous because the parameterization allows for adjustments to the overarching equations in order to fit trends to astronomical observations.

The Clayton model incorporates several simplifying assumptions to streamline the analysis. This includes the instantaneous recycling approximation (IRA), which states that stellar lifetimes are negligible relative to the timescale of gas consumption, and the instantaneous mixing approximation (IMA), which assumes that stellar ejecta are mixed instantaneously in the ISM. Together, these assumptions imply that short-lived massive stars, which have lifetimes on the order of Myr, live, die, and eject their material back into the ISM on timescales so brief relative to the age of the Galaxy that their lifecycles and contributions are effectively instantaneous. Additionally, the initial mass function (IMF), which sets the population distribution of stars, is time-dependent, and the star formation rate (SFR) is set to depend linearly on the gas mass (i.e., the SFR is proportional to the gas mass). While these simplifying principles make the model less complex than other GCE models, the arbitrary parameters allow for this mathematical model to be satisfactorily adjusted to match astronomical observations.

### **2.3.2. Assumptions**

In addition to the assumptions described above that are inherent to the Clayton model, we incorporate several of our own to be conservative in the application of and implications for predictions of the geochemistry of exoplanets:

1. Supernova-driven mixing in the interstellar medium in the Sun's neighborhood occurs on a  $\sim 100$  Myr timescale (de Avillez and Mac Low, 2002). In addition, we expect mixing from shear forces in the differentially rotating galactic disk. The timescale for this mixing is likely to be of the same order of magnitude as the galactic rotation period



in the Sun’s neighborhood,  $\sim 250$  Myr (e.g., Mihalas and Binney, 1981). Thus, within the solar annulus short-lived nuclides may experience inhomogeneous mixing on the timescale of their half-lives, but those of the long-lived radionuclides of interest are sufficiently long that this is not a concern (Huss et al., 2009). In stars in the vicinity of the Sun, Fe shows a radial chemical gradient of roughly  $-0.065$  dex per kiloparsec (Boeche et al., 2013), corresponding to a  $\sim 14\%$  drop in Fe abundance relative to H for every 1 kiloparsec. This suggests radial mixing occurs on a longer timescale than azimuthal mixing. For this reason, we restrict our GCE model to the volume of the solar annulus, which we assign to be several hundred parsecs in width, over which radial distance abundances are fairly constant.

2. The equations are fit to the element and isotope mass fractions reported by Anders and Grevesse (1989) for the solar system at the time of its formation. Thus, linking this to Assumption (1), the composition of all the gas in the solar annulus matches that of our solar system at its formation ca. 4.568 Ga.
3. The galaxy is  $12.5 \pm 0.9$  Gyr old (Dauphas, 2005). This estimate is based on the U/Th ratio in meteorites and comparisons to observations of low-mass stars in the galactic halo, thereby connecting cosmochemical data to astronomical observations.
4. There is no contribution to the metals from infalling halo gas, i.e.,  $z_f = 0$ , where  $z_f$  is the mass fraction of a species in the halo gas (Clayton, 1985). This assumption is necessary because there is little information about what those fractions are. Furthermore, the fractional contribution of radioactive species will not be constant with time due to their decay, adding further uncertainty to any assumptions. Here, the infalling gas is assumed to be metal-free and thus composed exclusively of H and He.

5. The current mass fraction of gas in the solar annulus is 0.2, with the remainder locked in stars, a value consistent with the range 0.15-0.25 estimated from observations of the surface densities of gas, stars, and stellar remnants in the solar neighborhood (Boissier and Prantzos, 1999 and references therein).
6. The predictions for exoplanets only apply to what we term “cosmochemically Earth-like” worlds around other stars, which are those that hypothetically possess the same elemental and isotopic ratios that Earth has relative to carbonaceous chondrites. (A more detailed description of this assumption can be found in §2.4.3.)

### 2.3.3. Relevant equations

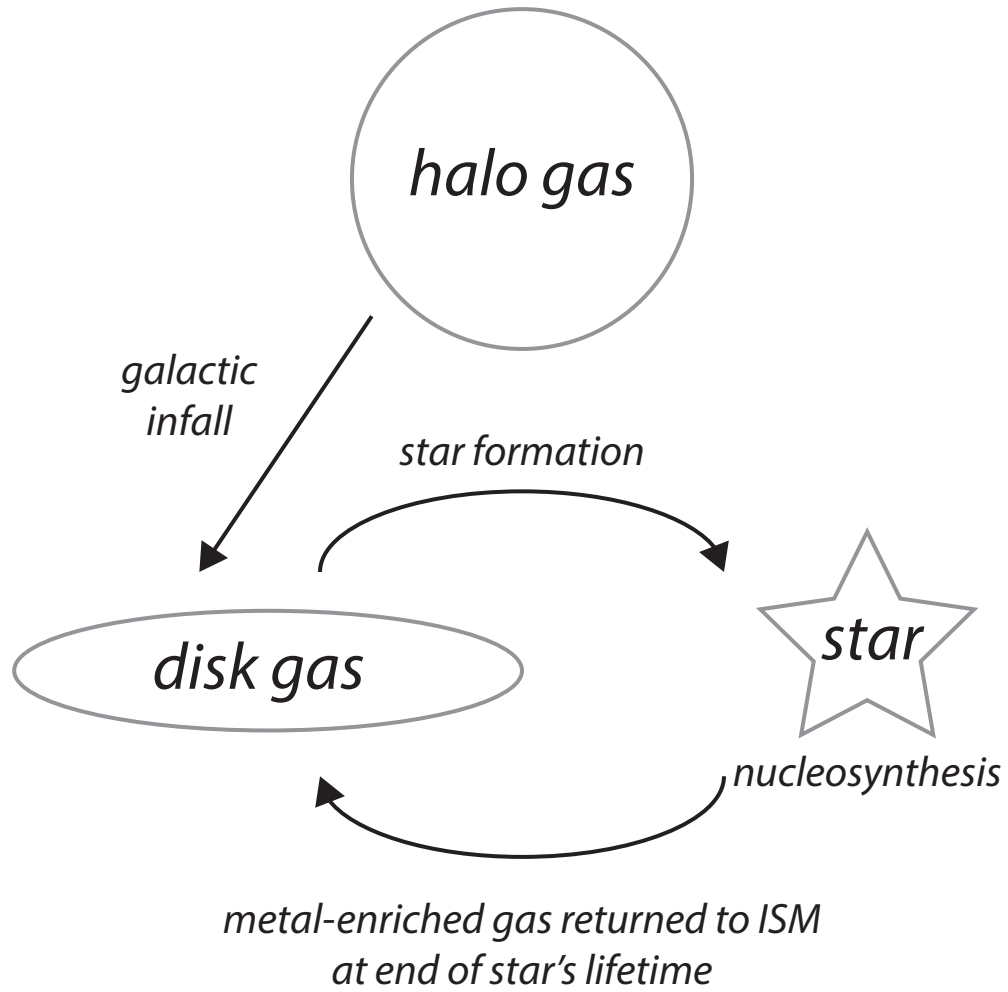
The Clayton model is designed to track how the chemistry of gas in the galactic disk and that of a particular species (isotope, element, or molecule) changes as a function of time. Gas in the disk initially comes from infall from the halo and is subsequently consumed by stars, the rate of which changes over time and is described by the SFR. Some fraction of mass in stars is ejected during supernova explosions and returned to the ISM, but as the galaxy chemically evolves, gas becomes increasingly locked in long-lived, low-mass stars. The evolving mass fraction of a species  $i$  in the disk can be qualitatively described by

(2.1)

$$\frac{\partial(M_G \cdot Z_i)}{\partial t} = - (\text{loss to stars}) + (\text{gain from stars}) - (\text{loss from radioactive decay}),$$

where  $M_G$  is the gas mass of the disk,  $Z_i$  is the mass fraction of a species in the gas, and  $t$  is time since galaxy formation. **Figure 2.1** is a schematic of these linked processes, the net chemical effect of which is metal enrichment in the ISM. The linear relationship between the SFR and gas mass is described by the equation

**Figure 2.1.** Schematic showing the flow of mass through the galactic disk.



(2.2)

$$\frac{\partial M_G}{\partial t} = -\omega M_G + f(t),$$

where  $\omega$  is the rate of mass consumption from star formation (constant for all species) and  $f(t)$  is the infall rate of gas from the galactic halo to the disk (in our case, only the solar annulus). Finally, the standard parameterized model of Clayton (1985) quantifying galactic infall's relationship to gas mass (for our purposes, in the solar annulus) is given by:

(2.3)

$$\frac{f(t)}{M_G(t)} = \frac{k}{t + \Delta},$$

where  $k$  is a positive integer (0, 1, 2, 3) and  $\Delta$  is a parameter with units of time. The parameterized equation for  $M_G(t)$  is

(2.4)

$$M_G(t) = M_G(0) \left( \frac{t + \Delta}{\Delta} \right)^k e^{-\omega t},$$

where  $M_G(0)$  is the initial mass of the solar annulus at the time of formation.

These equations lay the groundwork for computing the evolving mass fraction of a particular species in the gas. Most of the species considered here are only primary, meaning that they can form in the cores of massive stars composed solely of H and He and do not require seed nuclei. Tinsley (1979) recognized that the galactic chemical evolution of  $^{56}\text{Fe}$  received an additional primary boost from Type Ia supernovae, which caused a growing Fe abundance relative to other primary elements after a few Gyr in galactic history. Type Ia supernovae are the thermonuclear explosions of white dwarf stars and their onset is delayed by the time required to evolve the white dwarf progenitor (Matteucci and Greggio, 1986). In contrast, the nuclide  $^{40}\text{K}$  has both primary and secondary components. Secondary species form from seed nuclei and thus require a previous generation of stars to live and die before

adding their metals to the ISM. The yield from stellar nucleosynthesis ( $y_i$ ) for species  $i$  is the sum of the primary ( $\alpha_i$ ) and secondary ( $\beta_i$ ) yield terms, where the total yield of all primary species ( $y_p$ ) is used to calculate the secondary contribution:

$$y_i = \alpha_i + \beta_i y_p. \quad (2.5)$$

Yield is expressed as the mass of species  $i$  ejected from a generation of stars per unit of mass locked up in stellar remnants. When a particular species is purely primary,  $\beta_i = 0$  and  $y_i = \alpha_i$ .

From here the yield is used to calculate the evolution of a species' mass fraction ( $Z_i$ ) in gas over the age of the Galaxy:

$$\frac{\partial Z_i}{\partial t} = y_i \omega - \lambda_i Z_i - (Z_i - Z_{f,i}) \frac{f(t)}{M_G(t)}, \quad (2.6)$$

where  $\lambda_i$  is the decay constant in the case of a radioactive species ( $\lambda_i = 0$  for a stable species) and  $Z_{f,i}$  is the mass fraction contribution of a species from galactic infall. Because the infalling halo matter being considered here is metal-free, in our model we assume  $Z_{f,i} = 0$ . This governing equation leads to individual equations for the mass fraction evolution of stable and unstable species. That for a stable species is described by

$$Z_i = \left( \frac{y_i \omega \Delta}{k + 1} \right) \left[ \frac{t + \Delta}{\Delta} - \left( \frac{t + \Delta}{\Delta} \right)^{-k} \right]. \quad (2.7)$$

In contrast, radioactive species are described by

$$Z_i = (y_i \omega - \lambda_i Z_{f,i}) e^{-\lambda_i t} \left( \frac{\Delta}{t + \Delta} \right)^k I_k(t, \lambda_i), \quad (2.8)$$

where  $I_k(t, \lambda_i)$  is an integral that depends on the assumed  $k$ . For  $k = 1$ , this equation is

$$(2.9)$$

$$I_1 = \frac{1}{\Delta} \left[ e^{\lambda t} \left( \frac{t + \Delta}{\lambda} - \frac{1}{\lambda^2} \right) - \left( \frac{\Delta}{\lambda} - \frac{1}{\lambda^2} \right) \right].$$

The equations outlined above are the analytical solutions for the Clayton GCE model. A thorough derivation of these equations can be found in Clayton (1985), and details of the code used for the computations can be found in **Appendix 1**.

## 2.4. Results

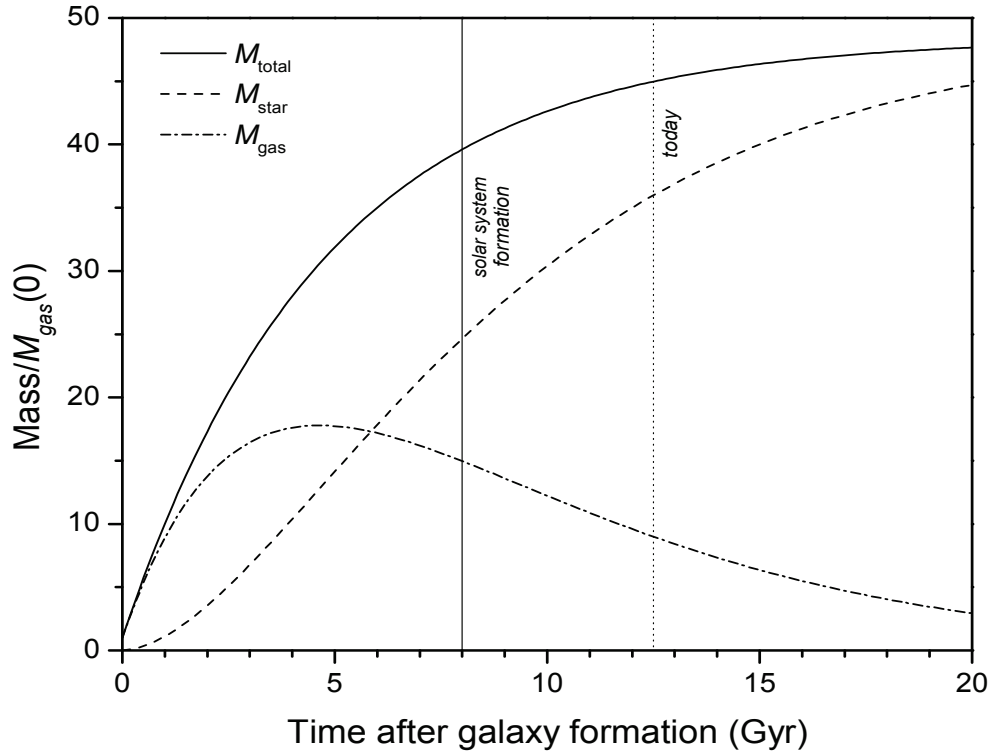
### 2.4.1. Gas mass evolution

The evolution of the gas mass in the Clayton model depends on the choice of the parameters  $k$ ,  $\Delta$ , and  $\omega$ . Following standard practice (e.g., Clayton, 1985), we choose  $k = 1$  and  $\Delta = 0.1$ . From the requirement that the fraction of the mass in the solar annulus be  $\sim 20\%$  (Boissier and Prantzos, 1999), we then determined  $\omega$  to be  $0.211 \text{ Gyr}^{-1}$ . We note that varying  $\Delta$  has little effect on the resulting value for  $\omega$ , while the effect of varying  $k$  is much larger (Huss et al., 2009).

**Figure 2.2** shows the evolution of the total mass (relative to the initial mass  $M_G(0)$ ) of the solar annulus, the mass in gas, and the mass in stars as computed from our choice of  $k$ ,  $\Delta$ , and  $\omega$ . The mass of the solar annulus builds up due to infall. Since the infall rate declines with time, the rate of growth of the total mass also declines. The gas mass initially grows, but as the infall rate declines, gas is increasingly locked up into stars. The gas fraction declines and reaches the 20% value observed today.

Our choice of model parameters agrees with two key observations. First, the choice of  $k = 1$  to 2 is consistent with the G dwarf star age-metallicity relationship (e.g, Clayton, 1985). Second, Madau et al. (1998) showed from observations of distant galaxies that the SFR

**Figure 2.2.** The evolution of mass in the galactic disk (relative to the initial disk mass). Infall from the halo rapidly increases the total mass of the disk but levels off asymptotically. The mass of the gas component peaks early in galactic history, following which disk material becomes increasingly trapped in long-lived stars. The solar neighborhood is currently approximately 20% gas by mass (Boissier and Prantzos, 1999).



peaked at a redshift of approximately 1.5, which corresponds to a time of  $\sim 2$  to  $3$  Gyr after the Big Bang. The peak in the gas mass (and by the proportionality of this quantity to the SFR) in the SFR is at  $\sim 4$  Gyr in **Figure 2.2**, but we note that the gas fraction of the Milky Way as a whole is  $\sim 0.1$  to  $0.15$  (e.g., Boissier and Prantzos, 1999). This lower gas fraction would require a larger  $\omega$  than the one we used, which would push the gas mass peak for the whole galaxy (not the solar annulus) to earlier times (near  $\sim 2$  to  $3$  Gyr). We thus expect that our choice of parameter values is consistent with observations of star formation at high redshift. We use these choices of  $k$ ,  $\Delta$ , and  $\omega$  throughout the remainder of this work.

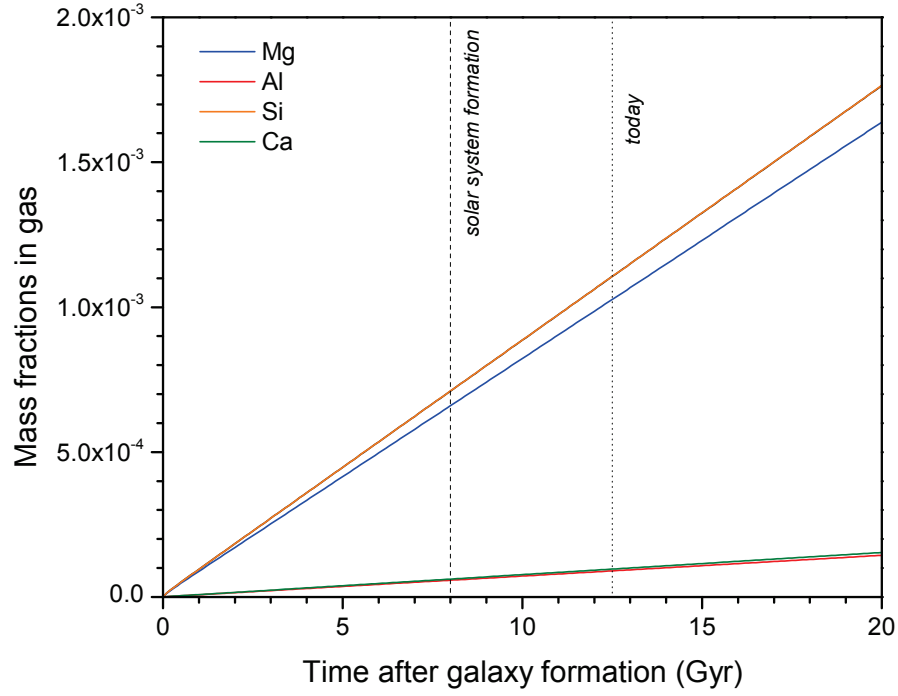
#### 2.4.2. Mass fractions

Output from the Clayton model yields species abundances in terms of mass fractions ( $Z_i$ ). At  $t = 0$  (where  $t$  is time after Galaxy formation), the gas starts as being metal-free before being enriched by the nucleosynthesis products of the first generation of massive stars. Since the species mass fractions in the gas of the solar annulus is known for our solar system from measurements of chondrite meteorites and the solar photosphere, the model is fit to those values at  $t = 8$  Gyr. (Since the age of the solar system is  $\sim 4.5$  Gyr and the age of the Galaxy is  $\sim 12.5$  Gyr, we assume that the solar system formed 8 Gyr into galactic history.) For the case of stable, primary-only species, the gas experiences a constant rate of enrichment, as shown in the example for Mg, Al, Si, and Ca in **Figure 2.3**. This is also the case for all species considered here except for  $^{56}\text{Fe}$  and  $^{40}\text{K}$ .

Iron-56 is a special case due to an additional production source found in Type Ia supernovae, which is the explosive result of a white dwarf (the remnant of a low-mass star that has reached the end of its lifetime and no longer experiences fusion) in a binary system that reaches critical mass from the stripping of material from its companion star, reigniting



**Figure 2.3.** Mass fractions of several of the major mantle-forming elements. In the analytical Clayton model, these are primary species that experience a constant state of enrichment in the gas since the gas is initially metal-free and have concentrations that are fit to CI values at the time the solar system formed.



fusion for a few seconds and burning heavy elements that are immediately ejected (Hillebrandt and Niemeyer, 2000). Because Type Ia supernovae occur at the end of a star's lifetime, their contributions to gas do not begin until the first generation of these low-mass stars has lived and died. This occurs  $\sim 1$  Gyr after Galaxy formation (Matteucci and Greggio, 1986). At that time, there is a graduate increase in the rate of  $^{56}\text{Fe}$  production, as shown in **Figure 2.4**. We model the yield of  $^{56}\text{Fe}$  as the sum of two primary terms,  $\alpha_1$  due to massive stars and  $\alpha_2$  due to Type Ia supernovae. Early in Galactic history we take the yield to be  $\alpha_1$ , but, as the Galaxy ages, the yield evolves to  $\alpha_1 + \alpha_2$ . We chose  $\alpha_1$  and  $\alpha_2$  and the timescale for evolution of the total  $^{56}\text{Fe}$  from  $\alpha_1$  to  $\alpha_1 + \alpha_2$  to reproduce Galactic disk  $[\text{O}/\text{Fe}]$  vs.  $[\text{Fe}/\text{H}]$  trends (Bensby et al., 2004).

Potassium-40 is a different case in that it can be produced as both a primary and secondary species. While its abundance in our solar system at the time of formation is known, the relative proportion of the two contributions is not. Owing to this uncertainty, we model endmember production scenarios in which  $^{40}\text{K}$  is only primary or only secondary (**Figure 2.5**). We then take a best fit to the two that incorporates contributions from both primary and secondary sources but later accounts for the range of plausible resulting concentrations and heat productions on the planetary scale.

### 2.4.3. Scaling to planets

Since our model makes predictions for the composition of the ISM from which solar systems form, the species mass fraction output is for bulk solar system material, which for our solar system is represented by the solar photosphere or CI carbonaceous chondrites minus volatile elements. These figures are not appropriate for direct insertion into geophysical

**Figure 2.4.** Mass fraction evolution of Fe in gas. Initially, it is only produced in massive stars, but  $\sim 1$  Gyr after formation, Type Ia supernovae begin contributing Fe, increasing its production rate.

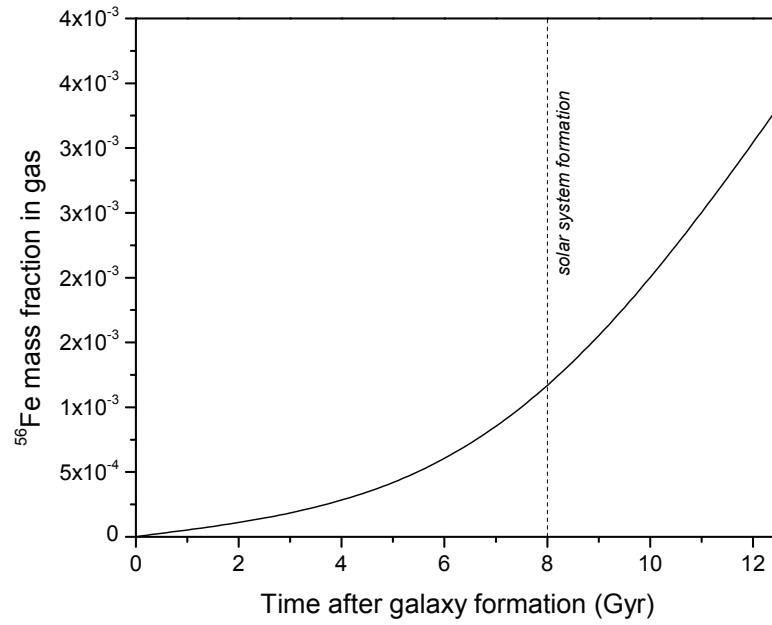
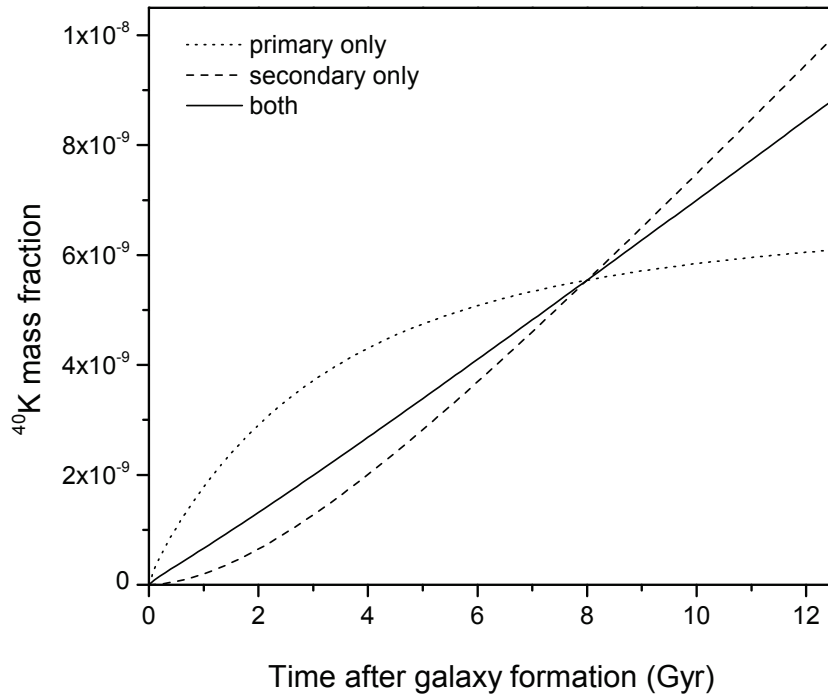


**Figure 2.5.** Mass fraction evolution of  $^{40}\text{K}$  in gas. Unlike  $^{232}\text{Th}$ ,  $^{235}\text{U}$ , and  $^{238}\text{U}$ , it has both primary and secondary species contributions. Although its concentration in the solar system is known for  $t = 8$  Gyr, the relative contributions of each process are not. Endmember scenarios for the  $^{40}\text{K}$  being only primary or secondary are shown, with a best fit that we selected (solid line) located between the two.



models of rocky exoplanets. When planets form and differentiate, elements fractionate according to their affinities for gas, metal, or silicate species (§1.2.2). Differentiation separates metal and siderophile elements from silicate and lithophile elements as metal descends into the burgeoning core, so from an early stage, the bulk silicate Earth (BSE) experienced fractionation of incompatible elements into crustal components (Caro, 2011 and references therein). To account for fractionation, we scale the bulk solar system concentration output to Earth-like values by using the ratio of the relevant isotopes between the concentrations of Earth’s mantle and CI values.

It is clearly a challenge to make the leap from the scale of bulk solar system chemistry to that of an individual planet. Currently, inferring the composition of a particular exoplanet from that of its star requires many assumptions. To sidestep this issue, we only consider here what we term “cosmochemically Earth-like exoplanets” whose bulk solar system/planet ratios for the species of interest match those of the Earth relative to the solar system. We justify this approach in several ways:

1. No formation model can currently explain all observed properties of our solar system.

The modeling is challenging: one must reconcile the chemistry, location, and mass of each planet. This remains an active area of research (e.g., Bond et al., 2010) but is currently impossible to perform for exoplanets due to the paucity of information about their planetary systems. With this in mind, we consider only planets that possess species in abundances identical in proportion to that between Earth and CI chondrites.

2. An “Earth-like” exoplanet is commonly defined as one that is close to Earth’s size and lies within its star’s so-called habitable zone. However, there are many distinct characteristics about Earth that make it what it is, not the least of which is chemistry.

With a single example for life in the Universe, we only have Earth on which to base

our definition of a habitable planet. Assuming an Earth-scaled chemistry for a planet incorporates the assumption that a potentially habitable Earth-like planet is also chemically Earth-like.

3. Applying such a ratio takes into account any stochastic accretion processes that went to building Earth and evolving it to its current state (§1.1.3), such as the Moon-forming Giant Impact (Canup, 2008), Late Veneer (Chou, 1978), planet migration, and Late Heavy Bombardment (Gomes et al., 2005).
4. The chemical compositions of the bulk solar system (from carbonaceous chondrites and observations of the solar photosphere) and Earth’s mantle (from peridotites) are reasonably well constrained and provide hard numbers with which to fit the GCE model.

Quantitatively, we apply this simple formula to the mass fraction output of a particular species to find its abundance in the mantle of a cosmochemically Earth-like exoplanet:

$$\frac{\text{CI chondrite}}{\text{Earth's mantle}} = \frac{\text{modeled bulk solar system}}{\text{predicted exoplanet mantle}} \quad (10)$$

**Table 2.2** shows the canonical chemical abundances used for CI chondrites (Anders and Grevesse, 1989) and Earth’s mantle abundances of major elements (Kargel and Lewis, 1993; McDonough and Sun, 1995) and the relevant radiogenic species (Turcotte and Schubert, 2002).

**Table 2.2.** Chemical abundances (expressed as mass fractions) assumed here for the solar system and the Earth. References include: (1) Anders and Grevesse (1989), (2) McDonough and Sun (1995), (3) Kargel and Lewis (1993), and (4) Turcotte and Schubert (2002).

	CI	Reference	Earth's mantle	Reference	CI/Earth
C	$3.07 \times 10^{-3}$	1	$1.20 \times 10^{-4}$	2	$3.91 \times 10^{-2}$
O	$9.62 \times 10^{-3}$	1	$4.44 \times 10^{-1}$	3	$4.62 \times 10^1$
Na	$3.34 \times 10^{-5}$	1	$2.67 \times 10^{-3}$	2	$8.00 \times 10^1$
Mg	$6.60 \times 10^{-4}$	1	$2.28 \times 10^{-1}$	2	$3.45 \times 10^2$
Al	$5.80 \times 10^{-5}$	1	$2.35 \times 10^{-2}$	2	$4.05 \times 10^2$
Si	$7.11 \times 10^{-5}$	1	$2.10 \times 10^{-1}$	2	$2.95 \times 10^2$
S	$4.18 \times 10^{-4}$	1	$2.50 \times 10^{-4}$	2	$5.98 \times 10^{-1}$
K	$3.74 \times 10^{-6}$	1	$2.40 \times 10^{-4}$	2	$6.42 \times 10^1$
Ca	$6.20 \times 10^{-5}$	1	$2.53 \times 10^{-2}$	2	$4.08 \times 10^2$
Ti	$2.91 \times 10^{-6}$	1	$1.21 \times 10^{-3}$	2	$4.14 \times 10^2$
Cr	$1.78 \times 10^{-5}$	1	$2.63 \times 10^{-3}$	2	$1.48 \times 10^2$
Fe	$1.17 \times 10^{-3}$	1	$6.26 \times 10^{-2}$	2	$5.36 \times 10^1$
Ni	$7.34 \times 10^{-5}$	1	$1.96 \times 10^{-2}$	2	$2.67 \times 10^2$
Sum	0.0160		1.02		
$^{40}\text{K}$	$5.54 \times 10^{-9}$	1	$4.64 \times 10^{-7}$	4	$8.36 \times 10^1$
$^{232}\text{Th}$	$2.46 \times 10^{-10}$	1	$1.55 \times 10^{-7}$	4	$6.29 \times 10^2$
$^{235}\text{U}$	$3.41 \times 10^{-11}$	1	$1.64 \times 10^{-8}$	4	$4.83 \times 10^2$
$^{238}\text{U}$	$1.09 \times 10^{-10}$	1	$6.24 \times 10^{-8}$	4	$5.73 \times 10^{-2}$

#### 2.4.4. Results for solar systems at time of formation

After applying the CI/mantle scaling factor to the mass fraction output, we can make predictions for the concentrations of the species in the rocky mantles of cosmochemically Earth-like planets.

##### 2.4.4.1. Concentrations

**Figure 2.6** shows the calculated concentrations of  $^{40}\text{K}$ ,  $^{232}\text{Th}$ ,  $^{235}\text{U}$ , and  $^{238}\text{U}$  as a function of the time of formation of generic exoplanets after Galaxy formation. Abundances of those isotopes in Earth's mantle when it formed at  $t = 8$  Gyr are shown for reference. The curves show that the later a planet forms in galactic history, the lower its starting concentrations of the isotopes will be. This is because while the isotopes are being continually produced as the Galaxy ages, they are also simultaneously decaying, whereas the stable species ostensibly are not. As a result,  $^{40}\text{K}$ ,  $^{232}\text{Th}$ ,  $^{235}\text{U}$ , and  $^{238}\text{U}$  are essentially being diluted by the buildup of the stable major mantle-forming elements as the Galaxy ages.

##### 2.4.4.2. Heating

While the concentrations of the isotopes are instructive in showing their evolution relative to the stable mantle-forming elements, those concentrations do not directly translate to radiogenic heating. Each isotope has a different specific heat output per unit mass (**Table 2.1**). For example, while  $^{40}\text{K}$  clearly dominates in concentration,  $^{235}\text{U}$  has the highest heat output. **Figure 2.7** shows the relative heat contributions of each isotope to a planet's mantle at the time of formation. Owing to its short half-life but high heat production,  $^{235}\text{U}$  is the most important isotope in heating planets within  $\sim 5$  Gyr after galaxy formation. After that,  $^{40}\text{K}$  takes over. The dilution effect is particularly apparent in terms of heating: planets that formed

**Figure 2.6.** The initial concentrations of  $^{40}\text{K}$ ,  $^{232}\text{Th}$ ,  $^{235}\text{U}$ , and  $^{238}\text{U}$  in cosmochemically Earth-like mantles as a function of the time at which they formed in galactic history. The dots indicate their concentration in Earth's mantle at the time of its formation.

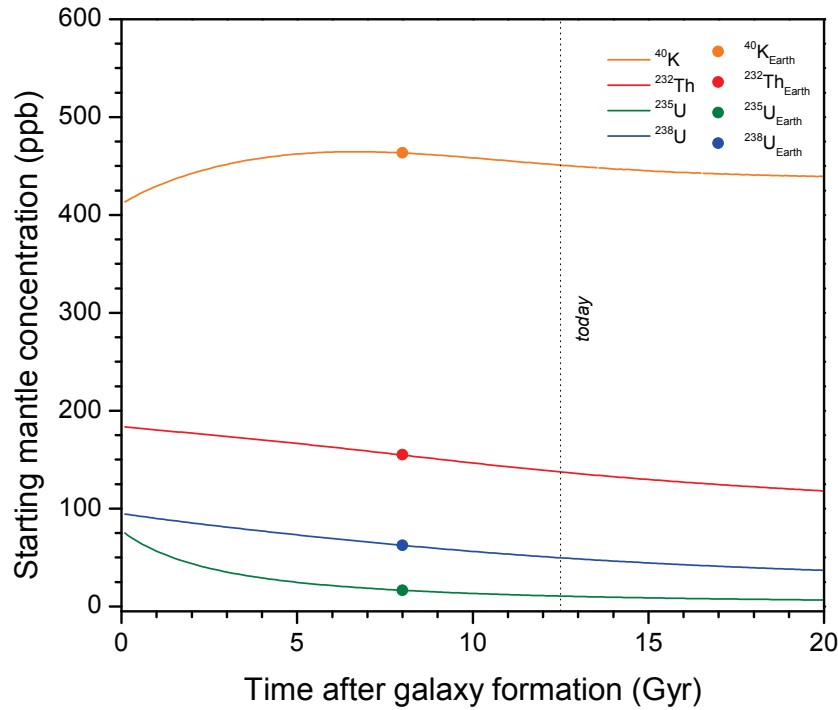
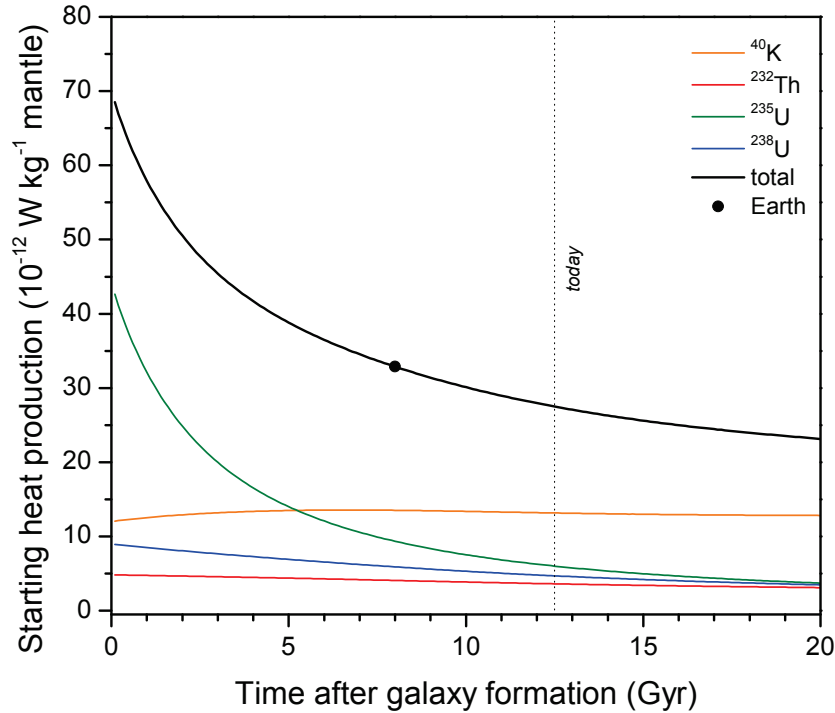


**Figure 2.7.** The initial heat productions of  $^{40}\text{K}$ ,  $^{232}\text{Th}$ ,  $^{235}\text{U}$ ,  $^{238}\text{U}$ , and their total in cosmochemically Earth-like exoplanet mantles as a function of their formation time. The black dot indicates Earth's mantle's starting heat production rate.





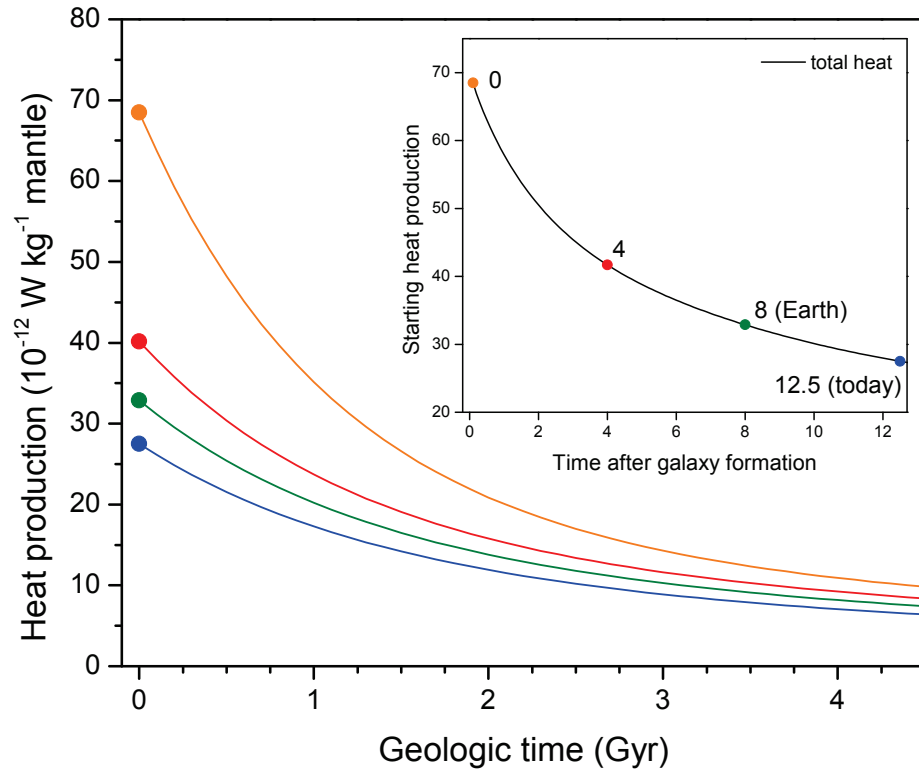
immediately after the Galaxy formed would have had more than twice as much initial heating than the Earth did at the time of its formation. The rate of decline in total initial heat production is slowing such that a planet forming today starts with  $\sim 5 \times 10^{-12} \text{ W kg}^{-1}$  less than Earth when it formed.

Given that radiogenic heating at the time of a planet's formation is one of the parameters that will dictate the planet's tectonic regime and evolution thereof, accounting for the time of a planet's formation and resulting initial heating is crucial. This factor has not been quantitatively accounted for in exoplanet models thus far. To underscore the effect of a planet's time of formation on its thermal evolution, **Figure 2.8** shows the heat production 4.5 Gyr after formation in planets that formed at  $t = 0, 4, 8$ , and 12.5 Gyr into galactic history (where  $t = 8$  Gyr is when Earth formed). Planets that formed soon after galaxy formation will always have more heat at a particular point in their geologic history than those that formed later. As the isotopes decay, their concentrations will converge as they approach zero, and so heat productions are more similar as planets age. However, the initial concentration helps set a planet's tectonic regime, and so starting with an appropriate initial value is important (Noack and Breuer, in press).

#### **2.4.5. Results for solar systems today**

While the initial heating in a planetary mantle is key to setting the conditions for its tectonic evolution, it is also imperative to consider its current heat production, as a planet that is too cool cannot sustain plate tectonics, if it ever did in the first place.

**Figure 2.8.** Heat production for 4.5 Gyr in cosmochemically Earth-like planets that formed 0, 4, 8, and 12.5 Gyr after the Galaxy formed.



#### 2.4.5.1. Concentrations

We now consider the current heat production in planets as a function of their age at the present time. To do this, the concentrations of the isotopes are decayed based on how long they have had to decay, i.e., the age of the planet. Again, the Galaxy is assumed to be 12.5 Gyr old (Dauphas, 2005). **Figure 2.9** shows the predicted concentrations of  $^{40}\text{K}$ ,  $^{232}\text{Th}$ ,  $^{235}\text{U}$ , and  $^{238}\text{U}$  in cosmochemically Earth-like planets as a function of their age. Owing to its half-life of 14 Gyr,  $^{232}\text{Th}$  has declined by only 54% over the age of the Galaxy, while  $^{40}\text{K}$  and  $^{235}\text{U}$  are effectively extinct and  $^{238}\text{U}$  is about 15% of its original concentration. Potassium-40 is abundant relative to the other isotopes, but with a half-life of only 1.25 Gyr, it does not contribute significantly after planets reach ~6 Gyr old.

#### 2.4.5.2. Heating

As expected, young planets are radioactively hotter than old planets. Specifically, as shown in **Figure 2.10**, planets forming today (age = 0 Gyr) are producing ~8× more heat than an ancient planet that formed at the time the Galaxy formed (age = 12.5 Gyr). With its relatively short half-life of 0.704 Gyr,  $^{235}\text{U}$  does not contribute significantly to heat after ~3 Gyr into a planet's history. The gray band in **Figure 2.10** shows the endmember scenarios for  $^{40}\text{K}$  as either only a primary species (minimum) or a secondary species (maximum). The proportions of primary versus secondary contributions turn out to not make a significant difference on the heating outcome. Rather, the age of a planet is a much more important factor. A table of heat production values as a production of age can be found online in **Appendix 2**. We envision that these values can be used in geophysical models of exoplanets.

**Figure 2.9.** Concentrations of  $^{40}\text{K}$ ,  $^{232}\text{Th}$ ,  $^{235}\text{U}$ , and  $^{238}\text{U}$  in exoplanets today as a function of their age. The dots show the current concentration of these isotopes in Earth's mantle.

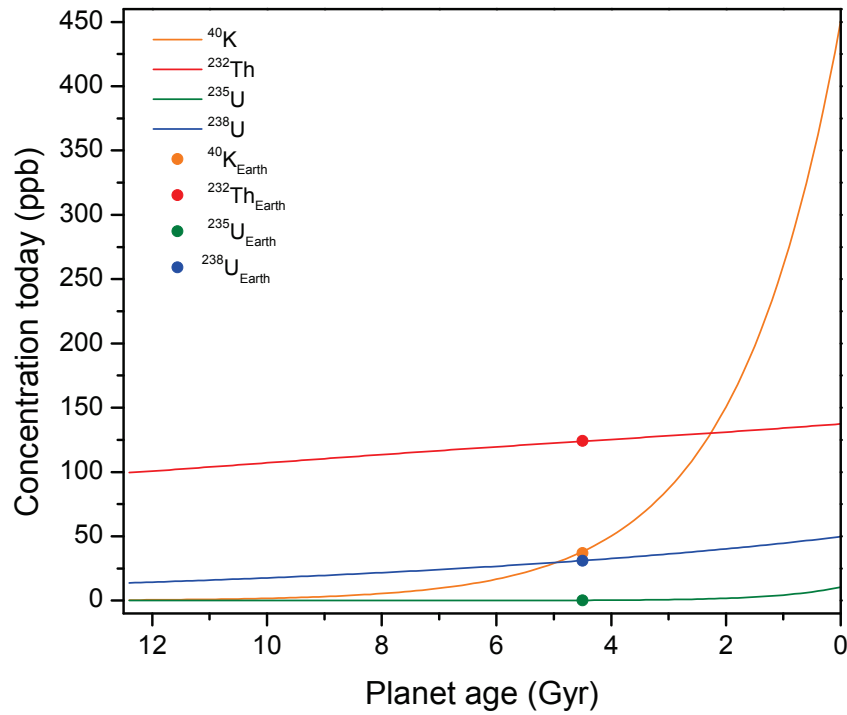
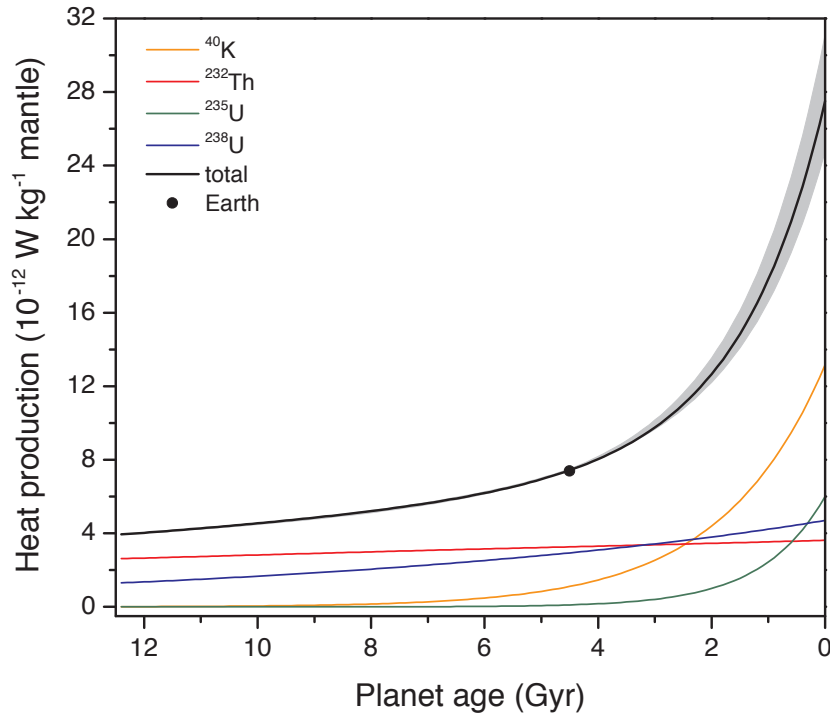


**Figure 2.10.** Current heat production in exoplanets as a function of their age. The gray band shows the range of heat productions if  $^{40}\text{K}$  depending on the relative proportions of primary versus secondary contributions.



## 2.5. Discussion

### 2.5.1. Testing against observations

Similar to the methods of geochronology used for silicate material, long-lived radionuclides can be used to determine the age of stars in nucleocosmochronology. This technique is useful because knowledge of the lifetime of stars is crucial to our understanding of the timescale of stellar processes. Other methods of stellar dating include position in the Hertzsprung-Russell diagram, lithium depletion in clusters via low-mass stars, and asteroseismology (Soderblom, 2010). In contrast to these techniques, nucleocosmochronology is one of the few that is independent of stellar isochrones. However, the technique is hindered by the reliability of heavy element detection due to observational constraints. Presently, robust spectroscopic observations for U and Th are limited to the r-process-enriched, ancient galactic halo stars because they are so metal-poor that there are few absorption line interferences from other elements. With only one weak optical absorption line, Th is still the most easily measured long-lived radioactive element. Europium is usually used as a reference element, but its utility has been called into question due to the large difference in atomic mass between it and Th and because these nuclides do not have perfectly identical nucleosynthetic histories (Ludwig et al., 2010). For this reason as well as for the comparable mean half-lives of U and Th relative to Eu, U is considered to be the best element for dating in combination with Th (Clayton, 1988; Ludwig et al., 2010). It is not yet possible to remotely differentiate among isotopes in these astronomical observations, so their elemental ratio (U/Th) must be used in combination with their isotopic production ratio to calculate the age of a star. This is not an issue since all  $^{235}\text{U}$  has decayed to extinction in these ancient stars such that  $^{238}\text{U}$  is the only uranium isotope that remains.

A way to test our predictions against observations is to take our modeled present-day, age-dependent (U/Th)<sup>a</sup> ratios in solar systems and compare them to spectroscopic observations of stars of different ages. The observed (U/Th) ratio in such stars only accounts for <sup>238</sup>U and <sup>232</sup>Th since we can be confident that <sup>235</sup>U is long extinct. The caveats in using these data, however, are that halo stars are among the oldest in the Galaxy, they are unusually enriched in the r-process elements, and they are located far from the solar annulus; all this being said, they are also the only available data with which to test our model. Future observations with more refined techniques will one day provide firmer constraints.

Due to these inherent observational difficulties in studying such weak spectral features as well as the dearth of viable candidates, U was only first measured in a star in 2001. The star CS31982-001 is both extremely metal-poor and enhanced in the r-process elements, making it an ideal candidate for observations. It was originally reported that based on the observed (U/Th), the star has an age of  $12.5 \pm 3$  Gyr (Cayrel et al., 2001). Later observations by separate groups have proposed ages of  $14.0 \pm 2.4$  Gyr (Hill et al., 2002) and  $15.5 \pm 3.2$  Gyr (Schatz et al., 2002). Today, approximately fifteen ancient, metal-poor halo stars have been documented, several more than once, for their U and Th abundances and/or age. **Table 2.3** includes a full list of published data, much of which was accessed through the SAGA database for extremely metal-poor stars (Suda et al., 2008). The mean margin of error of 20% corresponding to about 2.5 Gyr (Ludwig et al., 2010) is carried over to age predictions and reflects the difficulty of these observations and the compelling need for improvements in

---

<sup>a</sup> The ratio calculations presented here are in the form familiar to geochemists; astronomers instead report  $\log \epsilon(N_A) = \log \left( \frac{N_A}{N_H} \right) + 12$ ,

where  $N_A$  and  $N_H$  indicate the absolute number densities of a nuclide and hydrogen, respectively, and the equation solves for the difference of the log of their ratios of elemental observations between the star in question and the Sun.

**Table 2.3.** U/Th observations and age estimates of ancient, metal-rich halo stars. Bold values indicate papers that published coupled U-Th data with stellar age predictions.

Object	Reference	$\log-\epsilon(\text{U})$	$\log-\epsilon(\text{U})$ error	$\log-\epsilon(\text{Th})$	$\log-\epsilon(\text{Th})$ error	Age (Gyr)	(U/Th)	Age error ( $\pm$ Gyr)
BD+17_3248	1	-2	$0.1\sigma$	-1.18	$0.3\sigma$	<b>13.8</b>	<b>0.151</b>	4
	2					12.6		2.6
	2					15.7		3.4
CS22892-052	3	-2.3	N/A	-1.57	$\pm 0.1$		0.186	
	4	-1.92	N/A	-1.42	$0.15\sigma$		0.316	
	5	-2.4		-1.6		<b>16</b>	<b>0.158</b>	4
	6					15.2		3.7
	1					12.8		3
CS30306-132	4	-1.42	N/A	-1.12	$0.15\sigma$		0.501	
CS31082-001	7	-1.92	N/A	-0.98	$\pm 0.05$	<b>14</b>	<b>0.115</b>	2.4
	4	-1.96	N/A	-0.92	$0.1\sigma$		0.091	
	8	-1.92	$\pm 0.11$	-0.98	$\pm 0.05$		0.115	
	9					<b>12.5</b>	<b>0.1821</b>	3
	2					15		2.6
HD110184	4	-2.52	N/A	-2.5	$0.15\sigma$		0.955	
HD115444	4	-2.35	N/A	-1.97	$0.15\sigma$		0.417	
	10	-2.6		-2.23		<b>14.2</b>	<b>0.427</b>	4
	2					12.4		5.2
HD186478	4	-2	N/A	-1.85	$0.15\sigma$		0.708	
	11					18.3		4.2
	2					18		3.4
HE0338-3945	12	-0.11	$0.38\sigma$	0.23	$0.17\sigma$	<b>12</b>	<b>0.457</b>	
HE1523-0901	13	-2	N/A	-1.2	N/A	<b>13.2</b>	<b>0.158</b>	N/A

<sup>1</sup>Cowan et al. (2002)

<sup>2</sup>Li and Zhao (2009)

<sup>3</sup>Sneden et al. (2003)

<sup>4</sup>Honda et al. (2004)

<sup>5</sup>Sneden et al. (2000)

<sup>6</sup>Sneden et al. (1996)

<sup>7</sup>Hill et al. (2002)

<sup>8</sup>Plez et al. (2004)

<sup>9</sup>Cayrel et al. (2001)

<sup>10</sup>Westin et al. (2000)

<sup>11</sup>Johnson and Bolte (2001)

<sup>12</sup>Jonsell et al. (2006)

<sup>13</sup>Frebel et al. (2007)

technique and technology.

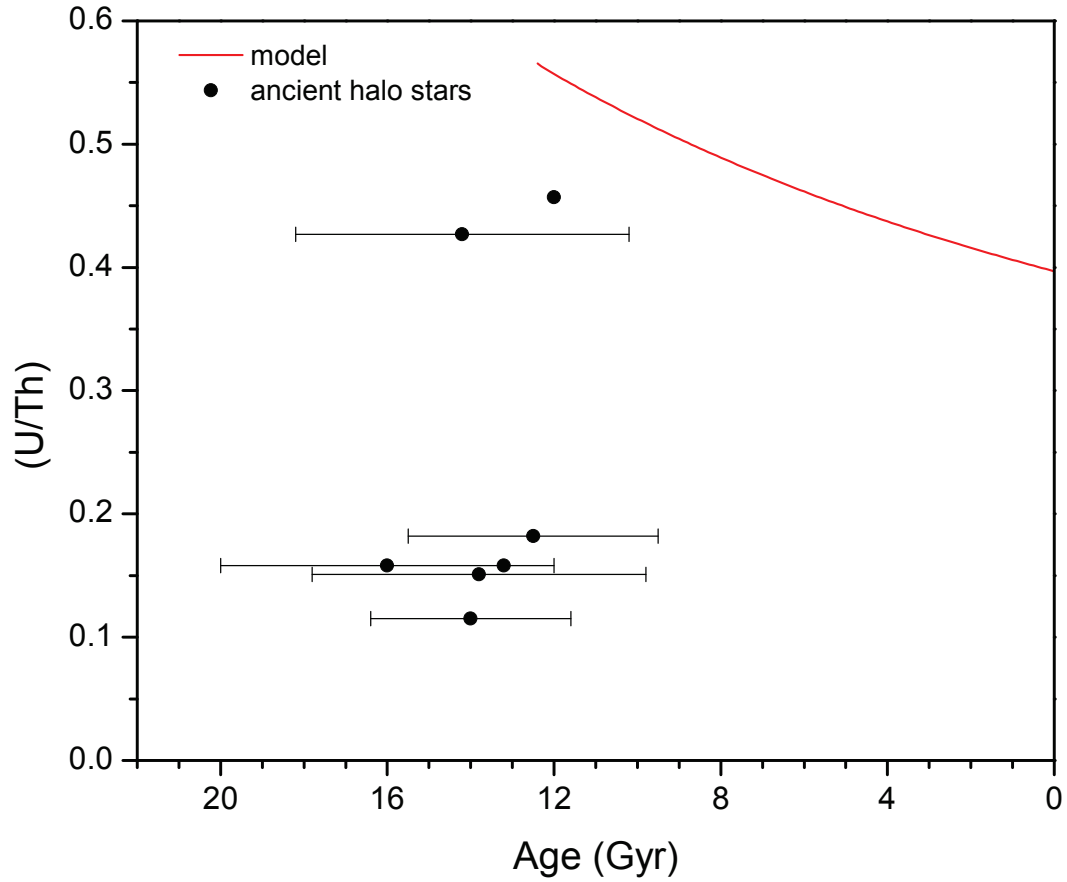
Despite the challenges inherent in nucleocosmochronology estimates, we compare the predictions of our model to observations of the ancient halo stars. The problem with this comparison, of course, is that these stars are unlike those located in the solar annulus. They are particularly metal-poor and actinide-enriched, even for halo stars. Indeed, **Figure 2.11** shows that the observed (U/Th) ratios, with the exception of two stars, are lower than the range predicted from the model though still on the same order of magnitude. The evolving (U/Th) of the model is due to the long half-life of  $^{232}\text{Th}$  relative to those of the U isotopes. Should spectroscopic technology improve in the future such that U and Th can be observed in metal-rich stars, we expect that stars in the solar annulus would have comparable (U/Th) ratios as a function of their age with those predicted by our model.

### 2.5.2. Heat budgets

An individual planet's thermal evolutionary pathway is dictated in large part by its mass (Stevenson, 1982). In particular, planets need to be large enough to retain internal heat over a long period of time for continued geological activity. Both the Earth's Moon ( $0.0123 M_{\oplus}$ ) and Mars ( $0.107 M_{\oplus}$ ) have experienced cooling as their accretionary heat dissipated and radiogenic heating failed to sustain vigorous internal convection. Internal heating also maintains a convecting outer core that sustains a magnetic field, another potentially important consideration for the long-term maintenance of life on exoplanets. The habitable potential of a planet's surface may be severely suppressed without a magnetic field due to the protection from solar radiation it provides (Dehant et al., 2007). Mars has been observed to have magnetic anomalies, which is suggestive of but not unequivocal evidence for



**Figure 2.11.** Modeled (U/Th) ratio compared to the only available stellar U/Th data, which are from ancient metal-poor, actinide-enriched halo stars. The error bars show the wide margin of error on the age estimates. Ratio error bars are not available because U and Th errors are reported separately (**Table 2.3**).

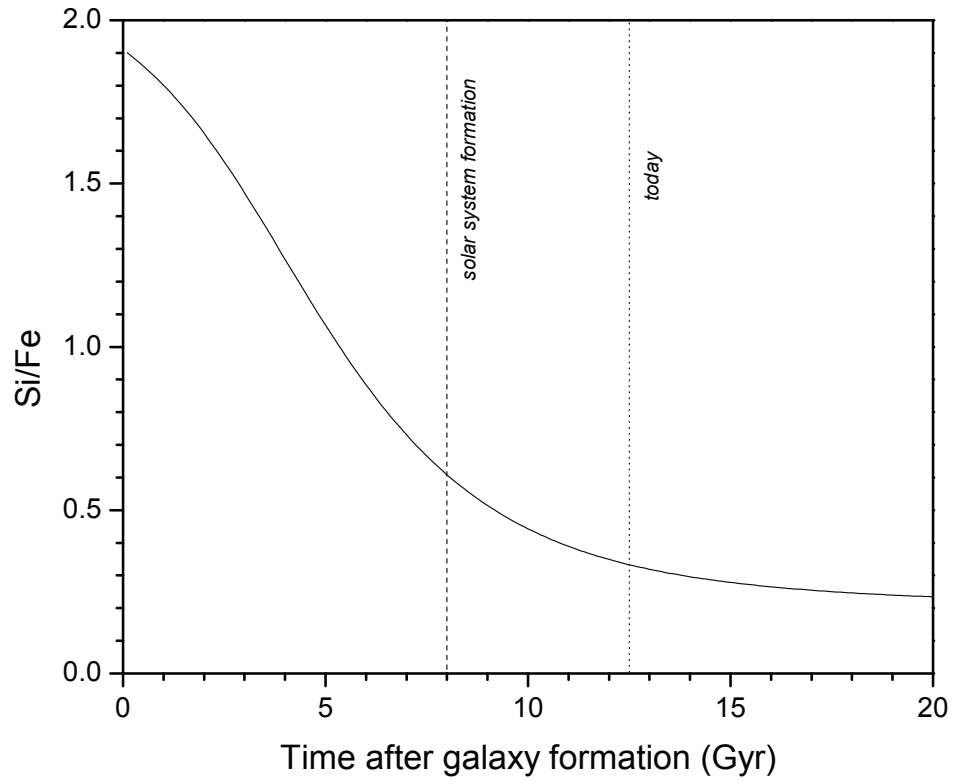


a past magnetic field (Acuña et al., 1998). It may be marginally habitable now in localized environments and almost certainly hosted widespread hospitable environments early in its history (e.g. Nisbet and Sleep, 2001). We consider Mars an adequate lower bound ( $0.1 M_{\oplus}$ ) for the end-member mass of a habitable planet (i.e., a mini-Earth). For an upper bound, Stevenson (1982) showed that after a protoplanet reaches  $\sim 8 M_{\oplus}$ , its predicted bulk composition quickly transitions from that of a silicate-metal planet to an ice giant like Neptune as nebular gases become gravitationally bound to the rocky core; from this it follows that  $8 M_{\oplus}$  can be considered a reasonable upper limit for habitable super-Earths. The mass constraints we adopt here for a thermally Earth-like planet are therefore 0.1 to  $8 M_{\oplus}$ .

A factor tied to nucleosynthesis that will significantly affect a planet’s evolution and subsequent capacity to sustain life is iron availability in the young Galaxy (e.g. Gonzalez et al., 2001). This is confirmed by observations of stellar [Fe/H] values (used as an indicator of metallicity) that are found to generally decrease as a function of increasing stellar age (Chiappini et al., 1997). As nucleosynthesis proceeds, the ISM becomes enriched in Fe as it does with U and Th. Because of the delay in Fe nucleosynthesis from Type Ia supernovae, silicate worlds that formed in the early Galaxy might very well have formed with small metal cores, leading to what we term a “super-lunar” planet. This can be quantified by observing how the Si/Fe ratio changes over time (**Figure 2.12**).

A  $1-M_{\oplus}$  planet with a relatively small lunar-like core ( $R = 1791$  km,  $R_{\text{core}} \sim 330$  km; Weber et al., 2011) will have a correspondingly larger silicate mantle, which means it would have more internal heat than, for example, a  $1-M_{\oplus}$  planet with a core radius proportional to that of Mercury ( $R = 2440$  km,  $R_{\text{core}} = 2030$  km; Smith et al., 2012). Thus, we may postulate

**Figure 2.12.** Si/Fe mass fraction ratio over galactic history. Very early in the Galaxy's history ( $t < 1$  Gyr), the ratio is constant while Si and Fe are both being produced in massive stars, but when Type Ia supernovae begin exploding, the production of Fe increases, resulting in declining Si/Fe.

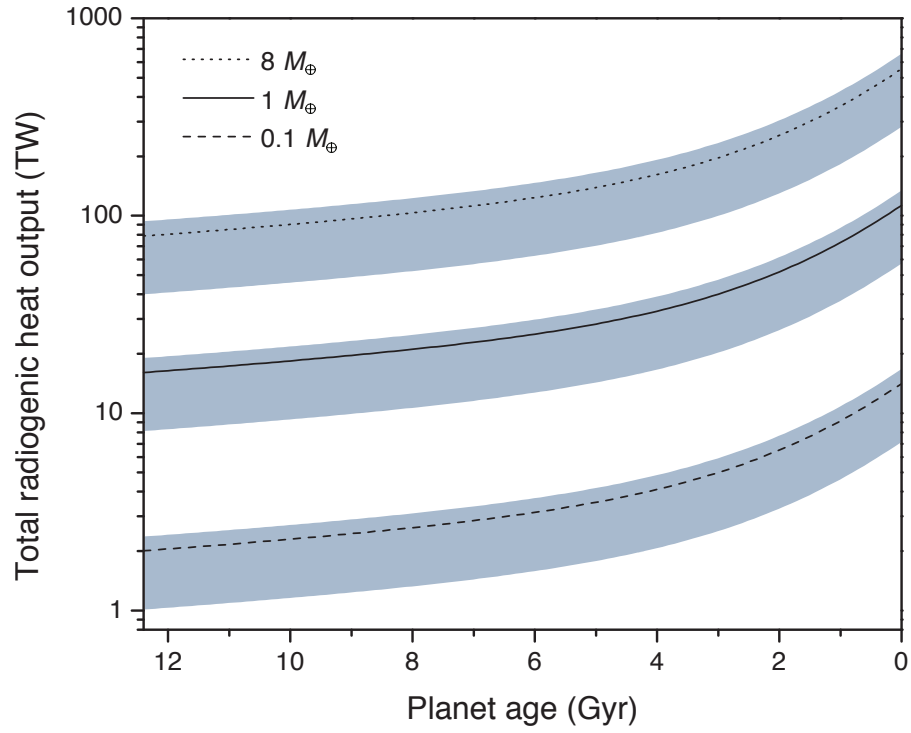


that a planet’s total heat output will be dictated both by its relative core/mantle size and initial radioactive inventory, in addition to its age. **Figure 2.13** shows the total heat output for planets of 0.1-, 1-, or 8- $M_{\oplus}$  and a  $R_{\text{core}}\text{-}R$  ratio like that of the Moon, Earth, or Mercury. The radii corresponding to mass are based on the mass-radius scaling relationship of Seager et al. (2007). A planet of any mass with a core proportional to the Moon’s will produce 20% more heat than one of the same mass with an Earth-scale core, and it will produce twice as much as one with a Mercury-scale core. Earth-mass planets of constant radius will produce 8 times more heat than those that are only 0.1  $M_{\oplus}$ ; planets that are 8  $M_{\oplus}$  will produce about 5 times more heat than an Earth-mass planet. Thus, as a result of the galactic [Fe/H] trend, should ancient solar systems host planets, we can expect their rocky worlds to have bulk compositions more lunar than Earth- or Mercury-like in their relative metal/silicate abundances. Super-lunar planets may have prevailed in the early Galaxy.

## 2.6. Conclusions

In this work, we have integrated a galactic chemical evolution model with cosmochemical data for our solar system and geochemical data for the Earth to make age-dependent predictions for radiogenic heating in what we term “cosmochemically Earth-like” exoplanets. By doing so, we have made predictions for both possible bulk compositions and radiogenic heat production rates for rocky exoplanets in the solar annulus. The results show that although young planets start with lower radiogenic heating rates than old planets due to those species being diluted by stable species, the effect of age—and by extension, the period of time that the isotopes have had to decay—overpowers this characteristic. Indeed, exoplanets forming today will have  $\sim 7\times$  more heating than a planet that is 12.5 Gyr old, the age of the

**Figure 2.13.** Total heat output from radiogenic heating as a function of a planet's mass (8, 1, or 0.1 Earth masses), relative core size, and age. The lines show the heat output for planets of different masses that have Earth's mantle/core ratio. The upper and lower bounds of each band are from planets that have the Moon's mantle/core ratio (upper) and Mars' mantle/core ratio (lower).



Galaxy. Those ancient planets may also have formed with small cores due to the initially high Si/Fe ratio in the young Galaxy before Type Ia supernovae increased the galactic Fe production rate. This will also have an effect on their total radiogenic heat budgets, as planets with small cores—like the Moon—will have more silicate material, and thus higher radiogenic heating, than a planet with a proportionally large core such as Mercury.

While there are many more factors than radiogenic heating that can affect a planet's tectonic regime, radiogenic heating is one that can be constrained. Setting the thermal evolution of an individual planet is important for geophysical models because heat production helps determine both the initial tectonic state of a planet (such as whether plate tectonics is capable of being initiated) and its subsequent evolution. We envision that the heat productions predicted here will be incorporated into geophysical models of exoplanets. This is imperative because a geologically active exoplanet, in the context of the search for Earth-like planets, is more likely to be capable of supporting life on a global scale than a dead planet. Furthermore, since hotter planets are more likely to be geologically active, future searches for exoplanet host stars should be directed towards young stars that might host planets that are Earth-like in terms of their chemistry in addition to their size and orbital parameters.

## Chapter 3: The geochemical record and dynamics of the Late Veneer

While Earth's chemistry can be used to infer that of other planets (§2), it is primarily used to explore the formation and evolution of Earth itself. The behavior of the elements in Earth processes is relatively well understood, so anomalies in their abundances or differences between various rock types often provide the most information—and the most interesting studies. Here, an unexpected signature in ancient rocks from the deep mantle is used to decipher the story of a poorly understood impact that the burgeoning Earth experienced, and dynamical simulations are used to back out the specifics of this event.

### 3.1. Geochemistry

#### 3.1.1. Introduction

During primary accretion, as metallic cores grew within the population of large differentiated planetary embryos, highly siderophile elements (HSE) should have been

effectively stripped from silicate mantles via strong partitioning into metal phases and segregated into metallic cores (Stevenson, 1981). The HSE include the platinum-group elements (PGE: Os, Ir, Ru, Rh, Pt, Pd), Au, and Re. Recent estimates of the Os, Pt, and Re concentrations in Earth's core suggest that these elements are three to four times more enriched relative to the Allende CV3 chondrite values, and  $\sim 10^3\times$  more than the primitive mantle (Day, 2013). It has long been known, however, that the HSE are present in modern terrestrial mafic and ultramafic rocks (basalts and komatiites) at concentrations several orders of magnitude higher than those predicted based on simple partitioning behavior (Kimura et al., 1974).

Komatiites are volcanic rocks of peridotitic composition with >18 wt.% MgO that can be used as archives of Archean mantle chemical evolution (e.g., Arndt et al., 2008). They are strongly enriched in the HSE in comparison to many kinds of mafic crustal rocks, and much more so than any normal felsic suite. It is surprising that any mantle-derived rocks contain so much as ppb-level abundances of the HSE given that, as described above, core formation should have stripped these elements from the silicate Earth. Even more surprising is the observation that the HSE are present in chondritic relative abundances in Earth's mantle despite displaying different metal-silicate partitioning behaviors between the elements. One explanation for this phenomenon is that a late accretion event (dubbed the "Late Veneer" for the case of Earth) supplemented the mantle with primitive solar system material (Chou, 1978). Late accretion was "late" in the sense that it would have occurred after core formation and, consequently, the chemical separation of the core from the mantle. Assuming that the delivered material polluting the mantle after core closure was of chondritic composition, as much as ~1% of Earth's mantle mass (~0.5% of its total mass) would be required to cause the

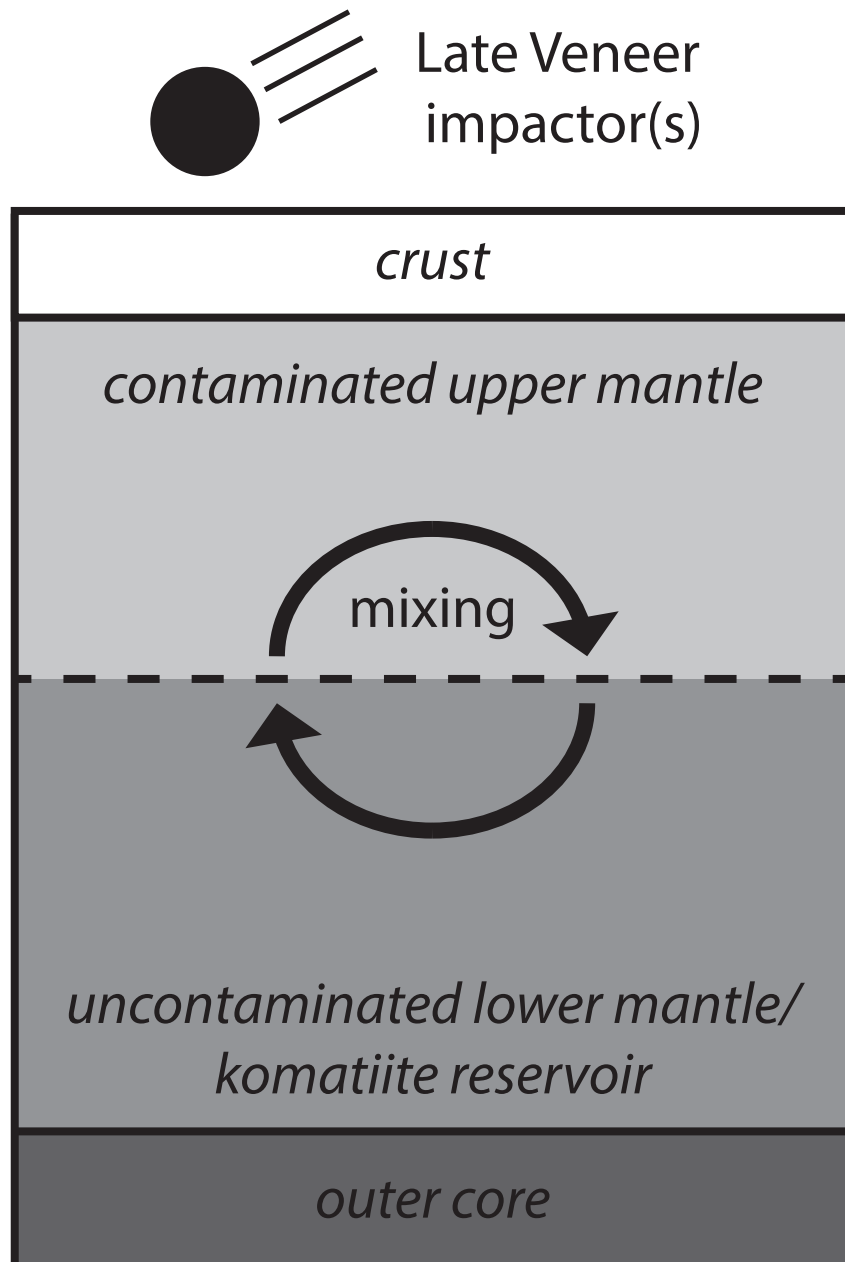


observed signature (Chou, 1978; Walker, 2009). A single chondritic impactor of that size corresponds to a differentiated body approximately 2700 km in diameter. The presence of objects this large at the time of the Late Veneer can be explained by a leftover population from planetary accretion (Bottke et al., 2010), but a multiple impactor scenario cannot be ruled out (Rubie et al., 2011).

Analyses of Pt and Ru in extrusive ultramafic rocks (komatiite *s.l.*) as old as about 3.5 Ga reveal a secular HSE trend in the mid- to deep-mantle reservoirs from which such rocks are sourced (Maier et al., 2009). The Late Veneer scenario was favored by Maier et al. (2009) to explain the depleted HSE abundance trends in the komatiite record, though this mechanism is only viable if the delivered material penetrated no farther than the upper mantle far away from the (deep) komatiite source. Arndt (2009) coined the term “trickle-down geodynamics” to describe an early scenario in which the deep mantle was relatively depleted in HSE until the upper mantle regions, polluted by HSE-rich components, were mixed throughout (**Figure 3.1**). The secular rise in mantle source Pt and Ru concentration occurred between about 3 and 3.5 Ga as reported in Maier et al. (2009).

Rocks of komatiitic affinity have been inferred from various ultramafic schists documented in ancient gneiss complexes that are at least 3.7 Gyr old (e.g., Anbar et al., 2001; Nutman et al., 1996), but almost no published komatiite data extend to samples older than about 3.5 Ga that could be used to explore the trend in HSE reported by Maier et al. (2009). Here we present HSE analyses of ten Eoarchean ultramafic schists, interpreted to represent komatiite protoliths that were collected in supracrustal enclaves of the ca. 3.83 Ga Akilia association (Itsaq Gneiss Complex) in southern West Greenland (Cates and Mojzsis, 2006; Manning et al., 2006), and the ca. 3.78 Ga Nuvvuagittuq supracrustal belt (Inukjuak domain)

**Figure 3.1:** Schematic of the late accretion scenario proposed by Maier et al. (2009), dubbed “trickle-down geodynamics” by Arndt (2009).



in northern Québec (Cates and Mojzsis, 2007; Cates et al., 2013). Our komatiite data are supplemented with a further eight analyses of amphibolites (meta-basalts) from the same localities. Some of these other samples are interpreted to represent fractionated derivatives of the komatiites. Results show that not only do Eoarchean rocks of komatiite protolith exist, but that the secular evolution of HSE abundance trends follows the pattern observed by Maier et al. (2009) to very low values for even older rocks. We use these data to further explore the hypothesis that observed HSE trends arise from an in-mixing of a postulated Late Veneer component to Earth's mantle. We find that the time required for this dynamic chemical homogenization is consistent with proposed early (slow) mantle stirring rates (O'Neill et al., 2013), long crustal recycling times ( $\sim 750$  Myr) as derived from coupled  $^{146,147}\text{Sm}/^{143,142}\text{Nd}$  systematics (e.g., Roth et al., 2013), and low  $^{182}\text{W}/^{184}\text{W}$  from a postulated Late Veneer contaminant (e.g., Willbold et al., 2011).

### 3.1.2. Late Veneer vs. Late Heavy Bombardment

The Late Veneer, if it were an event at the tail end of planetary accretion, must have occurred after the final physical-chemical closure of the core to the mantle. This event would have been subsequent to the postulated Moon-forming impact some 30 to 100 Myr into solar system history (Rudge et al., 2010; Jacobsen et al., 2014). A Giant Impact to the proto-Earth is thought to have generated a debris disk that re-accreted to form the Moon (e.g., Canup and Asphaug, 2001; Ćuk and Stewart, 2012). It is worth noting that any accretion events that enriched Earth's mantle with HSE *preceding* lunar formation are expected to have had that signature erased owing to disruption and re-formation of the core (Stewart and Leinhardt, 2012). As such, we argue that the time frame of about 4.53 Ga (at the earliest) to approximately 4.46 Ga (at the latest) can be used as likely uppermost temporal bounds for the

LV. The lower bound is provided by the oldest evidence of preserved crust from zircons dated to be ca. 4.37 Ga from the Narryer Gneiss Complex in Western Australia (Harrison, 2009; Valley et al., 2014). There is no obvious reason that the timing of the Late Veneer to Earth was substantially different from the other terrestrial planets (e.g., Mars).

On the other hand, a late lunar cataclysm (Tera et al., 1974), or as it is more commonly called, the “Late Heavy Bombardment” (hereafter, LHB), arrived later (ca. 4.2-3.9 Ga) and was far less violent than the postulated Late Veneer (e.g., Morbidelli et al., 2012; Norman and Nemchin, 2014). Even if the LHB potentially melted  $\leq 10$  vol.% of Earth’s crust (Abramov et al., 2013), it is calculated to have had a delivered mass ( $1.8 \times 10^{20}$  kg; Gomes et al., 2005) about 2250 times less than the LV. With this in mind, simple linear extrapolation shows that a tenfold increase in impactor mass from the LHB would have been enough to destroy the entire volume of Earth’s crust (Abramov and Mojzsis, 2009). Late Veneer-scale events hundreds of times greater than this would therefore be enough to melt the crust and cause a shallow magma ocean to form (e.g., Elkins-Tanton, 2008). Notably, an upper temporal limit for when Mars might have experienced its last late accretion event—either as a singular or protracted event—was recently established from a ca. 4.43 Ga zircon documented from martian meteorite NWA 7355 (Humayun et al., 2013).

We emphasize that while it is evident that the delivery of the LHB was enough to cause crustal melting and wholesale destruction, it was trivial with respect to effects on the bulk chemistry of the silicate Earth. This is true in terms of HSE abundances, as well as other geochemical characteristics such as O and Os isotopes (see Jacobsen et al., 2014). Conjoining the Late Veneer and the Late Heavy Bombardment as related events misconstrues interpretations of the HSE data in the context of late accretion.

### 3.1.3. Samples and analytical techniques

#### 3.1.3.1 Komatiites as an HSE archive

Sourced from mid- to deep-mantle reservoirs, komatiites are generally regarded to have formed at high degrees of partial melting (20-50%; Arndt, 2003) as a product of the elevated temperatures of the young mantle (e.g., Herzberg et al., 2010; Richter, 1988). This is supported by the general restriction of these rocks to Archean and early Proterozoic terranes. Notable exceptions to this are the Permian-Triassic komatiites in Song Da (Hanski et al., 2004), and the Mesozoic (ca. 88 Myr old) Gorgona Island ultramafic flows (Aitken and Echeverría, 1984).

Most komatiites fall into two main categories delineated by their bulk chemistry: (i) the Al-undepleted “Munro-type” and (ii) the Al-depleted “Barberton-type.” It has been proposed that the former type formed during 30 to 50% fractional melting of a depleted source at approximately 100 to 150 km depth, whereas the latter was derived from 20 to 30% partial melting at depths >200 km (Robin-Popieul et al., 2012), with residual garnet sequestering Al (Arndt, 2003). These different formation scenarios mean that Barberton-type komatiites are characteristically depleted in the heavy rare-earth elements (HREE) from melting in the presence of garnet, whereas Munro-types are depleted in the incompatible trace elements such as the light rare-earth elements (LREE). Less common than the Barberton- and Munro-types are the Ti-rich and Fe-Ti-rich Karasjok-type komatiites, as well as the aforementioned Gorgona komatiites, which have comparatively high  $\text{Al}_2\text{O}_3/\text{TiO}_2$  ratios.

Key to understanding the behavior of the HSE in komatiites is constraining their partitioning behavior between phases. Metal-silicate partition coefficients ( $D^{\text{met/sil}}$ ) of the HSE are mainly constrained through experiments performed at ~1 bar, with all having  $D^{\text{met/sil}}$  values

greater than  $10^5$  (Day, 2013 and references therein). While all the HSE partition very strongly from silicate into metal, it has been shown that they do not have identical  $D$  values. Specifically, the elements of one subgroup, the iridium-series PGE (IPGE: Ir, Ru, Os), behave highly compatibly relative to the platinum-series subgroup (PPGE: Pt, Pd, Rh), which, along with Re and Au, are moderately compatible to moderately incompatible (Barnes et al., 1985). The elements in these subgroups should have each behaved differently in the melts that formed at the time of core formation and separation of the silicate reservoirs. Thus, they are expected to show different degrees of fractionation relative to chondrites. That the HSE unexpectedly appear in ultramafic rocks in chondritic relative proportions (Chou, 1978) is the principle line of evidence for a late accretion explanation.

### **3.1.3.2. Eoarchean rocks of komatiite protolith**

The samples studied here derive from the Nuvvuagittuq supracrustal belt in northern Québec (Canada) and the Akilia association (McGregor and Mason, 1977), including the Akilia (island) and Innersuartuut localities in southern West Greenland. The Akilia association comprises interwoven m- to km-scale enclaves of mafic, ultramafic, and Fe-rich paragneisses of sedimentary derivation (Cates and Mojzsis, 2006). The Nuvvuagittuq supracrustals are composed mainly of amphibolite enclaves surrounded and in some cases intruded, by granitoid gneisses. Full descriptions of whole-rock analyses for the samples reported here and details of their geological settings can be found in Cates and Mojzsis (2006, 2007), Cates et al. (2013), Dauphas et al. (2007), and Manning et al. (2006). Whole rock geochemistry for our ultramafic samples from Akilia (*GR9705*, *GR97M22*, *GR0019*, *GR0020*, *GR0050*, *GR0051*), Innersuartuut (*GR04064*, *GR04065*) and Nuvvuagittuq (*IN05047*, *IN08016*) are reported in **Table 3.1**.

**Table 3.1.** Whole rock data for the ultramafic samples. Major elements are expressed as wt% and trace elements are expressed as ppm. Data come from (1) this study, (2) Manning et al. (2006), (3) McGregor and Mason (1977), (4) Cates and Mojzsis (2006), (5) Cates and Mojzsis (2007), (6) Dauphas et al. (2007), and (7) Cates et al. (2013).

Sample	GR9703	GR0019	GR0020	GR0030	GR0031
Locality	Akilia Island	Akilia Island	Akilia Island	Akilia Island	Akilia Island
Age (Ma)	3825	3825	3825	3825	3825
Reference	1	2	2	2	2
SiO <sub>2</sub>	48.67	46.73	46.52	45.84	47.17
TiO <sub>2</sub>	0.3	0.38	0.28	0.46	0.34
Al <sub>2</sub> O <sub>3</sub>	8.19	8.58	8.5	10.25	7.77
MgO	22.29	21.03	25.3	13.8	23.28
Fe <sub>2</sub> O <sub>3</sub>	10.87	12.43	10.90	12.86	11.64
MnO	0.18	0.18	0.16	0.18	0.16
CaO	4.18	6.39	4.79	12.44	5.2
Na <sub>2</sub> O	0.98	1.13	0.82	1.19	0.84
K <sub>2</sub> O	1.97	0.15	0.08	0.43	0.1
P <sub>2</sub> O <sub>5</sub>	0.02	0.02	0.02	0.3	0.02
LOI	1.95	2.44	2.35	1.45	3.17
Total	99.59	98.23	98.64	97.66	98.49
Rb		3	2	16	0
Sr		13	19	33	11
Ba		5	4	12	4
Sc		35	38	40	31
Nb					
Ta					
Y		9	7	12	8
Zr	26	26	23	33	22
Ni	729	725	971	323	1150
Cr	2367	3180	2300	1570	2720
V					
Co	79	73	83	68	87
Cu					
Zn					
La		2.80	1.30	2.50	1.80
Ce		5.20	2.60	5.00	3.80
Pr		0.65	0.35	0.70	0.48
Nd		3.60	2.20	4.30	3.00
Sm		1.10	0.70	1.30	0.90
Eu		0.52	0.25	0.42	0.34
Gd		1.40	1.00	1.60	1.20
Tb		0.30	0.20	0.30	0.20
Dy		1.80	1.30	2.20	1.50

**Table 1.1.** continued.

Sample	GR9703	GR0019	GR0020	GR0030	GR0031
Locality	Akilia Island	Akilia Island	Akilia Island	Akilia Island	Akilia Island
Age (Ma)	3825	3825	3825	3825	3825
Reference	1	2	2	2	2
Ho		0.40	0.30	0.50	0.30
Er		1.20	1.00	1.40	1.00
Tm		0.18	0.15	0.22	0.15
Yb		1.20	1.00	1.50	1.00
Lu		0.18	0.17	0.22	0.16
Hf		0.9	0.6	1.1	0.8
Th		0.3	0.1	0.2	0.2
U		0.2		0.2	0.3
Pb	5				



**Table 1.1.** continued.

Sample	GR97M22	GR04064	GR04065	IN05047	IN08016
Locality	Innersuartuut	Innersuartuut	Innersuartuut	Nuvvuagittuq	Nuvvuagittuq
Age (Ma)	3750	3750	3750	3740	3750
Reference	3	4	4	5,6	7
SiO <sub>2</sub>	45.00	39.99	50.42	42.40	49.06
TiO <sub>2</sub>	0.32	0.13	0.20	0.894	0.374
Al <sub>2</sub> O <sub>3</sub>	3.08	4.57	5.28	6.40	5.19
MgO	26.82	35.69	18.43	22.56	17.17
Fe <sub>2</sub> O <sub>3</sub>	12.26	11.66	9.52	20.04	14.64
MnO	0.25	0.18	0.20	0.22	0.26
CaO	9.31	2.12	12.79	1.03	10.58
Na <sub>2</sub> O	0.31	0.17	1.10	0.07	0.43
K <sub>2</sub> O	0.22	0.91	0.26	0.03	0.07
P <sub>2</sub> O <sub>5</sub>	0.04	0.01	0.03	0.08	0.11
LOI		4.08	1.62	5.47	2.77
Total	97.61	99.52	99.85	99.2	100.7
Rb		106	12.5	0.44	0.332
Sr		3.82	23.9	1.21	1.815
Ba		10.1	15.7	1.3	< D.L.
Sc		16.3	15.2		
Nb		0.29	1.65	2.82	1.107
Ta		0.54	0.56	0.2	0.33
Y		2.69	7.22	9.57	21.87
Zr		2.61	8.77	34.4	24.46
Ni	1580	1884	640	977.4	855.8
Cr	5540	2451	1504	3098	1680
V		58.3	104	196	113.1
Co					181.7
Cu		4.80	69.3	147	350
Zn		92.0	121	121	54
La		0.42	2.05	2.17	2.248
Ce		1.08	6.93	6.23	5.409
Pr		0.15	1.19	1.04	0.839
Nd		0.59	6.41	5.59	4.455
Sm		0.21	1.83	1.63	1.75
Eu		0.10	0.36	0.26	0.57
Gd		0.35	1.82	1.88	2.821
Tb		0.07	0.26	0.31	0.533
Dy		0.41	1.37	1.98	3.562
Ho		0.11	0.28	0.39	0.751
Er		0.31	0.76	1.13	2.088
Tm		0.05	0.12	0.159	0.312

**Table 1.1.** continued.

Sample	GR97M22	GR04064	GR04065	IN05047	IN08016
Locality	Innersuartuut	Innersuartuut	Innersuartuut	Nuvvuagittuq	Nuvvuagittuq
Age (Ma)	3750	3750	3750	3740	3750
Reference	3	4	4	5,6	7
Yb		0.30	0.79	1.03	2.017
Lu		0.05	0.12	0.159	0.3
Hf		0.11	0.30	1.0	0.69
Th		0.04	0.09	0.2	0.17
U		0.04	0.10	0.0	0.07
Pb		1.16	2.30	0.1	3.92

#### 3.1.3.2.1. Akilia association: GR9703, GR97M22, GR0019, GR0020, GR0050, GR0051

Sample *GR9703* is a hornblendite from the main body of supracrustal rocks from the type-locality of the Akilia association, and it closely corresponds to *GR0019* in Manning et al. (2006). Sample *GR97M22* was not analyzed for its major, minor, and trace element content but this sample is equivalent to *131477* reported in McGregor and Mason (1977; V. McGregor, *personal communication to S. Mojzsis, July 1997*). Sample *131477* showed high Cr (5540 ppm) and Ni (1580 ppm), and its overall composition was interpreted to be similar to that of komatiites from the Onverwacht Group (Viljoen and Viljoen, 1969) and, except for Al<sub>2</sub>O<sub>3</sub> and CaO, the average komatiite from Munro Township (Arndt et al., 1977). Although we report HSE measurements of *GR97M22*, we do not include them in our HSE trend analyses (see Section 4.2).

Samples *GR0019*, *GR0020*, *GR0050*, and *GR0051* all come from the same ultramafic locality at Akilia reported in Manning et al. (2006). They derive from ultramafic units that appear as irregular blocks to oblate lenses <1 m to several m in size within a larger mafic unit locked in a strongly deformed metamorphosed volcano-sedimentary (supracrustal) succession. All samples from this suite are rich in Fe-Mg amphibole and hornblende and are massive to weakly foliated. Sample *GR0050* was identified as ultramafic based on color discrimination in the field by Manning et al. (2006), and although its MgO content (13.8 wt%) is below the 18 wt% MgO typically used to classify komatiites, we include it in **Table 3.1**.

#### 3.1.3.2.2. Innersuurtuut: GR04064, GR04065

High-magnesium samples *GR04064* and *GR04065* have compositions intermediate between abyssal periodotite and basaltic komatiite, although their parentages are different (Cates and Mojzsis, 2006). The samples were collected from a supracrustal enclave that

preserves a mappable succession of metamorphosed volcanic and sedimentary rocks, including banded iron-formations.

#### *3.1.3.2.3. Nuvvuagittuq: IN05047, IN08016*

Both ultramafic samples from this collection show low  $\text{Al}_2\text{O}_3/\text{TiO}_2$  ratios. Sample *IN05047* is associated with nearby banded iron-formations and may preserve pillow structures. Cates and Mojzsis (2007) interpreted this rock to be derived from a melt originating from a source with garnet as a residual phase, consistent with Barberton-type komatiites (see also Dauphas et al., 2007). With 17.17 wt% MgO, *IN08016* is close to the arbitrary (Arndt, 2008) 18 wt% MgO cutoff for a komatiite. It contains 855.8 ppm Ni and 1680 ppm Cr (Cates et al., 2013), both of which are highly elevated concentrations relative to typical values for basaltic melts.

#### *3.1.3.2.4. Mafic samples from Nuvvuagittuq*

All of the mafic samples of relatively lower MgO contents in our sample collection (**Table 3.2**) were collected from Nuvvuagittuq localities. They include three hornblende amphibolites (*IN05013*, *IN05019*, *IN05021*), four cummingtonite-rich (Ca-poor) amphibolites (*IN08012*, *IN08017*, *IN08043*, *IN08044*), and one plagioclase-rich amphibolite (*IN05046*). Sample *IN05013* is a plagioclase-rich hornblende amphibolite captured within a succession of banded iron-formations at the Porpoise Cove outcrops (O'Neil et al., 2007). Samples *IN05019* and *IN05021* are massive hornblende amphibolites with low  $\text{Al}_2\text{O}_3/\text{TiO}_2$  ratios (Cates and Mojzsis, 2007; Dauphas et al., 2007). The  $\text{Al}_2\text{O}_3/\text{TiO}_2$  ratios of samples from Nuvvuagittuq were used by O'Neil and co-workers (2011, 2007) to develop a classification system bearing some resemblance with the komatiite classification system. Thus, medium and high  $\text{Al}_2\text{O}_3/\text{TiO}_2$  ratio cummingtonite-amphibolites are proposed to have crystallized from melts that formed in the

**Table 3.2.** Whole rock geochemistry for the mafic samples from the Nuvvuagittuq Supracrustal Belt. Data come from (1) Cates and Mojzsis (2007), (2) Dauphas et al., (2007), and (3) Cates and Mojzsis (2013).

Sample	IN05013	IN05019	IN05021	IN05046	IN08012
Locality	Nuvvuagittuq	Nuvvuagittuq	Nuvvuagittuq	Nuvvuagittuq	Nuvvuagittuq
Age (Ma)	3750	3750	3750	3750	3750
Reference	1,2	1,2	1,2	1	3
SiO <sub>2</sub>	48.88	46.27	48.87	46.27	42.78
TiO <sub>2</sub>	0.700	0.830	0.710	0.670	0.983
Al <sub>2</sub> O <sub>3</sub>	15.21	15.93	15.34	16.38	14.52
MgO	9.74	9.20	8.64	9.11	12.33
Fe <sub>2</sub> O <sub>3</sub>	12.94	13.02	12.05	11.77	19.78
MnO	0.18	0.19	0.20	0.19	0.19
CaO	6.28	9.26	9.76	10.89	1.41
Na <sub>2</sub> O	0.82	1.30	1.96	1.28	0.06
K <sub>2</sub> O	2.25	1.95	0.99	1.21	3.20
P <sub>2</sub> O <sub>5</sub>	0.07	0.08	0.07	0.07	0.08
LOI	2.74	1.64	1.46	1.94	5.34
Total	99.8	99.7	100.1	99.8	100.7
Rb	69.6	68.3	31.2	43	130.1
Sr	62.5	63.0	73.4	108	4.513
Ba	341	293	85	139	196.2
Sc	40.0	44.04	39.05	47.3	
Nb	1.85	2.18	2.02	1.65	4.0
Ta	0.29	0.61	1.17	0.80	0.30
Y	15.70	16.90	16.55	17.9	16.31
Zr	39.5	43.6	39.9	40	81
Ni	169	143	146	180	114.8
Cr	293	398	350	512	163.3
V	232	259	243	273	308.7
Co					53.52
Cu	10	79	76	67	19
Zn	72	68	68	64	149
La	2.22	3.86	3.16	2.37	4.218
Ce	5.95	8.66	8.37	6.00	8.404
Pr	0.94	1.23	1.30	0.94	1.048
Nd	4.99	6.12	6.73	4.98	4.599
Sm	1.65	1.86	2.00	1.62	1.252
Eu	0.69	0.86	0.78	0.66	0.398
Gd	2.30	2.51	2.63	2.20	1.694
Tb	0.42	0.46	0.46	0.41	0.32

**Table 3.2.** continued.

Sample	IN05013	IN05019	IN05021	IN05046	IN08012
Locality	Nuvvuagittuq	Nuvvuagittuq	Nuvvuagittuq	Nuvvuagittuq	Nuvvuagittuq
Age (Ma)	3750	3750	3750	3750	3750
Reference	1,2	1,2	1,2	1	3
Dy	2.90	3.17	3.09	2.65	2.397
Ho	0.60	0.67	0.65	0.58	0.594
Er	1.81	1.98	1.91	1.77	1.934
Tm	0.270	0.297	0.286	0.26	0.324
Yb	1.81	1.95	1.90	1.75	2.335
Lu	0.283	0.305	0.295	0.28	0.389
Hf	1.16	1.31	1.19	1.09	2.18
Th	0.30	0.30	0.25	0.16	1.025
U	0.09	0.28	0.26	0.07	0.27
Pb	0.9	2.2	3.8	1.9	1.44

**Table 3.2.** continued.

Sample	IN08017	IN08043	IN08044
Locality	Nuvvuagittuq	Nuvvuagittuq	Nuvvuagittuq
Age (Ma)	3750	3750	3750
Reference	3	3	3
SiO <sub>2</sub>	46.56	49.21	44.94
TiO <sub>2</sub>	0.567	0.827	0.882
Al <sub>2</sub> O <sub>3</sub>	15.88	16.05	15.11
MgO	12.50	9.57	12.82
Fe <sub>2</sub> O <sub>3</sub>	13.38	13.31	13.49
MnO	0.27	0.17	0.20
CaO	2.18	3.31	3.59
Na <sub>2</sub> O	0.69	1.20	1.50
K <sub>2</sub> O	2.43	2.16	1.04
P <sub>2</sub> O <sub>5</sub>	0.09	0.10	0.11
LOI	6.23	4.61	5.06
Total	100.8	100.5	98.7
Rb	82.17	73.55	40.76
Sr	58.04	75.67	72.15
Ba	440.3	333.3	223.2
Sc			
Nb	1.629	1.7	2.1
Ta	0.23	0.10	0.16
Y	11.45	15.44	14.81
Zr	61.77	49	49
Ni	180	135.7	149
Cr	613.5	345.3	284.1
V	144.7	218.4	250.7
Co	47.75	49.34	52.82
Cu	< D.L.	< D.L.	< D.L.
Zn	108	94	152
La	5.274	2.366	2.781
Ce	11.08	5.605	7.126
Pr	1.37	0.865	1.116
Nd	5.488	4.391	5.62
Sm	1.442	1.667	1.843
Eu	0.431	0.909	0.621
Gd	1.695	2.09	2.288
Tb	0.302	0.374	0.39
Dy	2.01	2.505	2.526
Ho	0.424	0.534	0.532

**Table 3.2.** continued.

Sample	IN08017	IN08043	IN08044
Locality	Nuvvuagittuq	Nuvvuagittuq	Nuvvuagittuq
Age (Ma)	3750	3750	3750
Reference	3	3	3
Er	1.223	1.567	1.527
Tm	0.192	0.231	0.231
Yb	1.35	1.629	1.584
Lu	0.213	0.254	0.251
Hf	1.61	1.34	1.38
Th	0.408	0.078	0.451
U	0.15	0.13	0.12
Pb	2.21	0.97	2.66



presence of garnet (Cates et al., 2013; O'Neil et al., 2011, 2007). Sample *IN08017*, another cummingtonite-amphibolite, has a medium  $\text{Al}_2\text{O}_3/\text{TiO}_2$  ratio, while *IN08012*, *IN08043*, and *IN08044* are all cummingtonite-amphibolites with low  $\text{Al}_2\text{O}_3/\text{TiO}_2$  ratios (Cates et al., 2013), interpreted to have formed without residual garnet.

### **3.1.3.3. Analytical techniques**

Whole-rock samples were crushed and powdered at the Department of Geological Sciences of the University of Colorado at Boulder in agate mortars that were pre-cleaned with quartz sand and subsequently conditioned with small sample aliquots prior to powdering of the main sample mass. Care was taken in all steps to avoid contact with metal. Splits from homogenized powders were divided for major, minor, and trace element geochemistry (see Cates and Mojzsis, 2007) and further subdivided for separate HSE work at LabMaTer, Université du Québec à Chicoutimi, Canada. Samples *GR97M22*, *IN05013*, *IN05019*, *IN05021*, *IN05056*, *IN08012*, *IN08016*, *IN08017*, *IN08043*, and *IN08044* were analyzed using the isotope dilution method, and samples *GR9703*, *GR0019*, *GR0020*, *GR0030*, *GR0031*, *GR04064*, *GR04065*, and *IN05047* were analyzed using nickel-sulfur fire assay. Analytical techniques for both methods are described in full detail by Savard et al. (2010). Due to the nature of each technique, Re data are not available for the samples analyzed by NiS fire assay, and Rh data are not available for the samples analyzed by isotope dilution.

## **3.1.4. Results**

### **3.1.4.1. Protolith identification**

These Eoarchean mafic and ultramafic rocks, ranging between 8.64 and 35.69 wt% MgO, are strongly deformed, and metamorphosed samples require that their protoliths be identified to confirm their komatiitic origin. High eruption temperatures (1650°C; Green,

1975) at time of emplacement means that some komatiites could have assimilated sulfur from crustal rocks. If this happens, it is possible that an immiscible sulfide melt exsolved that extracted the HSE—and thus, any Late Veneer signature—from the magmas (Leshner and Keays, 2002). In their analysis, Maier et al. (2009) reported previously published data of komatiites known to be unassociated with sulfide deposits, and none of the samples described herein are associated with such deposits or with sulfide mineralization.

Ultramafic schists collected within a supracrustal enclave can be identified as being komatiitic by plotting their Cr abundances as a function of MgO wt% (**Figure 3.2**). The rationale behind this approach is that as a magma evolves, Cr will stay in the melt and become increasingly concentrated until chromite or a Cr-rich phase begins to crystallize at ~25 wt% MgO. Our ultramafic samples fall within this trend, while most mafic samples hover at around the MORB value for Cr (357.1 ppm; Kelemen et al., 2004), confirming that they are more evolved than the ultramafic samples.

Another approach to constrain the komatiitic affinity of our Eoarchean enclave samples is to evaluate them on the basis of their MgO, Al<sub>2</sub>O<sub>3</sub>, and TiO<sub>2</sub> abundances (e.g., Fiorentini et al. 2011). **Figure 3.3** shows the distinct chemical differences between the Munro-type, Barberton-type, and Ti-rich komatiites that identify them as separate populations. Although there is scatter, a clustering of the Munro-type komatiites is centered at Al<sub>2</sub>O<sub>3</sub>/TiO<sub>2</sub> = ~20 and the Barberton-type at Al<sub>2</sub>O<sub>3</sub>/TiO<sub>2</sub> = ~11. Our ultramafic samples plot within the scatter of these komatiite types. In contrast, the mafic samples do not plot within the komatiitic fields. This is not surprising, as fractionation of pyroxene and plagioclase will have altered their Al/Ti ratios.

Arndt (2008) has argued that cogenetic komatiite-basalt sequences would be expected

**Figure 3.2:** Chromium abundances of the ultramafic and mafic samples relative to previously analyzed komatiites from Fiorentini et al. (2011).

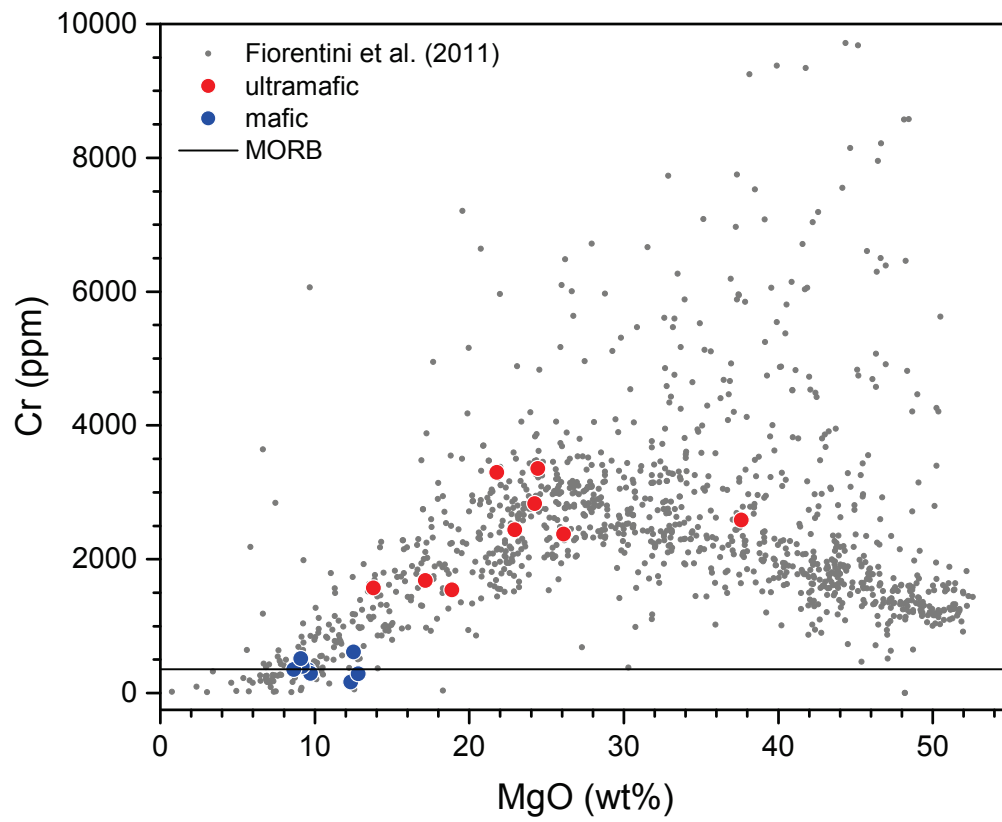
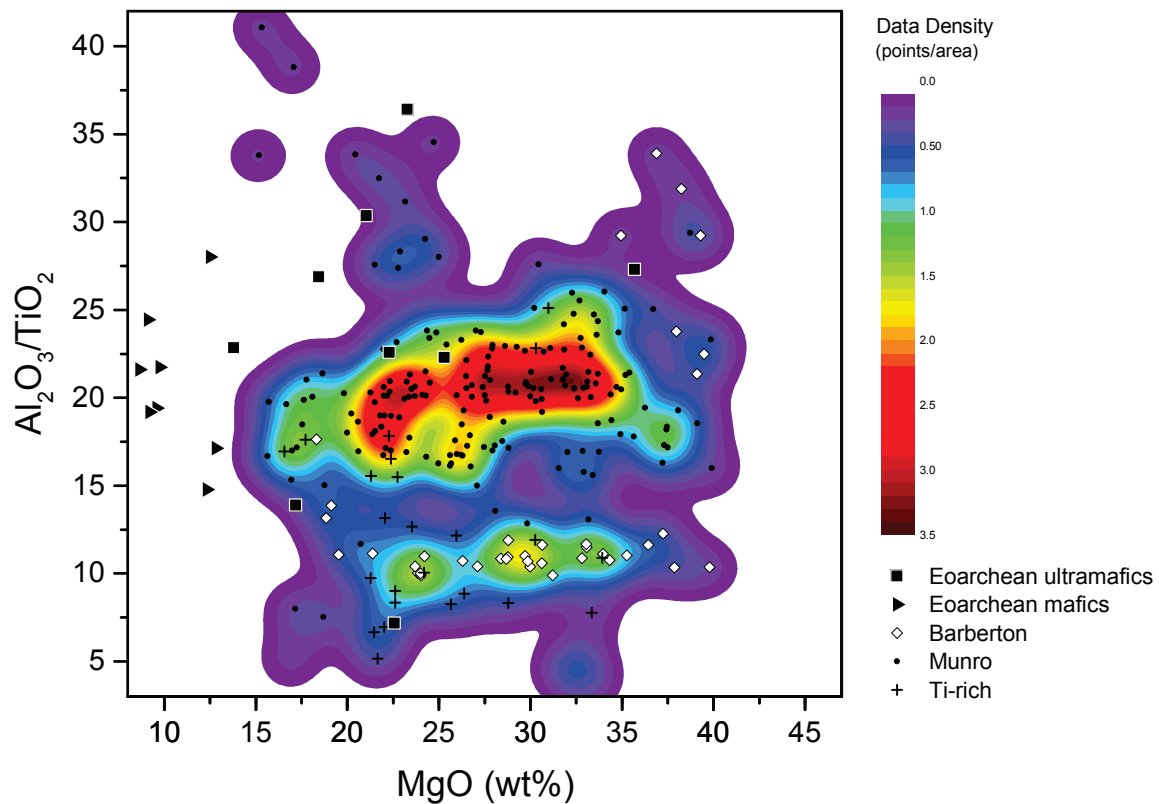
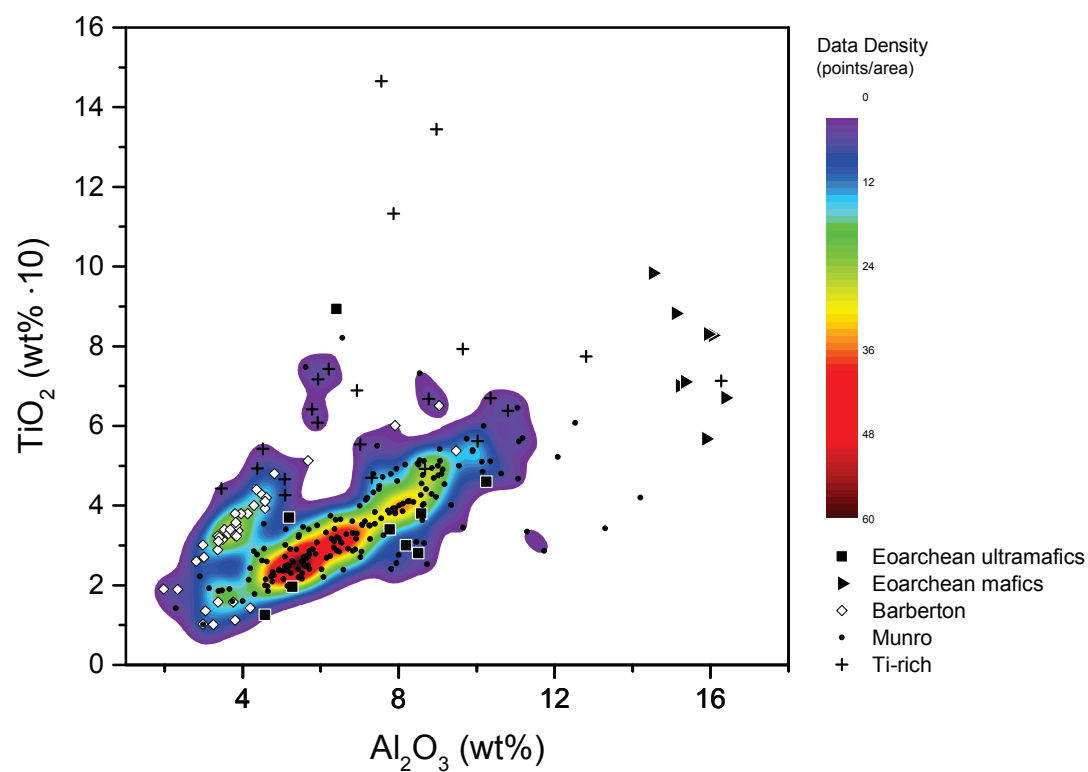


**Figure 3.3:** 2D kernel density plots for (A) MgO v.  $\text{Al}_2\text{O}_3$ , (B)  $\text{Al}_2\text{O}_3$  v.  $\text{TiO}_2$ , and (C)  $\text{Al}_2\text{O}_3$  v.  $\text{Al}_2\text{O}_3/\text{TiO}_2$ , comparing the samples reported here to previously identified komatiites presented in Maier et al. (2009). The color gradient indicates by the number of points per area smoothed out over the matrix that resulting from the 2D kernel density function. Black dots represent the Munro-type komatiites, open circles represent Barberton-type komatiites, crosses represent Ti-rich komatiites, and our new ultramafic and mafic data are shown by black squares and triangles, respectively. Figure 3A identifies a sample as ultramafic (>18 wt% MgO; Arndt, 2008), while  $\text{Al}_2\text{O}_3$  wt%,  $\text{TiO}_2$  wt%, and the ratio between the two are used to differentiate among the komatiite types (Al-depleted or Al-undepleted). Figures 3B and 3C plots show the distinctive chemical separation between Al-undepleted Munro-type and Al-depleted Barberton type komatiites.

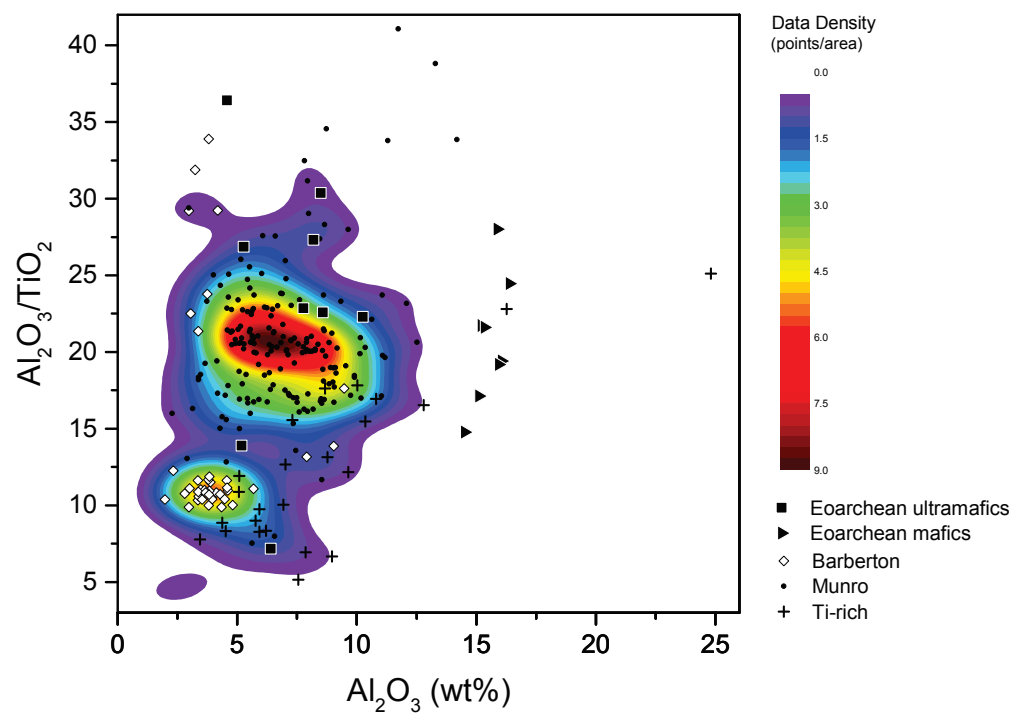
(A)



(B)



(C)



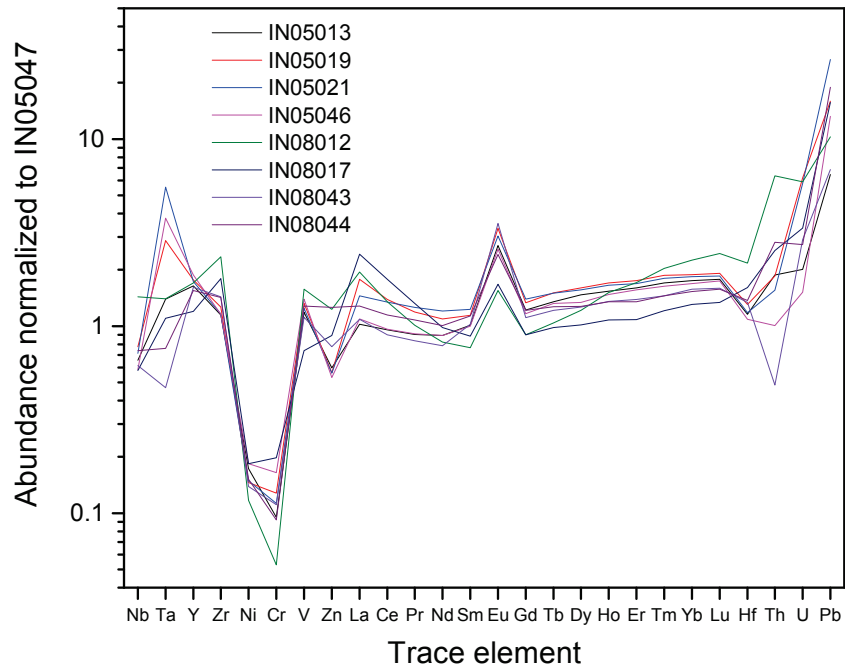
to show similar trace element patterns. **Figure 3.4** shows the trace element pattern of the mafic samples compared to Nuvvuagittuq ultramafic rocks. In terms of immobile and incompatible elements, the patterns overlap, with the exception of Nb and Th. The patterns also indicate that all samples represent mantle-derived magmas that experienced insignificant crustal contamination. The lack of sulfides means that the low PGE contents of the samples are not the result of sulfide segregation in response to contamination. To show that the mafic samples are cogenetic to the ultramafic samples, we normalized the trace element profiles of the former to the latter. Depletions in Ni and Cr are consistent with the degree of fractionation the derived melts should have experienced. Europium enrichments are likely due to its mobility.

#### **3.1.4.2. Highly siderophile elements in komatiites**

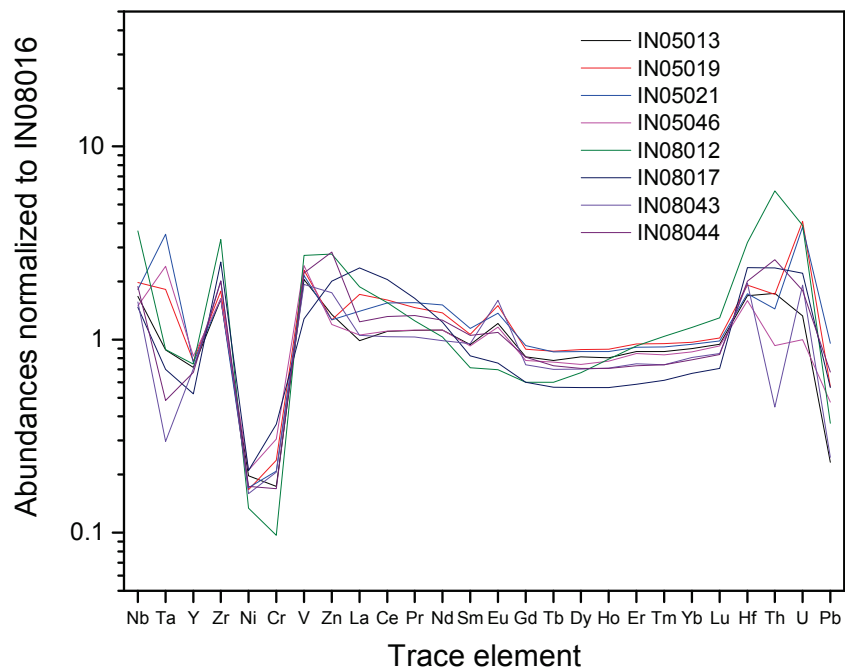
Platinum is incompatible during crystallization of sulfur-undersaturated komatiite magma, and thus Pt contents of the magma are expected to increase with degree of fractionation. To compare variably fractionated komatiites with each other and to deduce the nature of their mantle source, we normalized the Pt abundances in our samples to 25 wt% MgO. The normalization is performed by either subtracting or adding olivine to a komatiite by applying the lever rule. This normalization technique can also be applied to the mafic samples from Nuvvuagittuq because plagioclase and orthopyroxene only begin to crystallize in typical komatiitic melts at ~8.5 wt% MgO. We assume that olivine has the composition Fo<sub>93.5</sub> and 52 wt% MgO. Maier et al. (2009) focused on Pt because many of their komatiites were metamorphosed up to near greenschist facies, and Pt tends to be immobile even under those conditions. Palladium, on the other hand, has been shown to be mobile in some cases.

**Figure 3.4.** Normalized trace element concentrations of mafic samples from Nuvvuaguituq normalized to ultramafic samples (A) *IN05047* and (B) *IN08016*. Ratios close to 1 for relatively immobile elements indicate that the ultramafic and mafic samples at the localities have similar origins, allowing the mafic samples to be used as a complement to the ultramafic data.

(A)



(B)



Ruthenium does not need to be normalized in the same way because it has a bulk  $D$  of approximately 1 into the mantle during komatiite production (e.g., Maier et al., 2012).

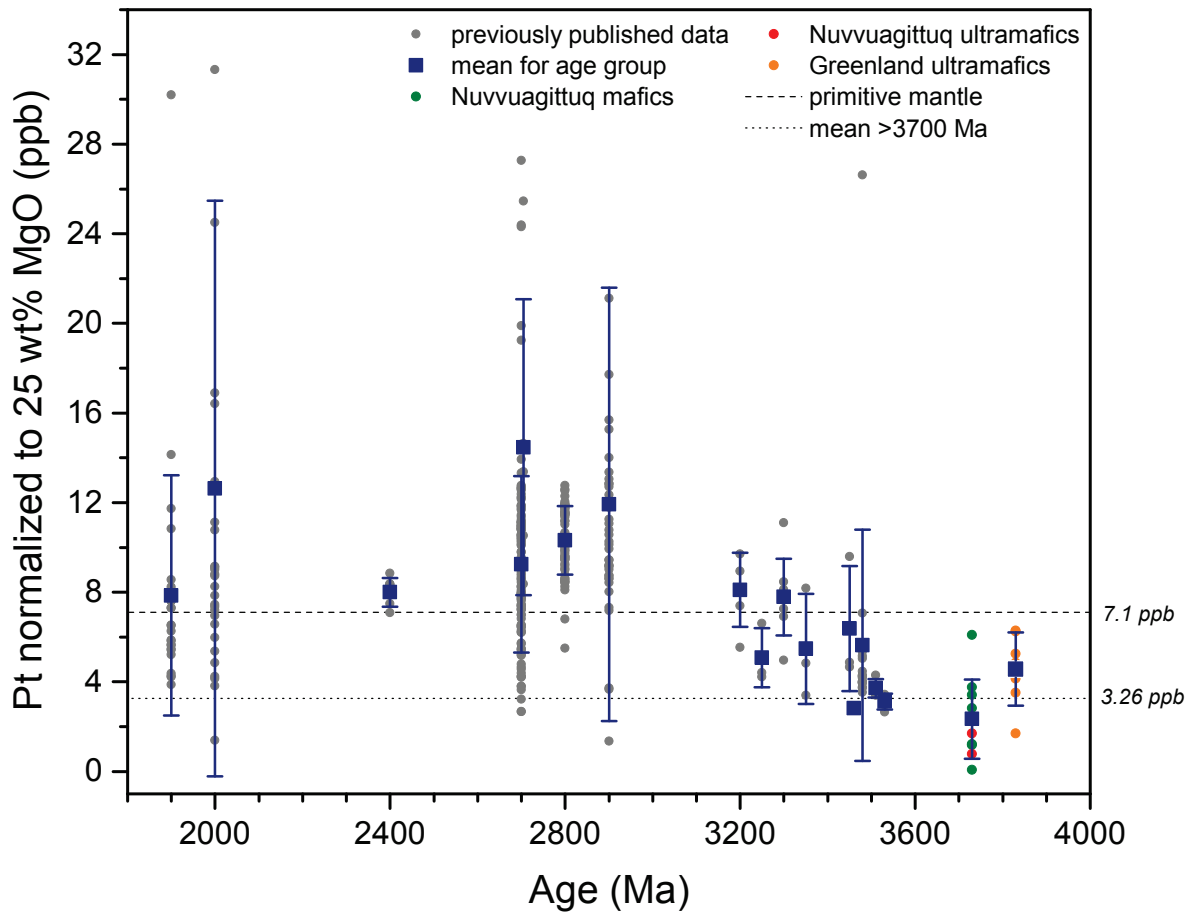
**Figure 3.5** shows the concentration of Pt and Ru in previously analyzed komatiites (Pt is normalized to 25 wt% MgO) along with the new data presented here. The mean concentrations for all samples of a particular age are also shown, as well as the two-sigma standard deviation for samples from any locality of a particular age. Ruthenium data for the mafic samples was not used here due to its compatible behavior and consequentially low concentration in evolved melts (see **Table 3.3** for the raw HSE data and **Table 3.4** for data normalized to 25 wt% MgO). Our new ultramafic HSE data continue the depletion trend previously observed by Maier et al. (2009) for samples older than about 3 Ga. This trend is confirmed in **Figure 3.6**, which shows linear regressions applied to age groups of data to within 95% confidence. For Pt and Ru, the average concentrations in the ultramafic samples prior to ca. 3.6 Ga are ~50 to 60% of the bulk silicate Earth (7.1 ppb Pt, 5.0 ppb Ru; McDonough and Sun, 1995). Sample *GR97M22* exhibited anomalously high Pd concentrations (**Table 3.3**), which can be ascribed to a “nugget effect” of the NiS fire assay technique. Although we report HSE abundances for this sample, they are not included in our trend analyses.

Whether schists of peridotitic composition represent komatiitic liquids or olivine-rich cumulates derived from basalt is a challenge, particularly if no primary mineral phases are available. The most reliable approach uses HSE data (e.g., Mouri et al., 2013). Komatiites have relatively unfractionated HSE patterns, whereas basaltic cumulates tend to have spiky patterns, often showing either depletion or enrichment of PPGE relative to IPGE that arises from the variable partitioning of the PGE into different cumulus phases. Primitive-mantle



**Figure 3.5:** The concentration of (A) Pt and (B) Ru in komatiites normalized to 25 wt% MgO. The new data reported here are all samples >3.6 Ga; all those younger are from Maier et al. (2009). Each black dot is a single sample analysis, the red circles show the mean concentration for all samples from any locality of a particular age, and the blue lines indicate a two-sigma standard deviation for samples from any locality of a particular age. The solid horizontal line shows the mean modern peridotite concentration of Pt or Ru, and the dashed line shows the calculated mean Eoarchean concentration for the mantle source from these data.

(A)



(B)

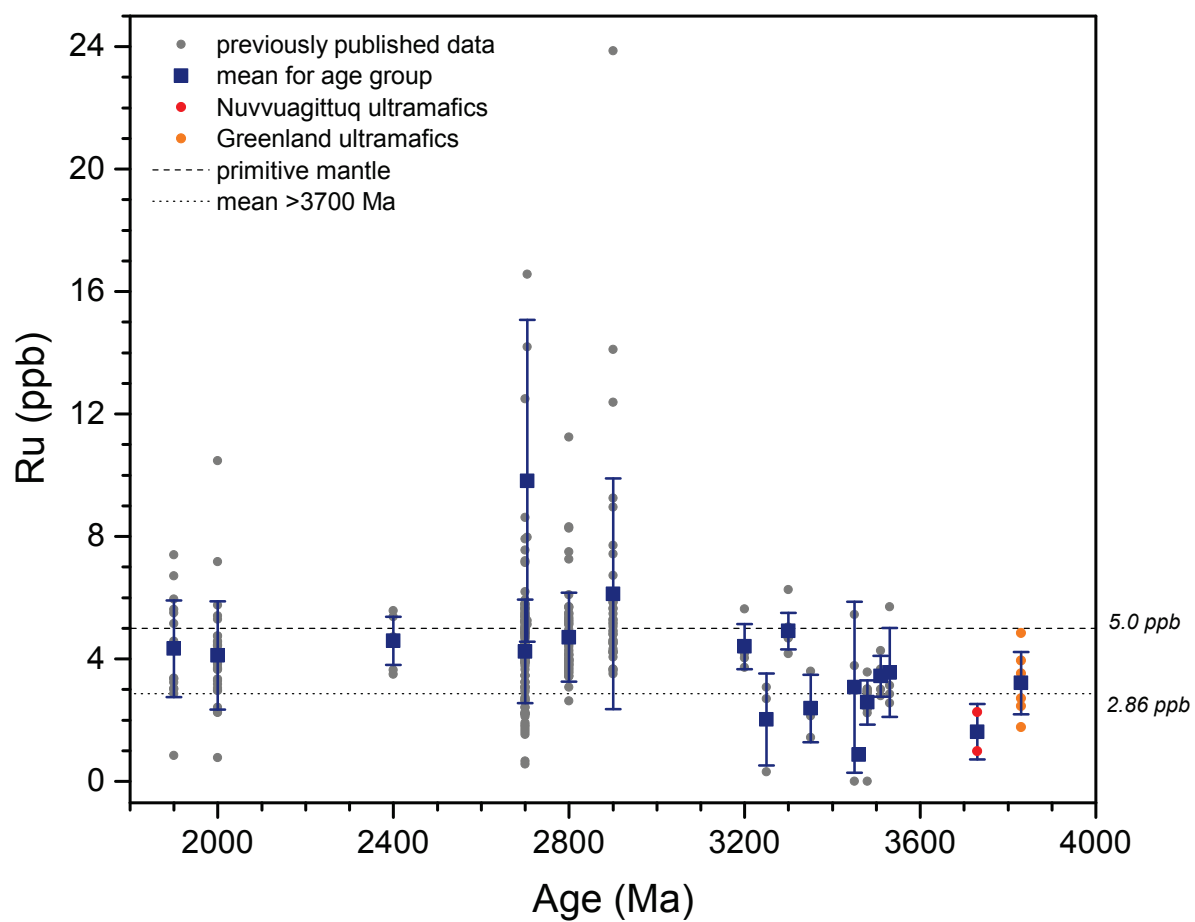


**Table 3.3.** HSE data for all ultramafic and mafic samples in order of decreasing MgO wt%. GR97M22 (italicized) is not included in the means show below or any analyses due to its high Pd, which indicates a possible problem in the analysis process.

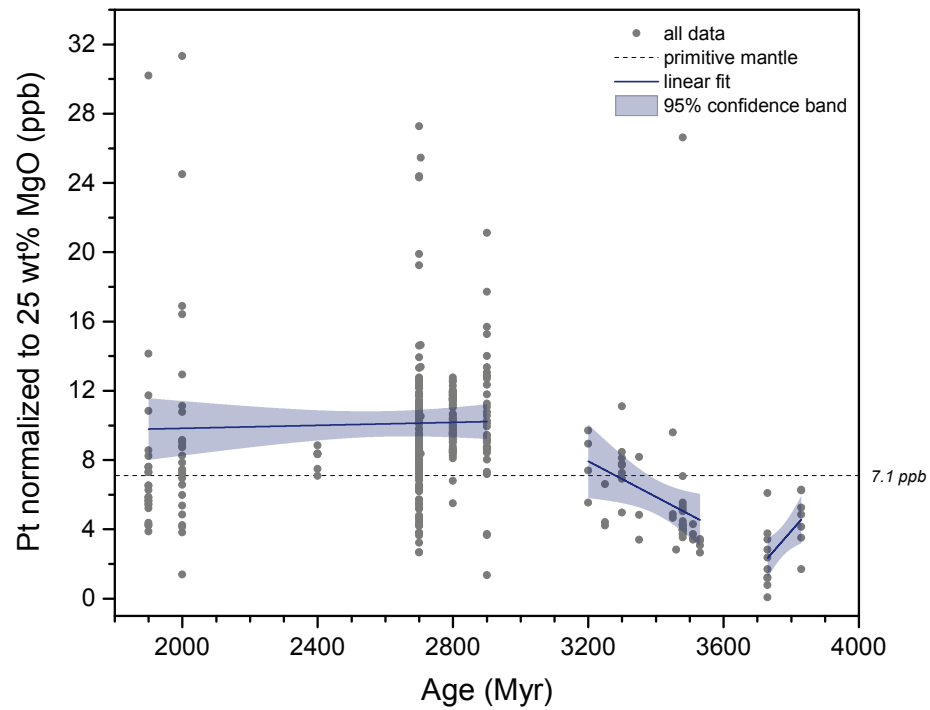
Sample	MgO (wt%)	Os (ppb)	Ir (ppb)	Ru (ppb)	Pt (ppb)	Pd (ppb)	Re (ppb)	Rh (ppb)
GR04064	35.69	1.19	1.24	3.94	2.50	0.97		0.78
<i>GR97M22</i>	<i>26.82</i>	<i>0.520</i>	<i>0.286</i>	<i>1.913</i>	<i>8.610</i>	<i>35.187</i>	<i>0.013</i>	
GR0020	25.3	0.813	0.729	3.246	6.217	7.221		0.844
GR0031	23.28	0.557	0.597	2.706	6.650	5.866		0.871
IN05047	22.56	1.49	0.85	2.26	1.86	2.49		0.28
GR/97/03	22.29	0.74	0.69	3.53	3.87	2.91		0.90
GR0019	21.03	1.236	1.190	4.848	6.019	6.789		1.053
GR04065	18.43	0.43	0.50	1.77	2.11	1.35		0.47
IN08016	17.17	0.252	0.175	0.983	0.993	4.889	1.267	
GR0030	13.8	0.430	0.575	2.460	6.867	3.760		0.997
IN08044	12.82	0.216	0.236	0.475	4.456	3.302	1.264	
IN08017	12.495	0.139	0.293	1.141	9.721	9.11	0.013	
IN08012	12.328	0.116	0.007	0.061	0.118	0.222	0.175	
IN05013	9.736	0.037	0.064	0.107	2.095	1.428	0.303	
IN08043	9.565	0.081	0.167	0.704	6.526	2.127	0.013	
IN05019	9.2	0.221	0.251	0.171	5.98	5.935	0.39	
IN05046	9.11	0.029	0.065	0.102	2.064	0.635	0.405	
IN05021	8.643	0.038	0.211	0.137	4.206	4.763	0.151	
<b>Mean</b>				1.685		4.250		
<b>Mean (ultramafic samples only)</b>				2.860		4.120		

**Table 3.4.** HSE data normalized to 25 wt% MgO for all ultramafic and mafic samples in order of decreasing MgO wt%. Corrected Ru data are not presented because its metal-silicate partition coefficient is near 1. GR97M22 (italicized) is shown but not included in the means show below or any analyses due to its high Pd, which indicates a possible problem in the analysis process.

Sample	MgO (wt%)	Correction Factor	Os (ppb)	Ir (ppb)	Rh (ppb)	Pt (ppb)	Pd (ppb)	Re (ppb)
GR04064	35.69	1.656	1.975	2.051	1.285	4.138	1.608	
<i>GR97M22</i>	<i>26.82</i>	<i>1.072</i>	<i>0.558</i>	<i>0.507</i>		<i>9.233</i>	<i>37.730</i>	<i>0.014</i>
GR0020	25.3	1.011	0.822	0.737	0.853	6.287	7.302	
GR0031	23.28	0.940	0.524	0.561	0.819	6.252	5.515	
IN05047	22.56	0.917	1.367	0.777	0.252	1.704	2.281	
GR/97/03	22.29	0.909	0.668	0.627	0.821	3.514	2.648	
GR0019	21.03	0.872	1.078	1.037	0.918	5.247	5.919	
GR04065	18.43	0.804	0.347	0.402	0.378	1.696	1.089	
IN08016	17.17	0.775	0.195	0.135		0.769	3.790	0.982
GR0030	13.8	0.707	0.304	0.406	0.705	4.854	2.658	
IN08044	12.82	0.689	0.137	0.149		2.820	2.090	0.800
IN08017	12.50	0.683	0.087	0.183		6.093	5.710	0.037
IN08012	12.33	0.681	0.072	0.004		0.074	0.138	0.109
IN05013	9.74	0.639	0.021	0.037		1.213	0.827	0.175
IN08043	9.57	0.636	0.047	0.096		3.762	1.226	0.007
IN05019	9.20	0.631	0.126	0.143		3.413	3.387	0.223
IN05046	9.11	0.630	0.017	0.037		1.175	0.361	0.231
IN05021	8.64	0.623	0.021	0.119		2.364	2.677	0.085
<b>Mean</b>						3.257		
<b>Mean (ultramafic samples only)</b>						3.829		

**Figure 3.6:** Linear regressions of (A) Pt and (B) Ru concentration trends in komatiites to 95% confidence.

(A)



(B)

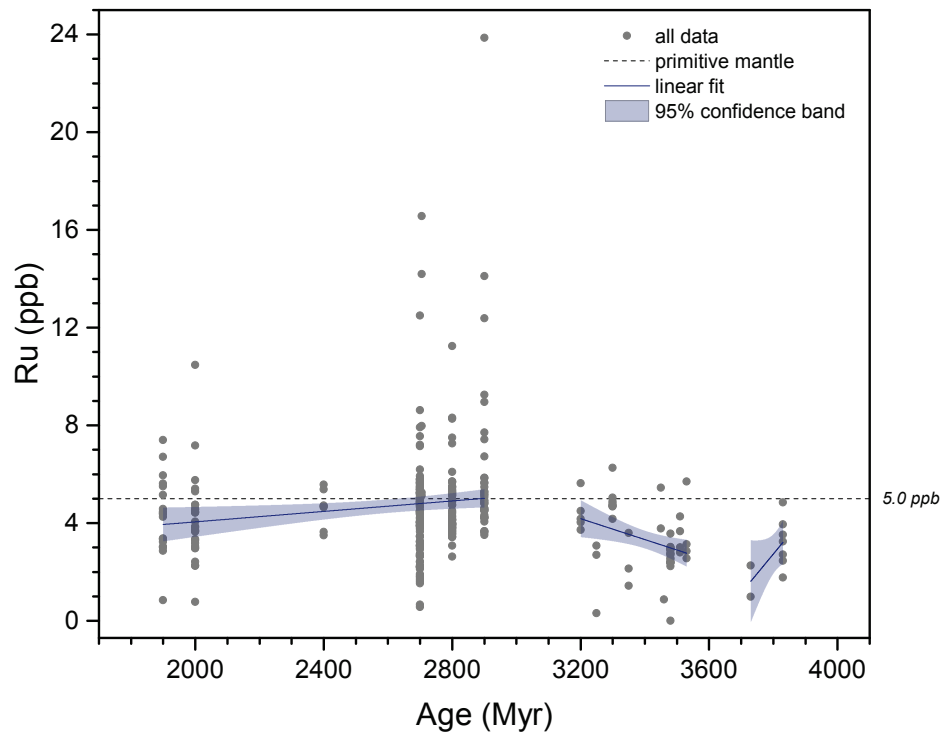
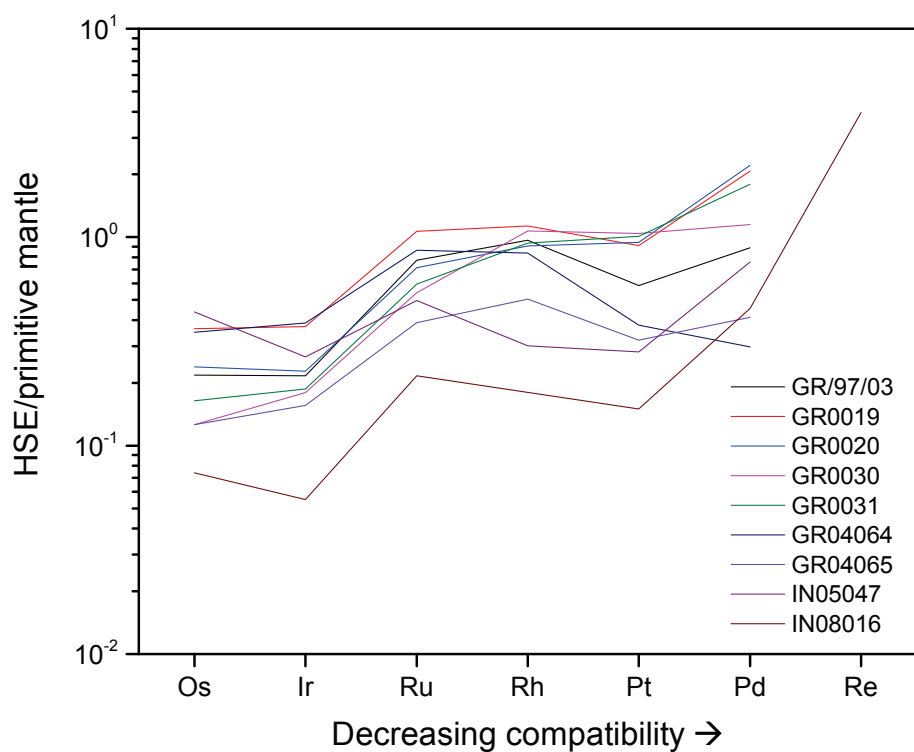
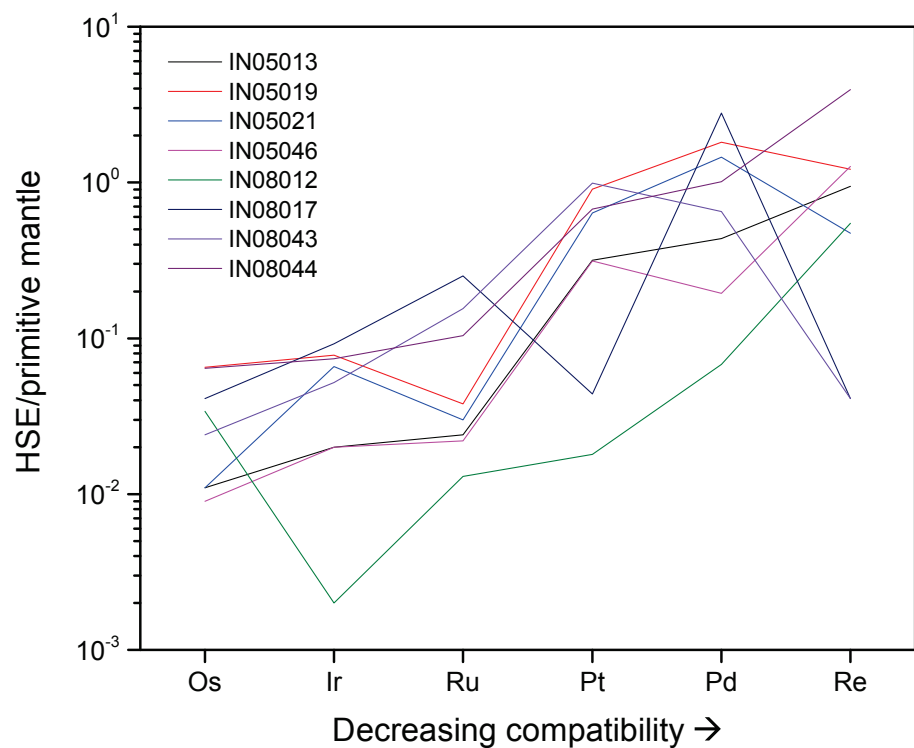


**Figure 3.7:** HSE abundances in (A) ultramafic and (B) mafic samples normalized to primitive mantle abundances from Palme and O'Neill (2003).

(A)



(B)



normalized (Palme and O'Neill, 2003) HSE spider plots for our ultramafic samples show relatively unfractionated patterns (**Figure 3.7A**), consistent with komatiites. The patterns of the mafic samples (**Figure 3.7B**) are more fractionated, with enrichment of PPGE over IPGE reflecting either more evolved mantle sources than the komatiites or more fractionation.

To confirm chondritic relative abundance trend for the HSE in mantle-derived rocks, we normalized the HSE data to CI chondrite concentrations of the relevant elements (Horan, 2003). **Figure 3.8A** shows the broadly chondritic patterns of the ultramafic samples we interpret to be komatiitic. **Figure 3.8B** shows the more scattered and less chondritic relative abundances of the mafic samples, which is expected given that these magmas formed at low degrees of partial melt relative to the komatiites. They may also be derived from more evolved melts, and thus experienced more fractionation between compatible and incompatible elements.

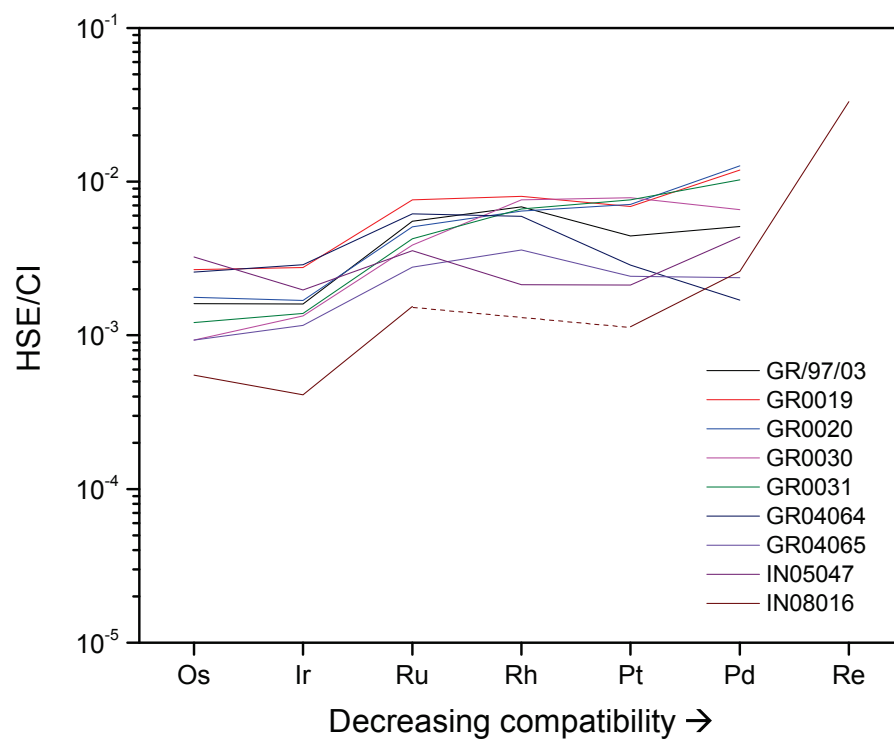
### **3.1.5. Discussion**

#### **3.1.5.1. Tungsten isotope systematics and the Late Veneer**

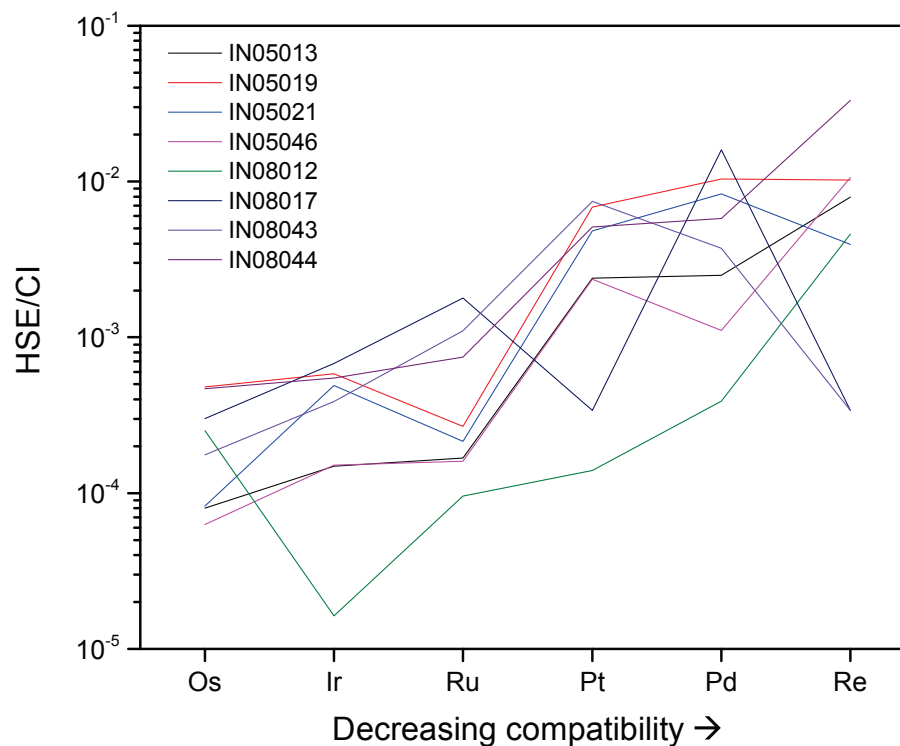
Several studies have explored whether W isotopic ratios in ancient rocks can be used as tracers of the Late Veneer. The  $^{182}\text{Hf}$ - $^{182}\text{W}$  system is useful for its ability to date early-solar system processes as a consequence of the different compatibilities of Hf and W. For example, Willbold et al. (2011) and Touboul et al. (2012) analyzed rocks older than approximately 2 Ga for their  $^{182}\text{W}$  concentrations and reported highly precise  $^{182}\text{W}/^{184}\text{W}$  ratios. Willbold et al. (2011) analyzed bulk rocks of a variety of lithologies (paragneisses, orthogneisses, amphibolites, and mafic schists) from the ca. 3.77 to 3.81 Ga Isua Supracrustal Belt in West Greenland for their W abundances. Because the upper mantle is severely depleted of

**Figure 3.8:** HSE abundances in (A) ultramafic and (B) mafic samples normalized to carbonaceous chondrite abundances from Anders and Grevesse (1989).

(A)



(B)





siderophile elements, including W, any deviations from the bulk mantle ratio should be resolvable. Indeed, their Isua samples show an average W enrichment of  $\epsilon^{182}\text{W} = +0.13 \pm 0.4$  compared to the standard. Strikingly, the mass of chondritic material required to explain the difference in  $\epsilon^{182}\text{W}$  between the modern mantle and the Isua samples (0.2 to 0.9% of Earth's current mass) is similar to that required to explain the HSE enhancement (~0.5% of Earth's current mass).

In the context of the Late Veneer hypothesis, this might imply that the Isua samples tapped a deep reservoir that had not yet been contaminated by late-accreted material. Similarly, Touboul et al. (2012) analyzed komatiites from the Kostomuksha formation in Russia (2.82 Ga) and the type-locality Komati Formation in South Africa (3.47 Ga) for W, Os, and Nd abundances. Analysis of four Komati samples showed  $^{182}\text{W}$  abundances indistinguishable from the terrestrial standard (La Palma) basalt, whereas the 18 Kostomuksha komatiites had an average of  $\epsilon^{182}\text{W} = +0.15 \pm 0.048$ , a clear excess of  $^{182}\text{W}$  comparable to that reported by Willbold et al. (2011). In contrast to the pre-Late Veneer explanation of Willbold et al., Touboul et al. interpret the excess as being derived from a mantle differentiation event that occurred while  $^{182}\text{Hf}$  was still extant, and that the differentiated reservoir was not thoroughly mixed back into the bulk mantle at the time that the Kostomuksha komatiites formed 2.8 Ga. To explain their W, Os, and Nd results for Komati and Kostomuksha, Touboul and co-workers formulated a mantle-mixing model to investigate how the Late Veneer could affect the isotope ratios for these elements. They concluded the mantle must have been incompletely mixed at the time of the Kostomuksha komatiites (2.82 Ga) and had not been completely homogenized by the Moon-forming event. If the Kostomuksha results are indicative of mantle conditions in the Neoproterozoic, they

represent an interesting challenge to the mantle mixing/homogenization models of Maier et al. (2009) and Willbold et al. (2011).

### 3.1.5.2. Archean “trickle-down” geodynamics

The notion of long and slow mantle mixing is an important component to the “trickle-down” (Arndt, 2009) model proposed by Maier et al. (2009). Once the Late Veneer material reached Earth, it had to have been delivered only to the upper mantle, and the komatiite reservoir(s) must have started off with near-negligible HSE abundances to later become contaminated as mixing progressed. This process steadily increased Pt and Ru concentrations as observed in komatiitic samples from about 3.8 Ga to 3.0 Ga. After that time, roughly modern-day peridotite HSE abundances are reached. If this interpretation is correct, by around 3 Ga, HSE pollutants from the upper mantle were well-mixed into the deep mantle komatiite reservoir. We note that this is consistent with the approximately 750-Myr mixing time suggested by  $\mu^{142}\text{Nd}$  measurements from Eoarchean rocks (Bennett et al., 2007; Carlson and Boyet, 2009; Roth et al., 2014) but is tenfold slower than that expected in convection models which lead to homogenization in less than ~100 Myr (e.g., Caro et al., 2006; Coltice and Schmalz, 2006). Recent analysis of a tholeiitic lava flow in the Abitibi Greenstone Belt (2.7 Ga) showed a positive  $\mu^{142}\text{Nd}$  anomaly, which Debaille et al. (2013) argued was evidence of a major geodynamical regime switch at about 3 Ga from stagnant-lid to mobile-lid plate tectonics. We note that this is also about the same time that HSE komatiite abundances appear to level off in our data. Furthermore, the positive  $\epsilon^{182}\text{W}$  anomalies presented by Willbold et al. (2011) for Isua, and from Touboul et al. (2012) for rocks as young as 2.8 Ga (Kostomuksha komatiites), provide additional evidence that the early mantle did not convect particularly rapidly. Alternatively, mantle mixing was incomplete in the Archean, and the

komatiite source was heterogeneous and/or there were independent mixing mechanisms such as subduction or plume ascent as opposed to intra-mantle convection. Our preferred interpretation is that results presented here are consistent with the  $^{142}\text{Nd}$  and  $^{182}\text{W}$  observations and protracted mantle mixing.

The Sm-Nd system does not only provide information on mantle mixing rates, but also what exactly was being mixed. Neodymium-142 excesses in rocks from Isua show that they were derived from a Hadean mantle depleted in highly incompatible elements (Boyet et al., 2003; Caro et al., 2006). The initial depletion of the early mantle would have occurred shortly after Earth's formation due to a global magma ocean differentiation or extraction followed by isolation of primordial crust. A differentiation event that formed the Isua depleted reservoir would have also formed a complementary enriched reservoir. Evidence for this was found in mafic dikes and the idea that mantle heterogeneities could be preserved until at least 3.4 Ga (Rizo et al., 2012). New combined Lu-Hf and Sm-Nd results from the Acasta Gneiss Complex show that the Hadean crust was re-worked and ultimately destroyed after about 1.5 Gyr (Guitreau et al., 2014; Roth et al., 2014).

Komatiites can provide further information on the postulated complementary Hadean reservoirs. Specifically, Sm/Nd and Lu/Hf ratios in early Archean komatiites are lower than those in Proterozoic komatiites, which suggests that an enriched reservoir and a depleted reservoir were mixed over time (Blichert-Toft and Puchtel, 2010). These isotopic systems as well as those of Rb-Sr and O show that the rate of continent growth was two-staged (Dhuime et al., 2012; Jacobsen, 1988). Dhuime et al. (2012) argued that Earth initially experienced a high rate of continental crust growth for the first ~1.5 Gyr, but at ca. 3 Ga the rate dropped. This may have been due to a shift in how continents are made and preserved as the mantle

transitioned to modern-day subduction-driven plate tectonics. Coincidentally, it is during this same time that Pt and Ru abundances in komatiites (**Figure 5.6**) appear to level off to approximately modern concentrations. The HSE may be an additional independent marker of a global shift in mantle behavior and mixing between reservoirs.

### **3.1.5.3. Late Veneers beyond Earth**

Observations of relatively elevated HSE concentrations in samples of mantle-derived rocks (or extrapolated from crustal rocks) of the Moon, Mars, and some meteorite parent bodies lend credence to the hypothesis of an extraterrestrial source for terrestrial HSE (**Table 3.5**). Taking into account the timelines and relatively enhanced HSE abundances in both small and large rocky bodies, it appears that late accretion (i.e., accretion after core formation) was a generic process that affected the silicate worlds of the inner solar system. Analyses of Apollo samples and lunar meteorites of basaltic origin show that although HSE are  $\sim 20\times$  less abundant in the lunar mantle compared to Earth's, the concentrations are still in chondritic relative proportions and elevated with respect to the abundances in the lunar crust (Day et al., 2010, 2007). This less dramatic enhancement of HSE concentrations in the lunar mantle can be accounted for by the early solidification of the lunar crust and resulting isolation of the Moon's mantle from late accretion impactors due to lack of mantle convection (Walker et al., 2004) and/or a stochastic delivery of late accretion material to the Earth-Moon system (Bottke et al., 2010). Mars' mantle also shows heightened HSE concentrations, as martian meteorites show comparable abundances to Earth's mantle in broadly chondritic proportions (Brandon et al., 2012; Dale et al., 2012; Jones et al., 2003). Highly siderophile element ratios in the samples appear to be independent of rock type but do show a range of how evolved their source reservoirs in the martian mantle were.

**Table 3.5.** HSE concentrations in the Earth, meteorites, and other planetary bodies. Data come from (1) Palme and O'Neill (2004), (2) McDonough and Sun (1995), (3) a calculation made by Day (2013) using data from Humayun (2011), (4) Horan (2003) and Walker et al. (2002), (5) Day et al. (2007, 2010), and (6) a calculation made by Day (2013) using the methods of Day et al. (2007) and data from Brandon et al. (2012).

Reservoir	Os (ppb)	Ir (ppb)	Ru (ppb)	Pt (ppb)	Pd (ppb)	Re (ppb)	Rh (ppb)	Reference
Primitive mantle	3.4	3.2	4.55	6.6	3.27	0.32	0.93	1
BSE	3.4	3.2	5	7.1	3.9	0.28	0.9	2
Bulk Core	2830			5290		247		3
Enstatite (avg)	637.4	582.7	873.3	1186	850.9	55.94		4
Ordinary (avg)	678.6	584.6	880.4	1185	657.9	58.38		4
Carbonaceous (avg)	642.6	608.5	862.2	1150	688.5	51.55		4
Lunar mantle	0.1	0.1	0.1	0.2	0.1	0.01		5
Lunar crust	0.0014	0.0015	0.007	0.016	0.03	0.0029		5
Martian mantle	3.7	3.3	5.3	3.7	2.3	0.3		6

To explain these observations, late accretion on Mars would have occurred in the time span between core formation (~5 to 30 Myr after solar system formation) and magma ocean solidification 50 to 100 Myr after it (Brandon et al., 2012). Hence, late accretion does not appear to be a process limited to the Earth-Moon system, nor was it exclusive to large rocky bodies. The diogenite/eucrite and angrite parent bodies experienced metal-silicate equilibrium followed by delivery of chondritic late accreted materials (Dale et al., 2012; Day et al., 2012; Riches et al., 2012). Heterogeneities in HSE between the samples from a single parent body may be a reflection on material that was delivered but not mixed to homogeneity in a magma ocean. The lack of difference in HSE concentrations between brecciated and non-brecciated diogenites suggests that late accretion must have occurred during or before magma ocean crystallization, perhaps 2 to 3 Ma after solar system formation (Day et al., 2012). Similarly, the angrite parent body likely experienced late accretion after core formation, and subsequent mantle mixing was rapid but inefficient (Riches et al., 2012). Late accretion appears to be a normal step in the process of solar system formation (Day et al., 2012).

#### **3.1.5.4. Alternate hypotheses to the Late Veneer**

The Late Veneer hypothesis is one of several that have been proposed to explain the HSE-enrichment in the Earth's mantle. Although Walker (2009) explored each hypothesis in considerable detail, we reevaluate two in the context of recent HSE analyses of Earth and beyond: (i) inefficient core formation and (ii) different partitioning behavior in a magma ocean. To remain viable, the hypotheses must explain the following observations: the HSE are present in Earth's mantle in chondritic proportions, samples from the Moon, Mars, and multiple parent bodies show enhancements that are also in chondritic relative proportions,

and Archean and early Proterozoic komatiites have lower HSE abundances than modern komatiites.

In hypothesis (i), metal fails to reach the core during differentiation and remains entrained with HSE in the mantle (e.g., Arculus and Delano, 1981; Jones et al., 2003). Models of inefficient core segregation calculate the partitioning behavior of elements between solid metal, liquid metal, solid silicate, and liquid silicate. An advantage of this hypothesis is that the amount of core material incorporated into the mantle to provide the HSE can be simply increased or decreased to match observations. Given the spread of partitioning behavior among the HSE ( $D^{met/ul} \sim 10^3$  to  $10^7$ ; Day, 2013), however, this hypothesis fails to explain their chondritic proportions in the mantle. Later work that advocated the inefficient core formation model focused on HSE analyses of abyssal peridotites that showed chondritic relative abundances but non-chondritic ratios among the elements (e.g., Ru/Ir, Pt/Ir, Rh/Ir, and Pd/Ir; Snow and Schmidt, 1998). It was suggested that the source was fragmented outer core material entrained in deep mantle plumes. In light of the HSE analyses of komatiites reported here and in previous work, this hypothesis makes implications that are at odds with the komatiite observations reported herein. If both Archean and Proterozoic komatiites come from lower mantle, the expectation is that they should have similar HSE concentrations if these are controlled by a core component. The inefficient core formation hypothesis can likely be ruled out.

Hypothesis (ii) proposes that instead of a late accretion event, the elevated HSE concentrations could arise from changes in partition coefficients in response to different pressure and temperature conditions in a magma ocean. Lower partition coefficients can cause different metal-silicate equilibration in the early mantle (c.f. Ringwood, 1977). The base of a

magma ocean meets the criteria where high temperatures and pressures lead to lower metal/silicate partitioning coefficients for the HSE and a weaker HSE fractionation into core-destined metal. Experiments with moderately siderophile elements at temperature, pressure conditions, and fugacities consistent with the base of a terrestrial magma ocean 400 to 700 km deep are broadly in line with the hypothesis (e.g., Drake, 2000; Righter and Drake, 1997). Similar experiments for the HSE have yielded conflicting results (see Walker, 2009 for a comprehensive review). Either way, this hypothesis does not satisfactorily explain the enhanced, chondritic HSE concentrations recently measured in asteroid parent bodies via meteorites (Dale et al., 2012; Day et al., 2012; Riches et al., 2012). These small bodies were not capable of supporting the global magma oceans on the scale that the Earth, Moon, and Mars are believed to have experienced (e.g., Elkins-Tanton et al., 2011). While it is possible this behavior contributed in part to elevated HSE concentrations in Earth's mantle (Mann et al., 2012), it does not provide a singular explanation for small bodies.

### **3.2. Dynamical modeling**

Understanding the mechanism and dynamical parameters by which excess HSE were delivered to Earth's mantle is key to justifying an extraterrestrial explanation for their enrichment. Geochemical analyses cannot currently differentiate between the impact of a single large projectile and multiple impacts of smaller bodies, but constraints can be generated via geophysical limitations and dynamical likelihood. For example, a single large planetary object that is 2500 to 3000 km in diameter and formed early in solar system history is large enough to be differentiated (McSween et al., 2002). In the case of such an impactor, its HSE should be sequestered in its core. The number of suitably large impactors at the time of the



Late Veneer was probably small (Bottke et al., 2010). A further requirement is that if such a large impactor hit Earth, the HSE lodged within its core must have remained suspended in Earth’s mantle. The dynamical modeling results of Bottke et al. (2010) make this hypothesis plausible had the strike been a “hit-and-almost-run” event that shattered the impactor’s core as it collided with Earth. In this scenario, a spiral of debris around Earth rains back down to the surface (Asphaug, 2010).

A multi-impactor scenario is also possible: the Late Veneer could have arrived through a fleet of small, oxidized bodies, removing the problem of keeping a large impactor core away from Earth’s core. The multi-impactor solution introduces a problem of numbers, however, such as whether there are enough small impactors available to deliver  $\sim 0.5\%$  Earth’s current mass. For reference, the asteroid belt is  $\sim 0.06\% M_{Earth}$  (Krasinsky, 2002). The Late Veneer Earth/Moon HSE enrichment ratio is  $\sim 1200$ , but the impact number flux ratio for both late-accreting planetesimals and present near-Earth objects are  $\sim 20$  (Bottke, 2002; Bottke et al., 2007; Nesvorný et al., 2010) and  $\sim 50$  for micrometeorites (Nesvorný et al., 2010). In their dynamical simulations of potential Late Veneer impactors, Bottke et al. (2010) explored the parameter space of plausible impactor flux ratios that depend on timing and impactor composition, concluding that the stochastic nature of large impacts is the most viable explanation for the anomalous impactor flux ratio.

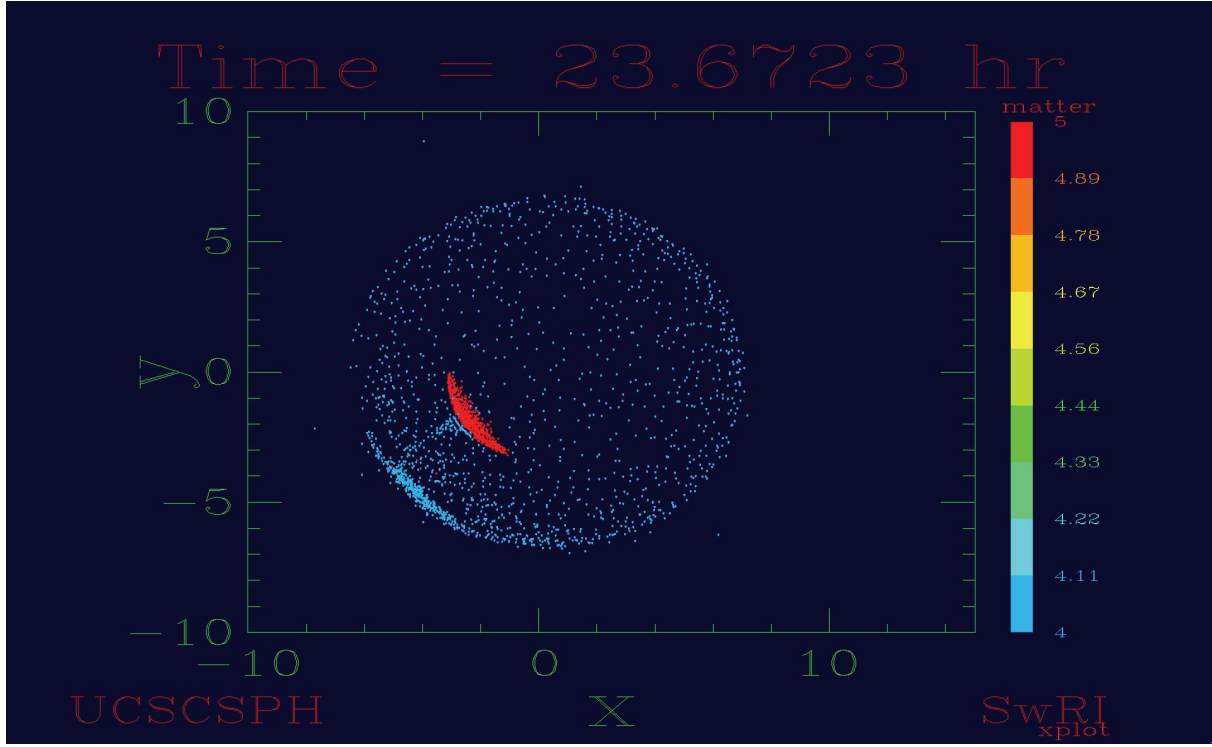
What remains to be tested is whether the proposed “hit-and-almost-run” scenario is feasible. The first steps to testing this have been taken by employing the same smooth particle hydrodynamics (SPH) code used to model the Giant Impact (e.g., Canup, 2008). SPH can handle mixed materials with certain densities based on their composition, making it ideal for tracking particles from different layers of a differentiated body. The code models the

interaction of spherical, symmetric particles over time by tracking material (metal or silicate), position, velocity, density, gravity, pressure forces, temperature, and shock dissipation of each individual particle. Acceleration due to pressure, artificial viscosity, and gravity are calculated using the conservation of momentum, and the rate of change in internal energy due to pressure and artificial viscosity is computed from the conservation of energy. Equations of state describe a particle's internal energy and density at each time step. The goal here is to explore the parameter space of varying the impact velocity (1.1, 1.2, 1.3, and 1.4 times Earth's escape velocity), impact angle ( $30^\circ$ ,  $45^\circ$ , and  $60^\circ$ ) and impactor mass (1%, 0.5% and 0.1%  $M_\oplus$ ). Thus far, the simulations for the 1%  $M_\oplus$  scenario have been performed; those for 0.5% and 0.1%  $M_\oplus$  remain as future work.

There is a caveat in the interpretation of these simulations. Because the SPH code is computationally limited to a resolution of 100 km, it cannot account for any small-scale processes that may occur when impactor fragments penetrate Earth's mantle. For example, a simulation that resulted in the impactor core particle reaching Earth's core cannot account for emulsification, which occurs on cm scales (Dahl and Stevenson, 2010). Rather, the focus of these simulations is to determine the conditions under which the impactor's core shatters, resulting in the hit-and-almost-run scenario that populates Earth's upper mantle with core material, and therefore, HSE.

For example, the  $v_i/v_{esc} = 1.1$ ,  $\angle_{impact} = 30^\circ$  simulation resulted in all of the impact core material going to Earth's core (**Figure 3.9**), which is a questionable result considering the resolution limits of the code. What is noteworthy, however, is that the impactor core was not shattered upon impact, which is inconsistent with the hit-and-almost-run scenario that permits a differentiated impactor to strike the Earth without its core merging with Earth's.

**Figure 3.9.** Final frame of the  $\rho_i/\rho_{esc} = 1.1$ ,  $\angle_{impact} = 30^\circ$  simulation.



Furthermore, the impact was clearly capable of melting the surface of the Earth, sterilizing the surface of any life that may have been present at that time.

This shattering did occur with the  $\rho_i/\rho_{\text{esc}} = 1.5$ ,  $\angle_{\text{impact}} = 60^\circ$  simulation; a spiral arm of debris can be clearly seen (**Figure 3.10**). **Figure 3.11** shows the final time step, this time with red representing core metal and blue representing silicate mantle. The particles that remain at Earth at this time step appear to remain suspended near its surface despite the exclusion of small-scale processes in the model. However, the simulation was not run for long enough to determine where the flung particles would end up, whether they would overcome Earth's escape velocity or return back to Earth.

Qualitative results are presented in **Figure 3.12**, preliminarily showing that the large impactor hit-and-almost-run scenario preferentially requires a shallow, high-velocity impact. From the simulations it seems that impact angle is a larger factor than impact velocity. Further work using 0.05% and 0.1%  $M_\oplus$  in the model are required to determine the cutoff at which the size of the impact does not pose a problem for HSE suspension in the mantle.

### 3.3. Conclusions

Earth's geological activity has erased nearly all tangible records of its earliest history. Late accretion is one of the processes that any young planetary body may experience following differentiation. The Late Veneer signature can be read in the HSE abundances of Archean and Proterozoic komatiites, which we interpret as a recording of progressing mixing of this primordial pollutant into the deep mantle. New data presented here for >3.7 Ga ultramafic rocks from the Nuvvuagittuq and Akilia localities extend this record back to the oldest known

**Figure 3.10.** Spiral arm of debris from the  $\rho_i/\rho_{esc} = 1.5$ ,  $\angle_{impact} = 60^\circ$  simulation. Red particles are metal from the impactor core and blue particles are from the impactor mantle.

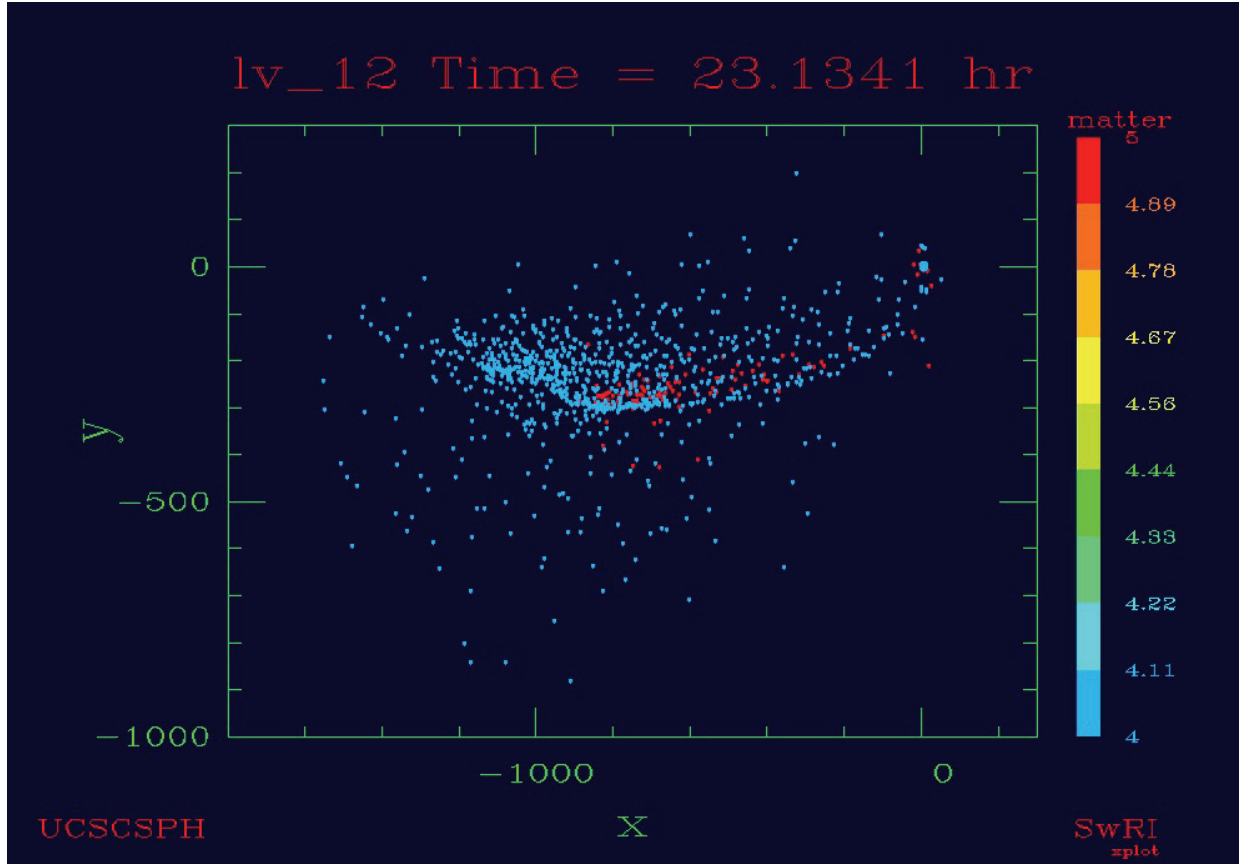
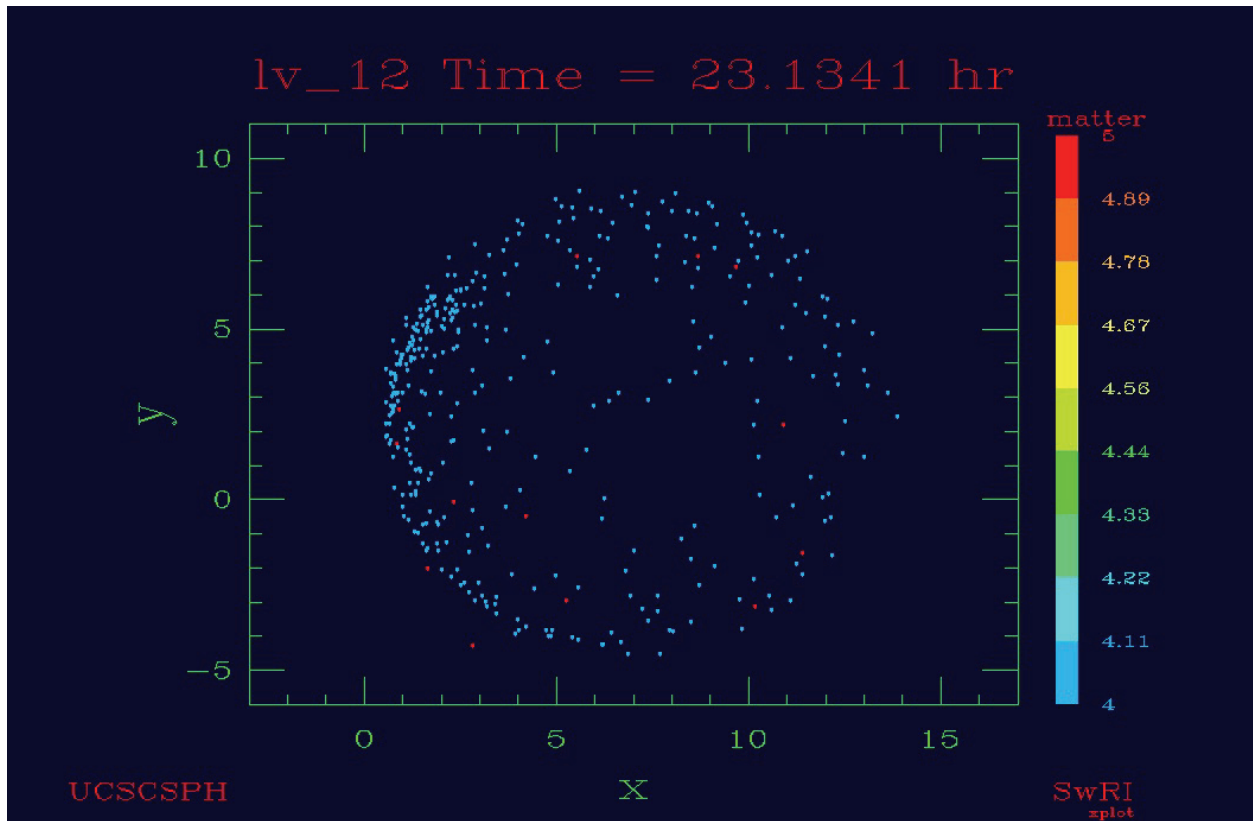


**Figure 3.11.** Zoomed-in frame of Figure 3.10 showing particles relative to the Earth. No core particles have entered Earth's core. Red particles are metal from the impactor core and blue particles are from the impactor mantle. Earth particles have been removed for clarity.



rocks of komatiite protolith, showing depletions of HSE that are ~60% of the concentrations in modern peridotites. Furthermore, SPH simulations of a single-impactor scenario indicate that even an endmember mass of 0.1%  $M_{\oplus}$  permits, under certain conditions, the hit-and-almost-run scenario hypothesized to cause the enrichment.

Alternative explanations for the enhanced HSE mantle abundances such as inefficient core formation and various mantle equilibration scenarios have been invoked, but none is able to explain by itself the chondritic relative abundances of these elements given that their metal-silicate partitioning behaviors are not identical. Additionally, the growing body of evidence of late accretion events beyond Earth (Dale et al., 2012; Day et al., 2010, 2007; Jones et al., 2003; Riches et al., 2012) requires that an explanation for these abundance trends must also be able applicable to the Moon, Mars, and small bodies. It may very well be that for Earth, the Late Veneer lies on the impact-scale continuum between the Giant Impact and the Late Heavy Bombardment and simply represents another milestone for planetary maturation in the construction of our solar system.

## Chapter 4: An integrated perspective on habitability

Provided with a coupled model for the geochemical and thermal evolution of planets, we can begin to evaluate the limits of their habitability. Even if a particular planetary body is habitable at some point, it will not be so within its entire volume and over the course of its entire history. These are subtleties that are not captured by the classical concept of the “habitable zone,” which is defined as an annulus around a star that permits liquid water to exist on the surface of a solid planet with a sufficient atmosphere (Hart, 1979). The definition of the habitable zone needs to be expanded to account for the limits of time and the possibility of regions in a solar system beyond that annulus that might be hospitable. Knowledge about the constraints of planetary habitability can be applied to exoplanets in the search for life beyond our solar system.

### 4.1. Space-limited habitability in the solar system

By defining a zone where terrestrial extremophiles could theoretically be transplanted and survive, we can evaluate the spatial limitations of habitable environments in the solar



system and estimate its total habitable volume. Earth's documented extremophile inventory provides environmental constraints for temperatures of approximately  $-20$  to  $121^{\circ}\text{C}$ , a pH range of 0 to 13, salinities  $\leq 35\%$  NaCl, and gamma radiation doses as high as 10 to 11 kgrays (Baross et al., 2007). Collectively, these criteria can be applied to the silicate planets, large asteroids, icy satellites, and small icy bodies to determine their geophysical habitable volumes using the current state of knowledge about their surfaces and interiors.

Of the four silicate planets, Mercury is the least likely to have ever supported life. It receives intense solar radiation, has a tenuous atmosphere, and is geologically moribund. Venus' layer of  $\text{H}_2\text{SO}_4$  clouds  $\sim 48$  to  $65$  km above its  $460^{\circ}\text{C}$  surface allows for mild temperatures of  $27$  to  $77^{\circ}\text{C}$  (Schulze-Makuch et al., 2004). This cloud layer is extremely acidic (pH  $\sim 0$ ), but thermoacidophiles on Earth can live at pH 0 and up to  $65^{\circ}\text{C}$  (Fütterer et al., 2004). With water present, Venus' atmosphere could in principle support a phototrophic biosphere, and chemotrophs might garner energy from the reduction of  $\text{SO}_2$  to  $\text{H}_2\text{S}$  or COS (Schulze-Makuch et al., 2004). Thus,  $\sim 10^9$  km<sup>3</sup> of Venus' atmosphere may be considered habitable regardless of whether life is actually present. On Earth, the biosphere extends from  $\sim 10$  km altitude to  $\sim 10$  km into the oceans and  $\sim 5$  km into the continental crust (Jones and Lineweaver, 2010). This results in a volume equivalent to  $\sim 1\%$  of Earth's geophysical and tropospheric volume, leading to a minimum biospheric volume of  $\sim 10^{10}$  km<sup>3</sup>. In contrast, Mars' desiccated surface and rarified atmosphere limits its potentially habitable volume to the subsurface. Fluvial geomorphology indicates a subsurface cryosphere because water stored in the polar caps is insufficient to have carved the observed features. An analysis taking into account such factors as thermal conductivity, porosity, cryosphere extent, and heat flow suggests that Mars has about  $10^7$  km<sup>3</sup> of potentially habitable groundwater beneath its cryosphere (Clifford et al., 2010).

Ceres is the largest asteroid in the asteroid belt and may possess a subsurface ocean. Despite being only ~950 km in diameter and lacking the tidal heating that moons such as Europa and Enceladus enjoy, a warm surface temperature (-93°C) and radiogenic heating could still sustain liquid water and replenish radiolysis products in its interior (Castillo-Rogez and McCord, 2010). Detection of serpentinization products (Rivkin et al., 2006) and the homogeneity in which they are found (Carry et al., 2012) suggest recent or even ongoing geological activity, which is strongly supported by the recent report of plumes (Küppers et al., 2014). In icy mantles without silicate hydration, antifreeze substances such as hydrates, carbonates, and chlorides depress the H<sub>2</sub>O eutectic to -83°C; ammonia drops it to -97°C. Which solute species are present in its interior ocean depends upon Ceres' starting composition and thermal evolution. Assuming a 75-km thick icy crust and a 10-km deep watery mantle in contact with warm (approximately 127 to 227°C) rock as modeled by Castillo-Rogez and McCord (2010), the volume of Ceres' habitable putative ocean is ~10<sup>7</sup> km<sup>3</sup>.

Gas giants are hostile to life, but their icy satellites offer more hospitable environments. The icy moons Europa and Triton likely have water ice crusts several tens of km thick and even thicker oceans expressed as liquid water mantles (Hussmann et al., 2006), while tiny Enceladus was recently confirmed to have at minimum a pocket of liquid underlying its cryovolcanically active South Polar Terrain (Iess et al., 2014), which does not rule out the possibility of a global subsurface ocean. Because hydrothermal systems supply reducing nutrients to support chemoautotrophy on Earth, subsurface oceans could contain similar environments if in contact with silicate mantles that experience melting. Assuming crust thicknesses of 50 km and ocean thicknesses of 100 km (although these figures are an active area of debate), the cumulative habitable volume of the small icy satellites is ~10<sup>9</sup> km<sup>3</sup>,

comparable in volume to Earth's oceans ( $1.3 \times 10^9 \text{ km}^3$ ). The larger icy satellites Titan, Ganymede, and Callisto could also possess significant liquid water, but any oceans would probably be sandwiched between ice layers with no contact with rock, severely limiting nutrient cycling (Sotin and Tobie, 2004). Should nutrient recycling be achieved, crust and ocean thicknesses of 50 km and 100 km (Vance et al., 2007) give a cumulative habitable volume of  $\sim 10^{10} \text{ km}^3$ .

Trans-neptunian objects (TNOs) are cold, dark planetesimals in the Kuiper belt, scattered disk, and Oort cloud. Aided by radiogenic heating, TNOs  $\geq 800 \text{ km}$  in radius (e.g., Sedna) may maintain liquid water oceans over geologic timescales despite surface temperatures of  $-233^\circ\text{C}$  (Hussmann et al., 2006). Population estimates suggest that of the  $\sim 10^9$  Kuiper Belt objects  $\geq 1 \text{ km}$  (Schwamb et al., 2010), at least 40 are Sedna-like (McFadden et al., 2010). Assuming the same size distribution for the  $\sim 4 \times 10^{11}$  Oort Cloud bodies (Levison et al., 2010), the population of  $\geq 800$  diameter TNOs exceeds  $10^4$ . If these large TNOs are Sedna-sized, the resulting cumulative habitable volume for TNOs is  $\sim 10^{12} \text{ km}^3$ , corresponding to 1,000 Earth oceans.

Surprisingly, the habitable volume of our solar system may be dominated by veiled oceans within the largest TNOs, akin to postulated cold, sunless bodies meandering in interplanetary space (Stevenson, 1999), whose existence has been confirmed through gravitational lensing observations (MOA and OGLE Collaborations, 2011). Since G-type stars like our Sun make up approximately 4% of the 90 billion main sequence stars in the galaxy (Carroll and Ostlie, 2007), we posit that the geophysical habitable volume of the Milky Way could be  $\sim 10^{21} \text{ km}^3$ , equivalent to about  $9 \times$  the volume of our Sun. While, volumetrically, most of the solar system is uninhabitable for life, space is not the biggest hurdle in the development of life. That culprit might be time.

## 4.2. Time-limited habitability in the cosmos

There must be bookends to the period of a planet's habitability: when is too soon for life to take hold on a planet, and when is it too late for continued survival?

### 4.2.1. Its rise

It is unknown—and unlikely to ever be known—when life first arose on Earth. It is possible but not testable that life in one form or another arose multiple times only to be erased by the powerful impacts that Earth experienced in its formative years (Maher and Stevenson, 1988). The earliest evidence in the morphological fossil record dates back to 3465 Ma (Schopf, 1993), but the isotopic record has pulled the curtain back to 3850 Ma (Mojzsis et al., 1996). Such discoveries are clear upper limits to when the origin of life occurred; it is plausible that it happened earlier but the record has since been erased. An oft-cited geological lower limit is the poorly constrained timing of the Moon-forming Giant Impact, estimates of which date the event between 30 and 100 Myr after solar system formation (Jacobson et al., 2014; Rudge et al., 2010b). Had life been present at that time, it would stand no chance against an impact event that shattered the impactor, melted and scattered much of Earth's mantle, and formed a satellite from the remains (Canup, 2008). Due to the undeniable violence of the Giant Impact, the surface of the Earth was no doubt sterilized (Sleep et al., 2001).

The Late Heavy Bombardment (LHB) is generally thought of as a less violent but more protracted event than the Giant Impact, delivering only  $\sim 2 \times 10^{20}$  kg of material, whereas the Giant Impact projectile was on the order of Mars' mass (**Figure 1.1**). Though still a distinctly large event in the impact history of the Earth-Moon system, the LHB has been shown to have not been sufficiently powerful to have sterilized the Earth as did the Giant

Impact (Abramov and Mojzsis, 2009; Abramov et al., 2013; Marchi et al., 2014). In fact, it even explains why the last common ancestor appears to be thermophilic or hyperthermophilic (Pace, 1997): the transient heat delivered to Earth's crust would have supported long-lived hydrothermal systems in which such organisms could develop (Abramov and Mojzsis, 2009). While the LHB might have influenced the evolutionary path of life on the nascent Earth, it did not extinguish it.

Although the Giant Impact and the LHB were major milestones in the impact flux of the Earth, the Late Veneer, which is along the mass continuum between the two, has not previously been considered in the context of the origin of life. As explained in §3, the timing of the Late Veneer is poorly constrained, having occurred following the Giant Impact but before the formation of the oldest known zircon  $\sim 4.37$  Ga (Harrison, 2009; Valley et al., 2014). Exploration of endmember scenarios for mass delivery during the LHB shows that only a tenfold increase in the LHB impact flux is required to melt most of the volume of the crust (Abramov and Mojzsis, 2009). Considering the Late Veneer was  $\sim 0.5\%$  of Earth's current mass, or  $\sim 2250$  times the size of the LHB, the Late Veneer no doubt would have formed a shallow magma ocean, sterilizing the surface of the Earth. As such, it can be considered a firm bookend to the reign of life on Earth: the iteration of life from which we originate must have arisen no earlier than the Late Veneer.

#### **4.2.2. Its demise**

No one knows when in the distant future Earth will become inhabitable. Climate change and asteroid or comet strikes notwithstanding, the natural lifetimes of stars and geological activity are likely to be the most serious limiting factors for Earth's global-scale habitability. As discussed in §2, radiogenic heating plays a key role in maintaining the internal

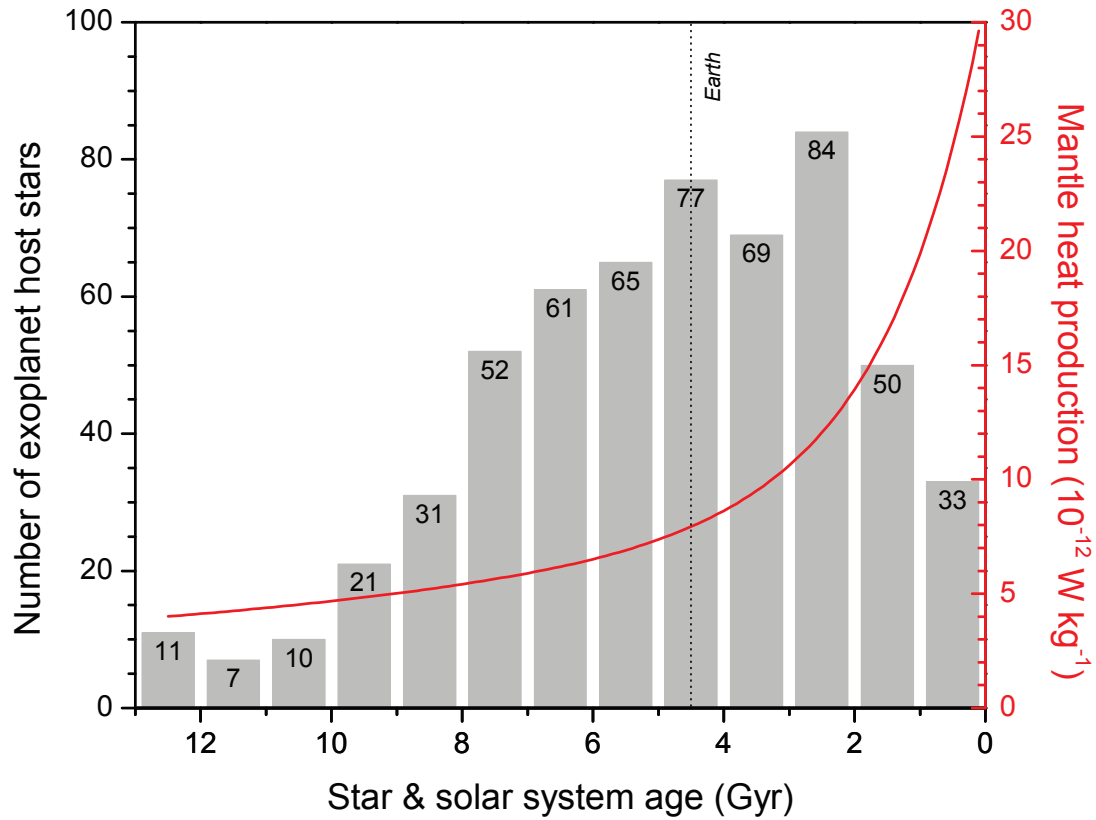
heat required for a rocky planet to support continued geological activity. In the absence of internal heat production, plate tectonics will end on Earth, though when and how this will occur are difficult to predict. Little work has been done on this topic: given that it is unknown how plate tectonics was initiated on Earth and how different Archean geodynamics was from the processes operating today, modeling its cessation is no easier. One attempt was made by (Sleep, 2007) to explore the different consequences of plate tectonics' demise on Earth, with the conclusion that the mantle could be too cool for convection in as soon as 0.9 Gyr. The delay between the terminus of plate tectonics and its cascading effects on global ecosystems are completely open questions, let alone the issue of how it might compare to similar scenarios on inhabited exoplanets. As such, while the oldest exoplanets may no longer be hot enough to support plate tectonics—should they have been capable of doing so in the first place, pinning down a rigorous date in the case of Earth remains unfeasible.

Better known than the lifetime of plate tectonics is the lifetime of stars. A G-type star like the Sun has a lifetime of approximately 10 Gyr, whereas dimmer M-type stars, which are also known to host exoplanets, have significantly longer lifetimes, up to hundreds of billions of years (Bertulani, 2013). Planets orbiting those stars will not be in imminent danger considering that the Galaxy is only 12.5 Gyr old (Dauphas, 2005), but the outlook for those around the oldest G-type stars is not particularly favorable. **Figure 4.1** shows the predicted heat production rates for cosmochemically Earth-like planets as a function of their age superimposed with the age distribution for dated stars with confirmed exoplanets, both gaseous and rocky, as of 2012.<sup>2</sup> The peak of ages around that of the Sun is a selection bias towards stars that were selected for focused observation due to their Sun-like qualities. The salient point from this figure is that in the search for Earth-like exoplanets, as previously

---

<sup>2</sup> Exoplanet population data from [en.wikipedia.org/wiki/List\\_of\\_exoplanetary\\_host\\_stars](http://en.wikipedia.org/wiki/List_of_exoplanetary_host_stars). Accessed Jan. 2014.

**Figure 4.1.** Number of exoplanet host stars as a function of their age superimposed with the predicted current heat production for cosmochemically Earth-like planets. The host stars include those that have either gaseous or rocky planets, and some stars are known to host multiple planets.



considered by other workers, stars of ages within a couple billion years in age from that of the Sun are most promising for their abilities to host life (e.g., Lineweaver et al., 2004). Rocky planets in these solar systems might be old enough to be beyond the period of late accretion but young enough such that their internal heat product is still sufficient for geological activity that may be expressed in the form of plate tectonics. Thus, in support of popular opinion, I argue that future searches for exoplanets should focus on those stars.

### **4.3. Habitability case study: H<sub>2</sub>-oxidizing biomass on Europa**

Among all bodies of astrobiological interest in the solar system, Europa is considered among the most promising for supporting extraterrestrial life. There is a broad suite of observational evidence that indicates that Europa has a subsurface ocean, such as moment of inertia estimates, chaos regions with trapped iceberg-like features, lineaments, and unique impact morphologies (Pappalardo et al., 1999). Europa is differentiated with a subsurface ocean that is in contact with a rocky mantle encapsulating a metal core. Its potential for supporting life draws from the immense heating it receives due to tidal interactions with Jupiter, which may result in sufficient heat for sustaining hydrothermal systems. On Earth, those systems support diverse populations of species despite the acidic, anaerobic, scalding water spewing from the vents. Should Europa be hot enough to melt rock, then a similar environment could exist beneath its icy shell, warranting consideration of the biological metabolisms that it may support.



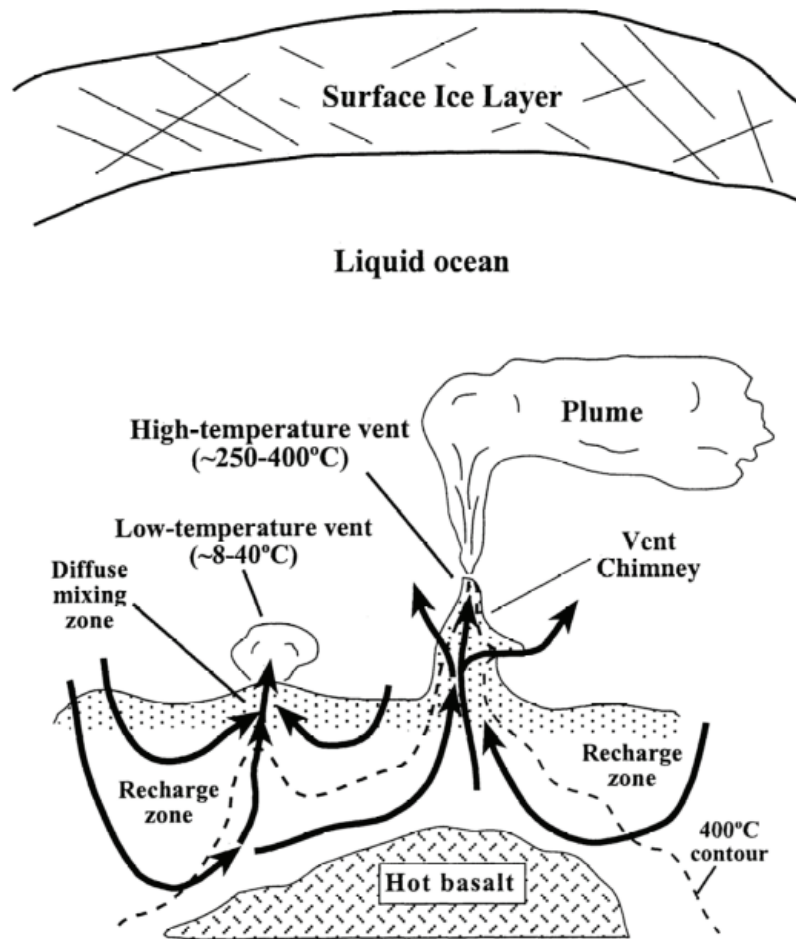
### 4.3.1. Introduction

That any life could exist at hydrothermal vents on Earth was a shocking discovery made during a 1977 ALVIN expedition to the Galapagos Rift. High populations of organisms such as mollusks and crabs were photographed around a vent even though no life had been observed elsewhere along the generally quiescent rift (Lonsdale, 1977). Since then, a plethora of organisms both macroscopic and microscopic have been discovered at other hydrothermal vents, and more continue to be found with further deep-sea expeditions. Beyond the ocean, extremophiles have been found in many other unexpected locations: the deep crust, glacial ice, hydrothermal springs, uranium deposits, and other seemingly inhospitable places (e.g., Rothschild and Mancinelli, 2001). The versatility of life on Earth lends credence to the idea that life—as we know it or otherwise—might be hardy enough to exist in a euroman ocean.

A key requirement for the existence of hydrothermal vents on any planetary body is a heat source. In Europa, internal heat derives from secular cooling, radiogenic heating, and tidal heating. Radiogenic and tidal heating alone may even produce enough heat to sustain hydrothermal vents on Europa (Lowell and DuBose, 2005). By extension, the plausibility of life in euroman hydrothermal vents—and the existence of the vents themselves—is dependent in large part on the moon's global heat flux. A hypothetical schematic of a possible euroman hydrothermal system is shown in **Figure 4.2**, taken from McCollom (1999).

Much more speculative than Europa's thermal state is the type of microbial metabolism that might be supported. Although methanogenesis, a type of microbial metabolism that results in the output of methane, has been suggested as a viable metabolism in a euroman hydrothermal system (McCollom, 1999),  $H_2$ -oxidizing microbes have not been considered in detail for their ability to be supported in a euroman ecosystem. Hydrogen

**Figure 4.2.** A hypothetical euroman hydrothermal vent system (McCollom, 1999).



oxidation extracts the most energy from hydrothermal vent fluid of all dissolved substrates, making it a particularly advantageous metabolism (McCollom, 2000). Here I present calculations for the maximum amount of H<sub>2</sub>-oxidizing biomass that may be supported by hydrothermal systems on Europa based on the range of radiogenic and tidal heating estimates.

#### 4.3.2. Heat Production

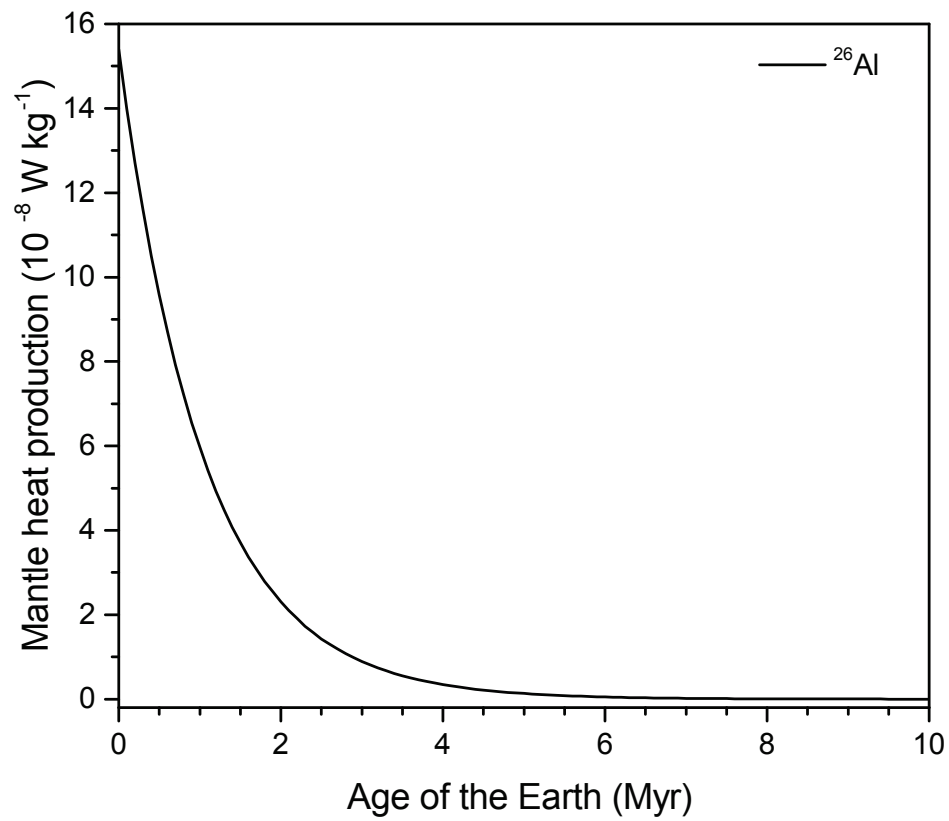
As outlined in §1.2.3.3, the long-lived radioactive isotopes <sup>40</sup>K, <sup>235</sup>U, <sup>238</sup>U, and <sup>232</sup>Th are a key source of heat for the long-term thermal evolution of rocky mantles in solid planetary bodies. Short-lived species such as <sup>26</sup>Al, which completely dominates short-lived heat production, are important for early solar system processes but do not operate today (§1.2.3.2). Past heat production can be back-calculated using the decay equation, isotope concentrations, and the heat production ( $H$ ) of the decaying isotope (Turcotte and Schubert, 2002):

$$H = C_0 H_0 \exp\left(\frac{t \ln 2}{\tau_{1/2}}\right) \quad (4.1)$$

where  $C_0$  is the isotope's initial abundance (kg isotope per kg mantle),  $H_0$  is the heat generated by the isotope (W kg<sup>-1</sup>),  $t$  is a time (Gyr), and  $\tau_{1/2}$  is the half-life (Gyr). As seen in **Figure 4.3**, short-lived <sup>26</sup>Al decayed very rapidly to extinction ~5 Myr into solar system history compared to the long-lived nuclides in **Figure 1.1**, which are still decaying and continue to provide heat to Earth's mantle.

Based on these calculations, the initial heat production at 4.6 Ga for the four long-lived nuclides in Earth's mantle was  $3.547 \times 10^{-13}$  W kg<sup>-1</sup>. Short-lived, heat-producing nuclides become extinct at approximately 5 Myr, a mere 0.1% of geologic time and likely irrelevant by the time that Jupiter's satellites completed accretion. Thus, short-lived species are unlikely to have an effect on Europa's thermal history, being more important for the planetesimals from

**Figure 4.3.** Heat production from the short-lived, heat-producing radionuclide  $^{26}\text{Al}$ , which dominates heat production in the early solar system.



which it formed. In the case of Europa, a present-day heat production for the european mantle will be assumed to be  $1.74 \times 10^{11}$  W, drawing from an estimate for Europa from Spohn and Schubert (2003).

Europa is locked in a Laplacian orbit with Ganymede and Io, two of its three brethren Galilean satellites. For each of Ganymede's revolutions around Jupiter, Europa orbits twice and Io four times. This resonance keeps Europa's orbit eccentric, which in turn affects its tidal deformation. Like our Earth-Moon system, Jupiter exerts more torque on Europa when it is at perijove and less when at apojoive. This tug-of-war from multiple sources generates shear friction in Europa's interior, which is expressed in the form of heat. Estimates of tidal heat production rates range between 10 to 100 mW m<sup>-2</sup> (e.g., Tobie et al., 2003).

Tidal heating is thought to generate more heat than the radiogenic sources, but the heat produced by decay is not insignificant, especially in relation to the lower bound for tidal heating. To find the combined heat production from radiogenic and tidal heating, the estimates are both converted to W and then summed. This results in a range for total heat production of 4.8 to  $33 \times 10^{11}$  W.

#### **4.3.3. Hydrothermal vents**

Hydrothermal vents are a visible manifestation of heat being released from Earth's interior. Roughly 75% of Earth's total heat loss occurs through the oceanic crust, and one third of that is released through hydrothermal systems at mid-ocean ridges, where oceanic plates are diverging and creating new crust (German and Lin, 2004). Seawater circulates through the hot, porous rock at these vents and is released at temperatures up to ~400°C, carrying with it a myriad of dissolved substances, including Fe, Mn, S, CH<sub>4</sub>, and H<sub>2</sub> (German and Lin, 2004). The hot water rises buoyantly and mixes with water above it in the water

column, as would be the case for Europa (**Figure 4.2**). If there is such an ocean in Europa, the tidal and radiogenic heat from its interior must be sufficient to maintain liquid water in such a frigid part of the solar system. Might some of the heat be released through hydrothermal vents at Europa's ocean-mantle interface? The answer to that question is currently unknown, but the plausibility of hydrothermal systems can be evaluated based on the above estimates for radiogenic and tidal heat.

In order to determine whether hydrothermal vents could exist on Europa, and later, the amount of H<sub>2</sub>-oxidizing biomass that could be supported by them, factors such as surface heat flux, thermal gradient, circulation, and mass flux must be taken into account. Best estimates drawn from knowledge about the Earth are used to fill in the gaps of knowledge for european parameters. The first step is to calculate the surface heat flux ( $q$ ) using the equation

$$q = \frac{H}{4\pi(R \cdot 10^5)^2} \quad (4.2)$$

where  $H = 4.8 - 33 \times 10^{12}$  W is the heat production and  $R = 1565$  km is Europa's radius (Lowell and DuBose, 2005). For the range of total heat production determined above,  $q = 0.018$  to  $0.12$  mW m<sup>-2</sup>.

In order to determine whether hydrothermal circulation is possible based on the heat production, the thermal gradient ( $\beta_E$ ), or change in temperature with depth, is calculated by

$$\beta_E = \frac{q}{\lambda} \quad (4.3)$$

where  $q$  is the surface flux calculated above and  $\lambda = 2.0$  W(mK)<sup>-1</sup> is the thermal conductivity of the silicate mantle, which is assumed to be comparable to Earth's upper mantle (Lowell and DuBose, 2005). This gives an upper and lower limit of  $9.0$  and  $60.5^\circ$  km<sup>-1</sup>. On Earth,

hydrothermal circulation occurs usually at 20 to 40° km<sup>-1</sup> (Lister, 1980). Assuming the same is true on Europa,  $4.8 \times 10^{12}$  W would not be sufficient to sustain hydrothermal systems, but  $33 \times 10^{12}$  W is. As such, further calculations will ignore this insufficient lower estimate in favor of the more optimistic upper bound.

On Earth, oceanic crust increases in age with distance from the mid-ocean ridge. Crust <60 Myr old is bare of significant amounts of sediment, but older crust that is closer to the continents will experience burial from sediment being shed from the eroding continents. The sediment then acts as a blanket that inhibits interior heat loss. Of the crust <60 Myr old, ~50% of its heat loss will be through hydrothermal circulation (Stein et al., 1995). Lacking the blanketing effects of eroding continents, Europa presumably has no or negligible sediment, so 50% of its total flux is assumed to come exclusively from hydrothermal circulation (Lowell and DuBose, 2005), which is  $1.6 \times 10^{12}$  W.

Europa, like Earth, could have both low- and high-temperature hydrothermal vents. High-temperature vents >350°C generate circulation and account for ~3 to 15% of the total terrestrial hydrothermal heat flux (Elderfield and Schultz, 1996). There is no circulation at low-temperature vents: the heat simply diffuses away. The upper bound of the European thermal gradient, 60.5° km<sup>-1</sup>, is significantly higher than that of Earth, which suggests that much more of Europa's heat flux would come from high-temperature vents. Lowell and DuBose (2005) estimate that this could be 10 to 50%; using these bounds results in a global high-temperature heat flux on Europa of 1.6 to  $8.2 \times 10^{11}$  W.

Finally, we must know the global hydrothermal mass flux, the mass of all water flowing through all hydrothermal systems on Europa. Mass flux ( $F$ ) is found using the equation

(4.4)

$$F = \frac{H_g}{\Delta T c_p}$$

where  $H_g = 8.2 \times 10^{11}$  W is the upper bound of the global high-temperature heat flux,  $\Delta T = 373$  K is the water temperature anomaly, and  $c_p = \sim 4$  kJ (kg K)<sup>-1</sup> is the heat capacity of water 0 to 100°C and 0 to 10 MPa (Lowell and DuBose, 2005). The water temperature anomaly is the difference in temperature between the vent fluid and surrounding cold waters. An assumption of 100°C is made based on comparable conditions on Earth (Lowell and DuBose, 2005) and the ability of thermotrophic organisms to use the high heat capacity of water as an energy source (Keenan et al., 1978). The resulting mass flux of water circulating at hydrothermal systems is  $5.5 \times 10^5$  kg s<sup>-1</sup>.

#### 4.3.4. H<sub>2</sub>-oxidation

Since the discovery of hydrothermal vents, each expedition to the deep ocean has both figuratively and literally shed light on the geological and biological processes that occur there. A 1986 expedition to the Endeavor segment of the Juan de Fuca ridge off the coast of the Northwestern United States resulted in the first observations of the compositional change of hydrothermal waters as they flowed away from the source vent (Kadko et al., 1990). Radon-222, a short-lived isotope with a half-life of 3.83 days, was used to date the water (Kadko et al., 1990). The team focused on the Mn, Fe, CH<sub>4</sub>, He, and H<sub>2</sub> in the fluids, predicting that their respective concentrations would change at different rates. Though the workers faced complications with data collection such as tides, currents, and changes in flow direction, it was clear that the H<sub>2</sub> concentration decayed the fastest, even relative to CH<sub>4</sub>, which was confirmed to be depleted by microbial activity. Hydrogen was observed to decay at twice the rate of



$^{222}\text{Rn}$ , and experiments showed that the  $\text{H}_2$  had a residence time of 10 hours, much more rapid than the sensitivity of the  $^{222}\text{Rn}$  chronometer (Kadko et al., 1990).

Though the authors briefly suggested the  $\text{H}_2$  may be undergoing rapid bacterial oxidation, the existence of such microbes at hydrothermal vents was not confirmed until 1995, when the first chemolithoautotrophic, thermophilic, hydrogen-gas-oxidizing bacterium was found at a vent along the Mid-Atlantic Ridge (Reysenbach et al., 2000). Hydrogen oxidation, termed the Knallgas (German for "bang-gas") reaction is:



This organism was important for two reasons: not only was it the first of its kind to be discovered, but of all dissolved substrates,  $\text{H}_2$  oxidation produces the greatest amount of energy (McCollom, 2000). The Knallgas reaction produces 4.4 mg dry weight biomass per kg vent fluid; for comparison, sulfur oxidation produces 17.0 mg dry wt biomass per kg vent fluid, but the sulfur exists as an unusable solid precipitate rather than a bioavailable dissolved substrate (McCollom, 2000). Although  $\text{H}_2$  may participate in methanogenesis and sulfate reduction, these processes are not nearly as productive (1.9 and 1.5 mg dry wt biomass per kg vent fluid, respectively; McCollom, 2000). Of course, this calculation assumes an Earth-like ocean, an unlikely composition in ocean-bearing icy bodies, but the relative productivity of the different metabolisms is instructive in evaluating their plausibility of operating in hypothetical extraterrestrial microbes.

Here,  $\text{H}_2$  oxidation is considered as a potential metabolism for organisms that could live in putative euroman hydrothermal vents due to its high energy production. To determine the biomass potential for  $\text{H}_2$ -oxidizing organisms, the production rate of 4.4 mg dry wt biomass per kg vent fluid calculated by McCollom (2000) is applied to the hydrothermal mass

flux calculated in §4.3.2 as well as those given for Earth and Europa by Lowell and DuBose (2005). The results are provided in **Table 4.1**. Due to the use of a more conservative value for the tidal heating contributions, the H<sub>2</sub>-oxidizing biomass estimates calculated here are roughly an order of magnitude smaller than the comparable value for the Lowell and DuBose (2005) results.

#### **4.3.5. Discussion and conclusions**

Based on heat production estimates and subsequent calculations for hydrothermal heat and mass fluxes, should the tidal heating contribution be on the high end of estimates, hydrothermal vent systems are possible on Europa. Tidal heating likely has a larger contribution than radiogenic heating. Due to its brief half-life, <sup>26</sup>Al did not have a significant effect on Europa's thermal evolution, and certainly would not provide heat to any life that might be there today. Tidal and radiogenic heating together may produce as much as  $1.6 \times 10^{12}$  W, causing a steep enough thermal gradient across Europa's interior that can sustain hydrothermal circulation.

Hydrogen oxidation is a chemolithoautotrophic metabolism worth considering for a european hydrothermal system because of its relative efficiency in producing biomass relative to other metabolisms, including methanogenesis and sulfate reduction. Assuming a production rate of 4.4 mg dry wt biomass per kg vent fluid (McCollom, 2000), up to  $2.4 \times 10^8$  kg yr<sup>-1</sup> may be generated through H<sub>2</sub> oxidation. Though this is significantly less than that produced on Earth, Europa is a much smaller body, and the results do not preclude the possibility of other microbial metabolisms.

**Table 4.1.** Comparison of biomass production calculated for Earth and Europa from Lowell and Dubose (2005), abbreviated to LD05, and Europa again based on this work. Biomass calculations draw from the biomass production rate for H<sub>2</sub> oxidation by McCollom (2000).

Parameter	Earth (LD05)	Europa (LD05)	Europa (this work)
Global hydrothermal heat flux	$10^{13}$ W	$5 \times 10^{12}$ W	$1.6 \times 10^{12}$ W
Global high-T heat flux	$3 \times 10^{11}$ W	$5\text{-}25 \times 10^{11}$ W	$1.6\text{-}8.2 \times 10^{11}$ W
Total hydrothermal mass flux	$2.5 \times 10^8$ kg s <sup>-1</sup>	$10^7$ kg s <sup>-1</sup>	$5.5 \times 10^5$ kg s <sup>-1</sup>
H <sub>2</sub> -oxidizing biomass	$3.5 \times 10^{10}$ kg yr <sup>-1</sup>	$1.4 \times 10^9$ kg yr <sup>-1</sup>	$2.4 \times 10^8$ kg yr <sup>-1</sup>

## 4.4. Earth-like exoplanets

Exoplanets that reside in the so-called "habitable zone" of a main-sequence star are of interest due to their potential for having liquid water on their surfaces provided a sufficiently thick atmosphere (Hart, 1979). This property, however, is only a simple first-order evaluation of habitability. Many other factors must be considered, and since evaluating a particular exoplanet's habitability is nearly impossible given the limited data available, it is statistically advantageous to look for planets that are most similar to Earth. Consequently, the focus of exoplanet searches, the *Kepler* mission in particular, has been on Earth-mass planets in their star's habitable zone.

One cannot definitively state one way or the other whether a particular planet is capable of harboring life, but we can surely argue that planets more similar to Earth than, for example, Mars have a higher likelihood of sustaining environments hospitable to life (as we know it). Using Mars as a point of comparison for a global-scale uninhabitable planet, an obvious difference between it and Earth is the present state of geological activity. In the case of our own planet, plate tectonics plays a fundamental role in the carbon cycle, helping to keep Earth's surface in thermodynamic disequilibrium (Des Marais, 1994; Parnell, 2004) and its global climate stable via the subduction of seafloor carbonates and subsequent release of CO<sub>2</sub> release back into the atmosphere through volcanism. Both criteria may be necessary for the long-term sustainability of biogeochemical cycles and the emergence of a substantial global-scale biosphere that could modulate atmospheric composition. Microbes can be found nearly everywhere on Earth there exists an exploitable redox gradient, and it is not unreasonable to assume that this would also be necessary for life beyond Earth (Benner et al., 2004). Indeed, as explained in §4.1, there are extremophiles on Earth thriving in

environments with a vast array of pH, temperature, pressure, radiation, salinity, desiccation, and chemistry. These environments range from deep-sea hydrothermal systems to salty evaporate basins to subglacial lakes, the diversity of which cannot be provided by a "dead" planet; while other bodies in our solar system such as Europa (e.g., Chyba and Phillips, 2002), Mars (e.g., McCollom, 2006), and Enceladus (e.g., Parkinson et al., 2008) have been hypothesized to be habitable, microbes on those bodies would have a much narrower selection of relatively hospitable environments from which to choose than that provided by our own geologically active planet. For its role in sustaining life on Earth, it is therefore reasonable to consider the plausibility of plate tectonics as one metric by which the habitable potential of an exoplanet can be judged.

## **4.5. Galactic habitability**

Also important to consider for extrasolar habitability is the concept of a galactic habitable zone (GHZ). The GHZ is defined as an annulus in the galactic disk that is sufficiently metal-rich to form rocky planets and has a relatively temperate environment for life to develop, particularly in the context of nearby supernovae rates (e.g., Gonzalez et al., 2001). The GHZ is not just defined in terms of space: time is a key factor as well, given that disk metallicity builds with time, and rocky planets will not form from ISM that is metal-poor. Indeed, a metallicity roughly half of that of the Sun may be required to produce a habitable rocky planet, and the region of the thin disk with sufficient metallicity migrates outwards as the Galaxy ages and becomes enriched in metals via nucleosynthesis (Gonzalez et al., 2001).

Lineweaver et al. (2004) evaluated the Milky Way's GHZ in the context of complex multicellular life and estimated that the GHZ annulus corresponds to 7 to 9 kpc from the

galactic center and has stars between 4 and 8 Ga old. Estimates of this annulus width are important given that the chemical and environmental limitations defined by the GHZ preclude Milky Way regions such as the halo, thick disk, outer thin disk, and bulge from having high abundances of hospitable Earth-like planets (Gonzalez et al., 2001). More recent work by Spitoni et al. (2014) involved adding radial gas flows and destructive supernovae processes to evaluations of the GHZ and confirmed the Lineweaver et al. (2004) GHZ annulus estimate of 7 to 9 kpc. Furthermore, they found that incorporating radial gas flows into the model enhanced the number of stars capable of hosting habitable planets by 38% relative to "classical" GHZ models such as those by Gonzalez et al. (2001) and Lineweaver et al. (2004). This is a promising result as technology for discovering exoplanets and evaluating their habitability continues to be developed. While the concept of a GHZ is important to take into account in any evaluation of habitability in the Galaxy, in our model (§2), we restricted the output to an annulus several hundred parsecs in width due to the compositional gradient effects of limited radial mixing. This is well within the 7 to 9 kpc annulus proposed by Lineweaver et al. (2004) and confirmed by Spitoni et al. (2014), and our model therefore applies to a region consistent with evaluations of our Galaxy's GHZ.

## 4.6. Concluding remarks

Incorporating the concepts of space- and time-limited habitability with those of the GHZ, observations of bodies in our solar system, and the nature of exoplanet observations today, we can introduce an integrated approach to evaluating exoplanets for their habitability. Searches for Earth-like exoplanets can be made more efficient by focusing on stars within a certain age range defined by life-limiting events in solar system and geological history.

Exoplanet host stars that are too young could still be experiencing post-primary accretion events; the Late Heavy Bombardment peaked ~700 Myr into solar system history, and the first evidence for life comes up in the geologic record at approximately the same time. Regardless of whether those two events are correlated, 1 Gyr might be considered a safe cutoff for a minimum time following planet formation for life to have taken hold.

A distinction must be made between life and detectable life, however. While life arise on Earth as early as 3.8 Ga, it would have not become observationally detectable from beyond Earth until the Great Oxygenation Event (GOE) at ca. 2.45 Ga (Papineau et al., 2007), which resulted in cyanobacteria populating the atmosphere with oxygen, an otherwise unstable species in planetary atmospheres due to its reactivity (Holland, 2002). No abiotic process is capable of making  $O_2$  on that scale. Consequently,  $O_2$  (in high concentration) is considered to be one of the telltale atmospheric biomarkers to detect extraterrestrial life (Sagan, 1994). Since it took approximately 2 Gyr after Earth's formation for the GOE to occur, I suggest that age as a cutoff for selecting target stars to search for rocky exoplanets with biomarkers. This automatically accounts for the winding down of large accretion events that might sterilize surfaces and subsurfaces of life. By that time, the planet's solar system should be stable. It should be noted, however, that it is only in the past few generations that sentient life on Earth became capable of space travel and communication.

From a life-limiting standpoint in the future, in the case of extraterrestrial life that depends on plate tectonics, the shutdown of plate tectonics might be a limiting factor in how long life thrives on the planet (§4.4). The work presented in §2 provides exoplanet geophysicists with one harder constraint for their models, which suffer from a general lack thereof. The task of determining the relative importance of age-dependent radiogenic heating

values to exoplanetary tectonic regimes is left to the geophysicists, but clearly, a young, warm planet is more likely to host plate tectonics than an ancient, cold one.

In consideration of detection capability, the most realistic future method of evaluating a particular planet's habitability is through measuring potential biomarker species in their atmosphere. A Europa-like planetary body with life beneath an ice shell or a Mars-like planet with small pockets of hospitable environs will not provide detectable biosignatures. For this reason, solid bodies with atmospheres—Earth-like planets—will feature the most detectable biomarkers. While the argument for focusing on searches for exoplanets around Sun-like stars is not a new one, the Late Veneer is proposed here for the first time as a hard constraint for when life could have arisen on Earth, and radiogenic heating has been shown to be a potential limiting factor for rocky exoplanets' ability to sustain Earth-like geodynamics and perhaps even Earth-like life.



## Chapter 5: Future directions

While the material presented in this dissertation encapsulates several years of work, as with all new knowledge, perhaps more questions have been created than answered. Here are possible areas for future research.

### 5.1. Radiogenic heating in exoplanets

The work presented in §2 regarding the radiogenic heating in exoplanets is only the first step in the topic of exoplanetary geochemistry, leaving much room for further expansion. The original motivation was to provide exoplanet geophysicists with a firmer constraint on one of the many parameters that go into their models. The clear next step in this work is for the results presented here to be input into those models, which primarily incorporate constant Earth-based or CI-based heat production rates. Simultaneously incorporating the timing of formation and age for a particular exoplanet around a star of a known age would add a significant degree of rigor to these models.

Expanding upon the model itself, its most challenging issue with which to grapple is to make the leap from a solar system's bulk composition to that of its planets. Here, I assumed that the ratio for a particular species between the concentration in CI chondrites and that in

Earth's mantle is the same as that for a "cosmochemically Earth-like planet." The intricacy of the model can be increased by incorporating another component into it: the distance of a particular planet from its star. Applying a simple condensation sequence based on the host star's spectral type allows for realistic predictions for a planet's bulk composition to be made based on the location at which it formed (assuming that the planet did not experience migration after formation).

An additional direction is to integrate the results over the Galaxy's star formation rate to determine a geochemical distribution that answers the question: what is a typical planet like for a particular age? Also interesting from the astronomical perspective is to compare the elemental ratios for radioactive species predicted here to those stars with a measured composition. This can provide an independent test of the veracity of the Clayton model, which is already coupled to astronomical observations such as the peak of the SFR and disk gas mass. Applications are also found in the field of nucleocosmochronology, which uses long-lived radionuclides to date stars. If the age of a particular star in the solar annulus is determined by an independent method (e.g., HR diagram position or astroseismology), then the output of the model presented here can be used to infer the chemistry of planets around it.

## 5.2. The Late Veneer

The largest impediment to continuing to search the ancient rock record for Late Veneer signatures is sample availability. Highly siderophile element analyses of Eoarchean komatiite-like rocks are limited by scarce sample availability from the oldest supracrustal belts. Furthermore, few HSE data exist for the time period between 2.9 and 3.1 Ga (**Figure 3.5**) due to a lack of komatiites of that age. We expect that future samples that fill in these

gaps will confirm the inferred trends described in this work, and that any that succeed in extending the komatiite record further back in time will show the continuation of a progressive decline in deep mantle HSE concentrations.

Archean komatiite collection is challenging in many of the oldest terranes, including the Nuvvuagittuq Supracrustal Belt and the Acasta Gneiss Complex, the localities from which samples described in this work derive. Touboul et al. (2014) have provided additional HSE analyses komatiites that broadened the suite of ultramafic rocks analyzed for their HSE as well as W abundances. Further exploration is warranted, and there are several promising locales, such as the Song Da zone in northwest Vietnam (Hanski et al., 2004). As shown by Willbold et al. (2011) and Touboul et al. (2012, 2014), W can also be used as a tracer for whether ultramafic rocks were contaminated by the Late Veneer, the material from which would have had a negative  $\epsilon^{182}\text{W}$  value (-200 ppm in the case of CI chondrites; Kleine et al., 2009). Measuring the samples discussed here for their W concentrations would operate as an independent test of the degree of Late Veneer contamination experienced by the rocks.

For the Late Veneer impact modeling, the work has only just begun. That described in §3.2 was a very preliminary endmember scenario that delivered mass perhaps twice that required for the HSE enrichment in the mantle. The results showed that a fast, oblique impact is the most effective method that would create the "hit-and-almost-run" scenario described by Bottke et al. (2010). Quantitative analysis of the results has not been performed yet due to challenges with the output normalization; future work is required to fix that problem. Given that this is an endmember scenario, and that the impactor(s) more likely delivered closer to 0.5% of Earth's current mass, further modeling is needed to determine the limit at which the challenge of keeping a differentiated impactor's core away from Earth's core is no longer an issue because the impactors are small enough to be undifferentiated. Since the geochemical

record is not capable of providing this information, and planetesimal dynamics do not narrow down the range of plausible sizes (Bottke et al., 2010), it is necessary to back out this information from impact modeling.

# References

- (OGLE), T.M.O. in A. (MOA) C.& T.O.G.L.E., Collaboration, 2011. Unbound or distant planetary mass population detected by gravitational microlensing. *Nature* 473, 349–352. doi:10.1038/nature10092
- Abramov, O., Kring, D.A., Mojzsis, S.J., 2013. The impact environment of the Hadean Earth. *Chemie der Erde - Geochemistry* 73, 227–248. doi:10.1016/j.chemer.2013.08.004
- Abramov, O., Mojzsis, S.J., 2009. Microbial habitability of the Hadean Earth during the late heavy bombardment. *Nature* 459, 419–422. doi:10.1038/nature08015
- Acuña, M.H., Connerney, J.E.P., Wasilewski, P., Lin, R.P., Anderson, K.A., Carlson, C.W., McFadden, J., Curtis, D.W., Mitchell, D., Reme, H., Mazelle, C., Sauvaud, J.A., D’Uston, C., Cros, A., Medale, J.L., Bauer, S.J., Cloutier, P., Mayhew, M., Winterhalter, D., Ness, N.F., 1998. Magnetic Field and Plasma Observations at Mars: Initial Results of the Mars Global Surveyor Mission. *Science* (80-. ). 279, 1676–1680. doi:10.1126/science.279.5357.1676
- Aitken, B.G., Echeverría, L.M., 1984. Petrology and geochemistry of komatiites and tholeiites from Gorgona Island, Colombia. *Contrib Miner. Pet.* 86, 94–105. doi:10.1007/BF00373714
- Amelin, Y., Krot, A.N., Hutcheon, I.D., Ulyanov, A.A., 2002. Lead isotopic ages of chondrules and calcium-aluminum-rich inclusions. *Science* (80-. ). 297, 1678–83. doi:10.1126/science.1073950
- Anbar, A.D., Zahnle, K.J., Arnold, G.L., Mojzsis, S.J., 2001. Extraterrestrial iridium, sediment accumulation and the habitability of the early Earth’s surface. *J. Geophys. Res.* 106, 3219. doi:10.1029/2000JE001272

- Anders, E., Grevesse, N., 1989. Abundances of the elements - Meteoritic and solar. *Geochim. Cosmochim. Acta* 53, 197–214.
- Arculus, R.J., Delano, J.W., 1981. Siderophile element abundances in the upper mantle: evidence for a sulfide signature and equilibrium with the core. *Geochim. Cosmochim. Acta* 45, 1331–1343. doi:10.1016/0016-7037(81)90226-X
- Arndt, N., 2003. Komatiites, kimberlites, and boninites. *J. Geophys. Res.* 108, 2293. doi:10.1029/2002JB002157
- Arndt, N., 2009. Earth science: Trickle-down geodynamics. *Nature* 460, 583–584. doi:10.1038/460583a
- Arndt, N., Leshner, C.M., Barnes, S.J., 2008. Komatiite. Cambridge University Press, Cambridge, UK.
- Arndt, N.T., Naldrett, A.J., Pyke, D.R., 1977. Komatiitic and Iron-rich Tholeiitic Lavas of Munro Township, Northeast Ontario. *J. Petrol.* 18, 319–369. doi:10.1093/petrology/18.2.319
- Asphaug, E., 2010. Similar-sized collisions and the diversity of planets. *Chemie der Erde - Geochemistry* 70, 199–219. doi:10.1016/j.chemer.2010.01.004
- Barclay, T., Rowe, J.F., Lissauer, J.J., Huber, D., Fressin, F., Howell, S.B., Bryson, S.T., Chaplin, W.J., Désert, J.-M., Lopez, E.D., Marcy, G.W., Mullally, F., Ragozzine, D., Torres, G., Adams, E.R., Agol, E., Barrado, D., Basu, S., Bedding, T.R., Buchhave, L.A., Charbonneau, D., Christiansen, J.L., Christensen-Dalsgaard, J., Ciardi, D., Cochran, W.D., Dupree, A.K., Elsworth, Y., Everett, M., Fischer, D.A., Ford, E.B., Fortney, J.J., Geary, J.C., Haas, M.R., Handberg, R., Hekker, S., Henze, C.E., Horch, E., Howard, A.W., Hunter, R.C., Isaacson, H., Jenkins, J.M., Karoff, C., Kawaler, S.D., Kjeldsen, H., Klaus, T.C., Latham, D.W., Li, J., Lillo-Box, J., Lund, M.N., Lundkvist, M., Metcalfe, T.S., Miglio, A., Morris, R.L., Quintana, E. V., Stello, D., Smith, J.C., Still, M., Thompson, S.E., 2013. A sub-Mercury-sized exoplanet. *Nature* 494, 452–454. doi:10.1038/nature11914
- Barnes, S., Naldrett, a, Gorton, M., 1985. The origin of the fractionation of platinum-group elements in terrestrial magmas. *Chem. Geol.* 53, 303–323. doi:10.1016/0009-2541(85)90076-2
- Baross, J.A., Benner, S., Cody, G.D., Copley, S.D., Pace, N.R., Scott, J.H., Shapiro, R., Sogin, M.L., Stein, J.L., 2007. *The Limits of Organic Life in Planetary Systems*. Washington, D.C.
- Benner, S.A., Ricardo, A., Carrigan, M.A., 2004. Is there a common chemical model for life in the universe? *Curr. Opin. Chem. Biol.* 8, 672–89. doi:10.1016/j.cbpa.2004.10.003

- Bennett, V.C., Brandon, A.D., Nutman, A.P., 2007. Coupled  $^{142}\text{Nd}$ - $^{143}\text{Nd}$  isotopic evidence for Hadean mantle dynamics. *Science* (80-. ). 318, 1907–1910. doi:10.1126/science.1145928
- Bensby, T., Feltzing, S., Lundström, I., 2004. A possible age-metallicity relation in the Galactic thick disk? *Astron. Astrophys.* 421, 969–976. doi:10.1051/0004-6361:20035957
- Bertulani, C., 2013. *Nuclei in the Cosmos*. World Scientific, Hackensack, NH.
- Blichert-Toft, J., Puchtel, I.S., 2010. Depleted mantle sources through time: Evidence from Lu–Hf and Sm–Nd isotope systematics of Archean komatiites. *Earth Planet. Sci. Lett.* 297, 598–606. doi:10.1016/j.epsl.2010.07.012
- Boeche, C., Chiappini, C., Minchev, I., Williams, M., Steinmetz, M., Sharma, S., Kordopatis, G., Bland-Hawthorn, J., Bienaymé, O., Gibson, B.K., Gilmore, G., Grebel, E.K., Helmi, A., Munari, U., Navarro, J.F., Parker, Q.A., Reid, W., Seabroke, G.M., Siebert, A., Siviero, A., Watson, F.G., Wyse, R.F.G., Zwitter, T., 2013. The relation between chemical abundances and kinematics of the Galactic disc with RAVE. *Astron. Astrophys.* 553, A19. doi:10.1051/0004-6361/201219607
- Boissier, S., Prantzos, N., 1999. Chemo-spectrophotometric evolution of spiral galaxies -- I. The model and the Milky Way. *Mon. Not. R. Astron. Soc.* 307, 857–876. doi:10.1046/j.1365-8711.1999.02699.x
- Bond, J.C., Lauretta, D.S., O'Brien, D.P., 2010. Making the Earth: Combining dynamics and chemistry in the Solar System. *Icarus* 205, 321–337. doi:10.1016/j.icarus.2009.07.037
- Bottke, W., 2002. Debiased Orbital and Absolute Magnitude Distribution of the Near-Earth Objects. *Icarus* 156, 399–433. doi:10.1006/icar.2001.6788
- Bottke, W.F., Levison, H.F., Nesvorný, D., Dones, L., 2007. Can planetesimals left over from terrestrial planet formation produce the lunar Late Heavy Bombardment? *Icarus* 190, 203–223. doi:10.1016/j.icarus.2007.02.010
- Bottke, W.F., Walker, R.J., Day, J.M.D., Nesvorný, D., Elkins-Tanton, L., 2010. Stochastic late accretion to Earth, the Moon, and Mars. *Science* (80-. ). 330, 1527–1530. doi:10.1126/science.1196874
- Bouvier, A., Wadhwa, M., 2010. The age of the Solar System redefined by the oldest Pb–Pb age of a meteoritic inclusion. *Nat. Geosci.* 3, 637–641. doi:10.1038/ngeo941
- Boyet, M., Blichert-Toft, J., Rosing, M., Storey, M., Télouk, P., Albarède, F., 2003.  $^{142}\text{Nd}$  evidence for early Earth differentiation. *Earth Planet. Sci. Lett.* 214, 427–442. doi:10.1016/S0012-821X(03)00423-0

- Brandon, A.D., Puchtel, I.S., Walker, R.J., Day, J.M.D., Irving, A.J., Taylor, L.A., 2012. Evolution of the martian mantle inferred from the  $^{187}\text{Re}$ – $^{187}\text{Os}$  isotope and highly siderophile element abundance systematics of shergottite meteorites. *Geochim. Cosmochim. Acta* 76, 206–235. doi:10.1016/j.gca.2011.09.047
- Bromm, V., Larson, R.B., 2004. The First Stars. *Annu. Rev. Astron. Astrophys.* 42, 79–118. doi:10.1146/annurev.astro.42.053102.134034
- Burbidge, E., Burbidge, G., Fowler, W., Hoyle, F., 1957. Synthesis of the Elements in Stars. *Rev. Mod. Phys.* 29, 547–650. doi:10.1103/RevModPhys.29.547
- Canup, R., 2008. Lunar-forming collisions with pre-impact rotation. *Icarus* 196, 518–538. doi:10.1016/j.icarus.2008.03.011
- Canup, R.M., 2004. Simulations of a late lunar-forming impact. *Int. J. Sol. Syst. Stud.* 168, 433–456. doi:10.1016/j.icarus.2003.09.028
- Canup, R.M., Asphaug, E., 2001. Origin of the Moon in a giant impact near the end of the Earth's formation. *Nature* 412, 708–712.
- Carlson, R.W., Boyet, M., 2009. Short-lived radionuclides as monitors of early crust–mantle differentiation on the terrestrial planets. *Earth Planet. Sci. Lett.* 279, 147–156. doi:10.1016/j.epsl.2009.01.017
- Caro, G., 2011. Early Silicate Earth Differentiation. *Annu. Rev. Earth Planet. Sci.* 39, 31–58. doi:10.1146/annurev-earth-040610-133400
- Caro, G., Bourdon, B., Birck, J.-L., Moorbath, S., 2006a. High-precision  $^{142}\text{Nd}/^{144}\text{Nd}$  measurements in terrestrial rocks: Constraints on the early differentiation of the Earth's mantle. *Geochim. Cosmochim. Acta* 70, 164–191. doi:10.1016/j.gca.2005.08.015
- Caro, G., Bourdon, B., Birck, J.-L., Moorbath, S., 2006b. High-precision  $^{142}\text{Nd}/^{144}\text{Nd}$  measurements in terrestrial rocks: Constraints on the early differentiation of the Earth's mantle. *Geochim. Cosmochim. Acta* 70, 164–191. doi:10.1016/j.gca.2005.08.015
- Carroll, B.W., Ostlie, D.A., 2007. *An Introduction to Modern Astrophysics*. Pearson Addison-Wesley, San Francisco.
- Carry, B., Vernazza, P., Dumas, C., Merline, W.J., Mousis, O., Rousselot, P., Jehin, E., Manfroid, J., Fulchignoni, M., Zucconi, J.-M., 2012. The remarkable surface homogeneity of the Dawn mission target (1) Ceres. *Icarus* 217, 20–26. doi:10.1016/j.icarus.2011.10.015
- Castillo-Rogez, J.C., McCord, T.B., 2010. Ceres' evolution and present state constrained by shape data. *Icarus* 205, 443–459. doi:10.1016/j.icarus.2009.04.008



- Cates, N.L., Mojzsis, S.J., 2006. Chemical and isotopic evidence for widespread Eoarchean metasedimentary enclaves in southern West Greenland. *Geochim. Cosmochim. Acta* 70, 4229–4257. doi:10.1016/j.gca.2006.05.014
- Cates, N.L., Mojzsis, S.J., 2007. Pre-3750 Ma supracrustal rocks from the Nuvvuagittuq supracrustal belt, northern Québec. *Earth Planet. Sci. Lett.* 255, 9–21. doi:10.1016/j.epsl.2006.11.034
- Cates, N.L., Ziegler, K., Schmitt, A.K., Mojzsis, S.J., 2013. Reduced, reused and recycled: Detrital zircons define a maximum age for the Eoarchean (ca. 3750–3780Ma) Nuvvuagittuq Supracrustal Belt, Québec (Canada). *Earth Planet. Sci. Lett.* 362, 283–293. doi:10.1016/j.epsl.2012.11.054
- Cayrel, R., Hill, V., Beers, T.C., Barbuy, B., Spite, M., Spite, F., Plez, B., Andersen, J., Bonifacio, P., François, P., Molaro, P., Nordström, B., Primas, F., 2001. Measurement of stellar age from uranium decay. *Nature* 409, 691–692. doi:10.1038/35055507
- Chambers, J.E., 2004. Planetary accretion in the inner Solar System. *Earth Planet. Sci. Lett.* 223, 241–252. doi:10.1016/j.epsl.2004.04.031
- Charbonneau, D., Berta, Z.K., Irwin, J., Burke, C.J., Nutzman, P., Buchhave, L.A., Lovis, C., Bonfils, X., Latham, D.W., Udry, S., Murray-Clay, R.A., Holman, M.J., Falco, E.E., Winn, J.N., Queloz, D., Pepe, F., Mayor, M., Delfosse, X., Forveille, T., 2009. A super-Earth transiting a nearby low-mass star. *Nature* 462, 891–4. doi:10.1038/nature08679
- Chiappini, C., Matteucci, F., Gratton, R., 1997. The Chemical Evolution of the Galaxy: The Two-Infall Model. *Astrophys. J.* 477, 765–780. doi:10.1086/303726
- Chou, C.-L., 1978. Fractionation of Siderophile Elements in the Earth's Upper Mantle, in: *Proc. Lunar. Planet. Sci. Conf.* 9th.
- Chyba, C., Phillips, C., 2002. Europa as an abode for life. *Orig. Life Evol. Biosph.* 6, 3–16.
- Clayton, D.D., 1975. Extinct radioactivities - Trapped residuals of presolar grains. *Astrophys. J.* 199, 765–769. doi:10.1086/153750
- Clayton, D.D., 1985. Galactic Chemical Evolution and Nucleocosmochronology: A Standard Model, in: Arnett, W.D., Truran, J.W. (Eds.), *Nucleosynthesis : Challenges and New Developments*. University of Chicago Press, Chicago, p. 65.
- Clayton, D.D., 1988. Nuclear cosmochronology within analytic models of the chemical evolution of the solar neighbourhood. *Mon. Not. R. Astron. Soc.* 234, 1–36.
- Clayton, D.D., 2003. *Handbook of Isotopes in the Cosmos*. Cambridge University Press, Cambridge.

- Clifford, S.M., Lasue, J., Heggy, E., Boisson, J., McGovern, P., Max, M.D., 2010. Depth of the Martian cryosphere : Revised estimates and implications for the existence and detection of subpermafrost groundwater. *J. Geophys. Res.* 115, E07001. doi:10.1029/2009JE003462
- Coltice, N., Schmalzl, J., 2006. Mixing times in the mantle of the early Earth derived from 2-D and 3-D numerical simulations of convection. *Geophys. Res. Lett.* 33, L23304. doi:10.1029/2006GL027707
- Copi, C., Schramm, D., Turner, M., 1995. Big-bang nucleosynthesis and the baryon density of the universe. *Science* (80-. ). 267, 192–199. doi:10.1126/science.7809624
- Cowan, J.J., Sneden, C., 2006. Heavy element synthesis in the oldest stars and the early Universe. *Nature* 440, 1151–1156. doi:10.1038/nature04807
- Cowan, J.J., Sneden, C., Burles, S., Ivans, I.I., Beers, T.C., Truran, J.W., Lawler, J.E., Primas, F., Fuller, G.M., Pfeiffer, B., Kratz, K., 2002. The chemical composition and age of the metal-poor halo star BD +17°3248. *Astrophys. J.* 572, 861–879.
- Cowan, J.J., Thielemann, F.K., Truran, J.W., 1991. Radioactive Dating of the Elements. *Annu. Rev. Astron. Astrophys.* 29, 447–497. doi:10.1146/annurev.aa.29.090191.002311
- Ćuk, M., Stewart, S.T., 2012. Making the Moon from a fast-spinning Earth: a giant impact followed by resonant despinning. *Science* 338, 1047–52. doi:10.1126/science.1225542
- Cuzzi, J.N., Hogan, R.C., Shariff, K., 2008. Toward Planetesimals: Dense Chondrule Clumps in the Protoplanetary Nebula. *Astrophys. J.* 687, 1432–1447. doi:10.1086/591239
- Dahl, T.W., Stevenson, D.J., 2010. Turbulent mixing of metal and silicate during planet accretion — And interpretation of the Hf-W chronometer. *Earth Planet. Sci. Lett.* 295, 177–186. doi:10.1016/j.epsl.2010.03.038
- Dale, C.W., Burton, K.W., Greenwood, R.C., Gannoun, A., Wade, J., Wood, B.J., Pearson, D.G., 2012. Late accretion on the earliest planetesimals revealed by the highly siderophile elements. *Science* (80-. ). 336, 72–75. doi:10.1126/science.1214967
- Dauphas, N., 2005. The U/Th production ratio and the age of the Milky Way from meteorites and Galactic halo stars. *Nature* 435, 1203–5. doi:10.1038/nature03645
- Dauphas, N., Cates, N.L., Mojzsis, S.J., Busigny, V., 2007. Identification of chemical sedimentary protoliths using iron isotopes in the >3750 Ma Nuvvuagittuq supracrustal belt, Canada. *Earth Planet. Sci. Lett.* 254, 358–376. doi:10.1016/j.epsl.2006.11.042
- Day, J.M.D., 2013. Hotspot volcanism and highly siderophile elements. *Chem. Geol.* 341, 50–74. doi:10.1016/j.chemgeo.2012.12.010

- Day, J.M.D., Pearson, D.G., Taylor, L.A., 2007. Highly siderophile element constraints on accretion and differentiation of the Earth-Moon system. *Science* (80-. ). 315, 217–219. doi:10.1126/science.1133355
- Day, J.M.D., Walker, R.J., James, O.B., Puchtel, I.S., 2010. Osmium isotope and highly siderophile element systematics of the lunar crust. *Earth Planet. Sci. Lett.* 289, 595–605. doi:10.1016/j.epsl.2009.12.001
- Day, J.M.D., Walker, R.J., Qin, L., Rumble III, D., 2012. Late accretion as a natural consequence of planetary growth. *Nat. Geosci.* 5, 614–617. doi:10.1038/ngeo1527
- De Avillez, M.A., Mac Low, M., 2002. Mixing Timescales in a Supernova-driven Interstellar Medium. *Astrophys. J.* 581, 1047–1060. doi:10.1086/344256
- Debaille, V., Neill, C.O., Brandon, A.D., Haenecour, P., Yin, Q., Mattielli, N., Treiman, A.H., 2013. Stagnant-lid tectonics in early Earth revealed by in late Archean rocks Nd variations.
- Dehant, V., Lammer, H., Kulikov, Y.N., Grießmeier, J.-M., Breuer, D., Verhoeven, O., Karatekin, Ö., Hoolst, T., Korablev, O., Lognonné, P., 2007. Planetary Magnetic Dynamo Effect on Atmospheric Protection of Early Earth and Mars. *Space Sci. Rev.*, Space Sciences Series of ISSI 129, 279–300. doi:10.1007/s11214-007-9163-9
- Des Marais, D.J., 1994. Tectonic control of the crustal organic carbon reservoir during the Precambrian. *Chem. Geol.* 114, 303–314. doi:10.1016/0009-2541(94)90060-4
- Dhuime, B., Hawkesworth, C.J., Cawood, P.A., Storey, C.D., 2012. A change in the geodynamics of continental growth 3 billion years ago. *Science* (80-. ). 335, 1334–1336. doi:10.1126/science.1216066
- Dodson-Robinson, S.E., Willacy, K., Bodenheimer, P., Turner, N.J., Beichman, C.A., 2009. Ice lines, planetesimal composition and solid surface density in the solar nebula. *Icarus* 200, 672–693. doi:10.1016/j.icarus.2008.11.023
- Drake, M.J., 2000. Accretion and primary differentiation of the Earth: a personal journey. *Geochim. Cosmochim. Acta* 64, 2363–2369. doi:10.1016/S0016-7037(00)00372-0
- Drake, M.J., Richter, K., 2002. Determining the composition of the Earth. *Nature* 416, 39–44.
- Elderfield, H., Schultz, A., 1996. Mid-Ocean Ridge Hydrothermal Fluxes and the Chemical Composition of the Ocean. *Annu. Rev. Earth Planet. Sci.* 24, 191–224. doi:10.1146/annurev.earth.24.1.191
- Elkins-Tanton, L.T., 2008. Linked magma ocean solidification and atmospheric growth for Earth and Mars. *Earth Planet. Sci. Lett.* 271, 181–191. doi:10.1016/j.epsl.2008.03.062

- Elkins-Tanton, L.T., Burgess, S., Yin, Q.-Z., 2011. The lunar magma ocean: Reconciling the solidification process with lunar petrology and geochronology. *Earth Planet. Sci. Lett.* 304, 326–336. doi:10.1016/j.epsl.2011.02.004
- Fassett, C.I., Head, J.W., Kadish, S.J., Mazarico, E., Neumann, G.A., Smith, D.E., Zuber, M.T., 2012. Lunar impact basins: Stratigraphy, sequence and ages from superposed impact crater populations measured from Lunar Orbiter Laser Altimeter (LOLA) data. *J. Geophys. Res. Planets* 117, E00H06. doi:10.1029/2011JE003951
- Finkelstein, S.L., Papovich, C., Dickinson, M., Song, M., Tilvi, V., Koekemoer, A.M., Finkelstein, K.D., Mobasher, B., Ferguson, H.C., Giavalisco, M., Reddy, N., Ashby, M.L.N., Dekel, A., Fazio, G.G., Fontana, A., Grogan, N.A., Huang, J.-S., Kocevski, D., Rafelski, M., Weiner, B.J., Willner, S.P., 2013. A galaxy rapidly forming stars 700 million years after the Big Bang at redshift 7.51. *Nature* 502, 524–527. doi:10.1038/nature12657
- Fitoussi, C., Bourdon, B., 2012. Silicon isotope evidence against an enstatite chondrite Earth. *Science* (80-. ). 335, 1477–1480. doi:10.1126/science.1219509
- Foley, B.J., Bercovici, D., Landuyt, W., 2012. The conditions for plate tectonics on super-Earths: Inferences from convection models with damage. *Earth Planet. Sci. Lett.* 331–332, 281–290. doi:10.1016/j.epsl.2012.03.028
- Fortney, J.J., Marley, M.S., Barnes, J.W., 2007. Planetary radii across five orders of magnitude in mass and stellar insolation: Application to transits. *Astrophys. J.* 1661–1672.
- Frebel, A., Christlieb, N., Norris, J.E., Thom, C., Beers, T.C., Rhee, J., 2007. Discovery of HE 1523-0901, a Strongly r -Process-enhanced Metal-poor Star with Detected Uranium. *Astrophys. J.* 660, L117–L120. doi:10.1086/518122
- Fütterer, O., Angelov, A., Liesegang, H., Gottschalk, G., Schleper, C., Schepers, B., Dock, C., Antranikian, G., Liebl, W., 2004. Genome sequence of *Picrophilus torridus* and its implications for life around pH 0. *Proc. Natl. Acad. Sci. U. S. A.* 101, 9091–9096. doi:10.1073/pnas.0401356101
- German, C.R., Lin, J., 2004. The Thermal Structure of the Oceanic Crust, Ridge-Spreading and Hydrothermal Circulation: How Well Do We Understand Their Inter-Connections?, in: German, C.R., Lin, J., Parsons, L. (Eds.), *Mid-Ocean Ridges: Hydrothermal Interactions Between the Lithosphere and Oceans*. American Geophysical Union, Washington, D.C.
- Goldschmidt, V.M., 1954. *Geochemistry*. Clarendon Press, Oxford.
- Gomes, R., Levison, H.F., Tsiganis, K., Morbidelli, a, 2005. Origin of the cataclysmic Late Heavy Bombardment period of the terrestrial planets. *Nature* 435, 466–469. doi:10.1038/nature03676

- Gonzalez, G., Brownlee, D., Ward, P., 2001. The Galactic Habitable Zone: Galactic Chemical Evolution. *Icarus* 152, 185–200. doi:10.1006/icar.2001.6617
- Green, D.H., 1975. Genesis of Archean Peridotitic Magmas and Constraints on Archean Geothermal Gradients and Tectonics. *Geology* 3, 15–18. doi:10.1130/0091-7613(1975)3<15:GOAPMA>2.0.CO;2
- Greenberg, R., Wacker, J.F., Hartmann, W.K., Chapman, C.R., 1978. Planetesimals to planets: Numerical simulation of collisional evolution. *Icarus* 35, 1–26. doi:10.1016/0019-1035(78)90057-X
- Hanski, E., Walker, R.J., Huhma, H., Polyakov, G. V., Balykin, P.A., Hoa, T.T., Phuong, N.T., 2004. Origin of the Permian-Triassic komatiites, northwestern Vietnam. *Contrib. to Mineral. Petrol.* 147, 453–469. doi:10.1007/s00410-004-0567-1
- Harrison, T.M., 2009. The Hadean Crust: Evidence from >4 Ga Zircons. *Annu. Rev. Earth Planet. Sci.* 37, 479–505. doi:10.1146/annurev.earth.031208.100151
- Hart, M.H., 1979. Habitable zones about main sequence stars. *Icarus* 37, 351–357. doi:10.1016/0019-1035(79)90141-6
- Hartmann, W., Ryder, G., Dones, L., Grinspoon, D.H., 2000. The time-dependent intense bombardment of the primordial Earth/Moon system, in: Canup, R.M., Righter, K. (Eds.), *Origin of the Earth and Moon*. Tuscon, AZ, pp. 493–512.
- Hayashi, C., 1981. Structure of the Solar Nebula, Growth and Decay of Magnetic Fields and Effects of Magnetic and Turbulent Viscosities on the Nebula. *Prog. Theor. Phys. Suppl.* 70, 35–53. doi:10.1143/PTPS.70.35
- Herzberg, C., Condie, K., Korenaga, J., 2010. Thermal history of the Earth and its petrological expression. *Earth Planet. Sci. Lett.* 292, 79–88. doi:10.1016/j.epsl.2010.01.022
- Hill, V., Plez, B., Cayrel, R., Beers, T.C., Nordstrom, B., Andersen, J., Spite, M., Spite, F., Barbuy, B., Bonifacio, P., Depagne, E., Francois, P., Primas, F., 2002. First stars. I: The extreme r-element rich, iron-poor halo giant CS 31082-001 - Implications for the r-process site(s) and radioactive cosmochronology. *Astron. Astrophys.* 387, 560–579. doi:10.1051/0004-6361
- Hillebrandt, W., Niemeyer, J.C., 2000. Type Ia supernova explosion models. *Annu. Rev. Astron. Astrophys.* 38, 191–230. doi:10.1146/annurev.astro.38.1.191
- Hohenberg, C.M., Munk, M.N., Reynolds, J.H., 1967. Spallation and fissiogenic xenon and krypton from stepwise heating of the Pasamonte achondrite; The case for extinct plutonium 244 in meteorites; Relative ages of chondrites and achondrites. *J. Geophys. Res.* 72, 3139–3177. doi:10.1029/JZ072i012p03139

- Holland, H.D., 2002. Volcanic gases, black smokers, and the great oxidation event. *Geochim. Cosmochim. Acta* 66, 3811–3826. doi:10.1016/S0016-7037(02)00950-X
- Honda, S., Aoki, W., Kajino, T., Ando, H., Beers, T.C., Izumiura, H., Sadakane, K., Takada-hidai, M., 2004. Spectroscopic Studies of Extremely Metal-Poor Stars With the Subaru High Dispersion. *Astrophys. J.* 474–498.
- Horan, M., 2003. Highly siderophile elements in chondrites. *Chem. Geol.* 196, 27–42. doi:10.1016/S0009-2541(02)00405-9
- Hoyle, F., Fowler, W.A., 1960. Nucleosynthesis in Supernovae. *Astrophys. J.* 132, 565–590. doi:10.1086/146963
- Hsieh, H.H., Jewitt, D., 2006. A population of comets in the main asteroid belt. *Science* (80-. ). 312, 561–563. doi:10.1126/science.1125150
- Humayun, M., Nemchin, A., Zanda, B., Hewins, R.H., Grange, M., Kennedy, A., Lorand, J.-P., Göpel, C., Fieni, C., Pont, S., Deldicque, D., 2013. Origin and age of the earliest Martian crust from meteorite NWA 7533. *Nature* 503, 513–516. doi:10.1038/nature12764
- Huss, G.R., Meyer, B.S., Srinivasan, G., Goswami, J.N., Sahijpal, S., 2009. Stellar sources of the short-lived radionuclides in the early solar system. *Geochim. Cosmochim. Acta* 73, 4922–4945. doi:10.1016/j.gca.2009.01.039
- Hussmann, H., Sohl, F., Spohn, T., 2006. Subsurface oceans and deep interiors of medium-sized outer planet satellites and large trans-neptunian objects. *Icarus* 185, 258–273. doi:10.1016/j.icarus.2006.06.005
- Iess, L., Stevenson, D.J., Parisi, M., Hemingway, D., Jacobson, R.A., Lunine, J.I., Nimmo, F., Armstrong, J.W., Asmar, S.W., Ducci, M., Tortora, P., 2014. The gravity field and interior structure of Enceladus. *Science* (80-. ). 344, 78–80. doi:10.1126/science.1250551
- Jacobsen, S.B., 1988. Isotopic and chemical constraints on mantle-crust evolution. *Geochim. Cosmochim. Acta* 52, 1341–1350. doi:10.1016/0016-7037(88)90205-0
- Jacobson, S.A., Morbidelli, A., Raymond, S.N., O'Brien, D.P., Walsh, K.J., Rubie, D.C., 2014. Highly siderophile elements in Earth's mantle as a clock for the Moon-forming impact. *Nature* 508, 84–87. doi:10.1038/nature13172
- Johansen, A., Oishi, J.S., Mac Low, M.-M., Klahr, H., Henning, T., Youdin, A., 2007. Rapid planetesimal formation in turbulent circumstellar disks. *Nature* 448, 1022–1025. doi:10.1038/nature06086
- Johnson, J.A., Bolte, M., 2001. The Ages for Metal-poor Stars. *Astrophys. J.* 20, 888–902.

- Johnson, J.A., Winn, J.N., Albrecht, S., Howard, A.W., Marcy, G.W., Gazak, J.Z., 2009. A Third Exoplanetary System with Misaligned Orbital and Stellar Spin Axes. *Publ. Astron. Soc. Pacific* 121, 1104–1111. doi:10.1086/644604
- Jones, E.G., Lineweaver, C.H., 2010. To what extent does terrestrial life “follow the water”? *Astrobiology* 10, 349–361. doi:10.1089/ast.2009.0428
- Jones, J.H., Neal, C.R., Ely, J.C., 2003. Signatures of the highly siderophile elements in the SNC meteorites and Mars: a review and petrologic synthesis. *Chem. Geol.* 196, 5–25. doi:10.1016/S0009-2541(02)00404-7
- Jonsell, K., Barklem, P.S., Gustafsson, B., Christlieb, N., Hill, V., Beers, T.C., Holmberg, J., 2006. The Hamburg / ESO R-process enhanced star survey (HERES) III. HE 0338-3945 and the formation of the r + s stars. *Astron. Astrophys.* 670, 651–670. doi:10.1051/0004-6361
- Kadko, D.C., Rosenberg, N.D., Lupton, J.E., Collier, R.W., Lilley, M.D., 1990. Chemical reaction rates and entrainment within the Endeavour Ridge hydrothermal plume. *Earth Planet. Sci. Lett.* 99, 315–335. doi:10.1016/0012-821X(90)90137-M
- Kaltenegger, L., Selsis, F., Fridlund, M., Lammer, H., Beichman, C., Danchi, W., Eiroa, C., Henning, T., Herbst, T., Le, A., Lunine, J., Paresce, F., Penny, A., Quirrenbach, A., Ro, H., Schneider, J., Stam, D., Tinetti, G., White, G.J., 2010. Deciphering Spectral Fingerprints of Habitable Exoplanets 10.
- Kargel, J.S., Lewis, J.S., 1993. The Composition and Early Evolution of Earth. *Icarus* 105, 1–25. doi:10.1006/icar.1993.1108
- Keenan, J.H., Keyes, F.G., Hill, P.G., Moore, J.G., 1978. *Steam Tables: Thermodynamic Properties of Water Including Vapor, Liquid, and Solid Phases*. Krieger Publishing Company, Malabar, Florida.
- Kelemen, P., Kikawa, E., Miller, D., 2004. *Proceedings of the Ocean Drilling Program, Initial Reports*. Volume 209. [online].
- Kimura, K., Lewis, R.S., Anders, E., 1974. Distribution of gold and rhenium between nickel-iron and silicate melts: implications for the abundance of siderophile elements on the Earth and Moon. *Geochim. Cosmochim. Acta* 38, 683–701.
- Kite, E.S., Manga, M., Gaidos, E., 2009. Geodynamics and Rate of Volcanism on Massive Earth-like Planets. *Astrophys. J.* 700, 1732–1749. doi:10.1088/0004-637X/700/2/1732
- Kleine, T., Touboul, M., Bourdon, B., Nimmo, F., Mezger, K., Palme, H., Jacobsen, S.B., Yin, Q.-Z., Halliday, A.N., 2009. Hf–W chronology of the accretion and early evolution of asteroids and terrestrial planets. *Geochim. Cosmochim. Acta* 73, 5150–5188. doi:10.1016/j.gca.2008.11.047



- Kokubo, E., Ida, S., 1998. Oligarchic Growth of Protoplanets. *Icarus* 131, 171–178.  
doi:10.1006/icar.1997.5840
- Krane, K., 1987. *Introductory Nuclear Physics*. John Wiley & Sons, Inc.
- Krasinsky, G., 2002. Hidden Mass in the Asteroid Belt. *Icarus* 158, 98–105.  
doi:10.1006/icar.2002.6837
- Küppers, M., O'Rourke, L., Bockelée-Morvan, D., Zakharov, V., Lee, S., von Allmen, P., Carry, B., Teyssier, D., Marston, A., Müller, T., Crovisier, J., Barucci, M.A., Moreno, R., 2014. Localized sources of water vapour on the dwarf planet (1) Ceres. *Nature* 505, 525–527. doi:10.1038/nature12918
- Lenardic, A., Cooper, C.M., Moresi, L., 2011. A note on continents and the Earth's Urey ratio. *Phys. Earth Planet. Inter.* 188, 127–130. doi:10.1016/j.pepi.2011.06.008
- Leshner, C.M., Keays, R.R., 2002. Komatiite-associated Ni-Cu-PGE deposits, in: Cabri, L.J. (Ed.), *The Geology, Geochemistry, Mineralogy and Mineral Beneficiation of the Platinum-Group Elements, Special Volume, Vol. 54*. Canadian Institute of Mining, Metallurgy, and Petroleum, pp. 579 – 617.
- Levison, H.F., Duncan, M.J., Brasser, R., Kaufmann, D.E., 2010. Capture of the Sun's Oort cloud from stars in its birth cluster. *Science* (80-. ). 329, 187–190.  
doi:10.1126/science.1187535
- Li, J., Zhao, G., 2009. Radioactive Ages of Metal-Poor Halo Stars. *Chinese J. Astron. Astrophys.* 75, 75–87.
- Lineweaver, C.H., Fenner, Y., Gibson, B.K., 2004. The galactic habitable zone and the age distribution of complex life in the Milky Way. *Science* (80-. ). 303, 59–62.  
doi:10.1126/science.1092322
- Lister, C.R.B., 1980. Heat Flow and Hydrothermal Circulation. *Annu. Rev. Earth Planet. Sci.* 8, 95–117. doi:10.1146/annurev.ea.08.050180.000523
- Lodders, K., 2003. Solar System Abundances and Condensation Temperatures of the Elements. *Astrophys. J.* 591, 1220–1247. doi:10.1086/375492
- Lonsdale, P., 1977. Deep-tow observations at the mounds abyssal hydrothermal field, Galapagos Rift. *Earth Planet. Sci. Lett.* 36, 92–110. doi:10.1016/0012-821X(77)90191-1
- Lorand, J.-P., Luguet, A., Alard, O., 2008. Platinum-Group Elements: A New Set of Key Tracers for the Earth's Interior. *Elements* 4, 247–252.  
doi:10.2113/GSELEMENTS.4.4.247



- Lowell, R.P., DuBose, M., 2005. Hydrothermal systems on Europa. *Geophys. Res. Lett.* 32, L05202. doi:10.1029/2005GL022375
- Ludwig, H.-G., Caffau, E., Steffen, M., Bonifacio, P., Sbordone, L., 2010. Accuracy of spectroscopy-based radioactive dating of stars. *Astron. Astrophys.* 509, A84. doi:10.1051/0004-6361/200810780
- Madau, P., Pozzetti, L., Dickinson, M., 1998. The Star Formation History of Field Galaxies. *Astrophys. J.* 498, 106–116. doi:10.1086/305523
- Maher, K.A., Stevenson, D.J., 1988. Impact frustration of the origin of life. *Nature* 331, 612–614. doi:10.1038/331612a0
- Maier, W.D., Barnes, S.J., Campbell, I.H., Fiorentini, M.L., Peltonen, P., Barnes, S.-J., Smithies, R.H., 2009. Progressive mixing of meteoritic veneer into the early Earth's deep mantle. *Nature* 460, 620–623. doi:10.1038/nature08205
- Maier, W.D., Peltonen, P., McDonald, I., Barnes, S.J., Barnes, S.-J., Hatton, C., Viljoen, F., 2012. The concentration of platinum-group elements and gold in southern African and Karelian kimberlite-hosted mantle xenoliths: Implications for the noble metal content of the Earth's mantle. *Chem. Geol.* 302–303, 119–135. doi:10.1016/j.chemgeo.2011.06.014
- Mann, U., Frost, D.J., Rubie, D.C., Becker, H., Audétat, A., 2012. Partitioning of Ru, Rh, Pd, Re, Ir and Pt between liquid metal and silicate at high pressures and high temperatures - Implications for the origin of highly siderophile element concentrations in the Earth's mantle. *Geochim. Cosmochim. Acta* 84, 593–613. doi:10.1016/j.gca.2012.01.026
- Manning, C.E., Mojzsis, S.J., Harrison, T.M., 2006. Geology, Age and Origin of Supracrustal Rocks at Akilia, West Greenland. *Am. J. Sci.* 306, 303–366. doi:10.2475/05.2006.02
- Marchi, S., Bottke, W.F., Elkins-Tanton, L.T., Bierhaus, M., Wuennemann, K., Morbidelli, A., Kring, D.A., 2014. Widespread mixing and burial of Earth's Hadean crust by asteroid impacts. *Nature* 511, 578–582. doi:10.1038/nature13539
- Matteucci, F., 2003. *The Chemical Evolution of the Galaxy*. Kluwer Academic Publishers, Dordrecht, The Netherlands.
- Matteucci, F., Greggio, L., 1986. Relative roles of type I and II supernovae in the chemical enrichment of the interstellar gas. *Astron. Astrophys.* 154, 279–287.
- Mayor, M., Queloz, D., 1995. A Jupiter-mass companion to a solar-type star. *Nature* 378, 355–359. doi:10.1038/378355a0

- McCollom, T.M., 1999. Methanogenesis as a potential source of chemical energy for primary biomass production by autotrophic organisms in hydrothermal systems on Europa. *J. Geophys. Res.* 104, 30729–30742. doi:10.1029/1999JE001126
- McCollom, T.M., 2000. Geochemical constraints on primary productivity in submarine hydrothermal vent plumes. *Deep Sea Res. Part I Oceanogr. Res. Pap.* 47, 85–101.
- McCollom, T.M., 2006. The Habitability of Mars: Past and Present, in: Blondel, P., Mason, J.W. (Eds.), *Solar System Update*. Springer-Verlag, Berlin, pp. 159–175. doi:10.1007/3-540-37683-6\_6
- McCord, T.B., Castillo-Rogez, J., Rivkin, A., 2011. Ceres: Its Origin, Evolution and Structure and Dawn's Potential Contribution. *Space Sci. Rev.* 163, 63–76. doi:10.1007/s11214-010-9729-9
- McCord, T.B., Sotin, C., 2005. Ceres: Evolution and current state. *J. Geophys. Res. Planets* 110, 5009–5023. doi:10.1029/2004JE002244
- McDonough, W., Sun, S., 1995. The composition of the Earth. *Chem. Geol.* 254/1, 223–253.
- McGregor, V., Mason, B., 1977. Petrogenesis and geochemistry of metabasaltic and metasedimentary enclaves in the Amitsoq gneisses, West Greenland. *Am. Mineral.* 62, 887–904.
- McSween Jr., H., Ghosh, A., Grimm, R.E., Wilson, L., Young, E.D., 2002. Thermal Evolution Models of Asteroids, in: Bottke, W.F., Cellino, A., Paolicchi, P., Binzel, R.P. (Eds.), *Asteroids III*. University of Arizona Press, Tuscon, AZ, pp. 559–571.
- Meyer, B.S., Clayton, D.D., 2000. Short-Lived Radioactivities and the Birth of the Sun, in: Benz, W., Kallenbach, R., Lugmair, G.W. (Eds.), *From Dust to Terrestrial Planets*. Springer Netherlands, pp. 133–152. doi:10.1007/978-94-011-4146-8\_11
- Mihalas, D., Binney, J., 1981. *Galactic Astronomy: Structure and Kinematics*, 2nd ed. W.H. Freeman & Co., San Francisco.
- Milliken, R.E., Rivkin, A.S., 2009. Brucite and carbonate assemblages from altered olivine-rich materials on Ceres. *Nat. Geosci.* 2, 258–261. doi:10.1038/ngeo478
- Mojzsis, S.J., Arrhenius, G., McKeegan, K.D., Harrison, T.M., Nutman, A.P., Friend, C.R., 1996. Evidence for life on Earth before 3,800 million years ago. *Nature* 384, 55–59. doi:10.1038/384055a0
- Morbidelli, A., Marchi, S., Bottke, W.F., Kring, D.A., 2012. A sawtooth-like timeline for the first billion years of lunar bombardment. *Earth Planet. Sci. Lett.* 355–356, 144–151. doi:10.1016/j.epsl.2012.07.037

- Mostefaoui, S., Lugmair, G.W., Hoppe, P., 2005.  $^{60}\text{Fe}$ : A Heat Source for Planetary Differentiation from a Nearby Supernova Explosion. *Astrophys. J.* 625, 271–277. doi:10.1086/429555
- Mouri, H., Maier, W.D., Brandl, G., 2013. On the possible occurrence of komatiites in the Archean high-grade polymetamorphic central zone of the Limpopo Belt, South Africa. *South African J. Geol.* 116, 55–66. doi:10.2113/gssajg.116.1.55
- Nesvorný, D., Jenniskens, P., Levison, H.F., Bottke, W.F., Vokrouhlický, D., Gounelle, M., 2010. Cometary Origin of the Zodiacal Cloud and Carbonaceous Micrometeorites. Implications for Hot Debris Disks. *Astrophys. J.* 713, 816–836. doi:10.1088/0004-637X/713/2/816
- Neukum, G., Wilhelms, D.E., 1982. Ancient Lunar Impact Record, in: *Lunar and Planetary Science Conference XIII*. Houston, TX, pp. 590–591.
- Nisbet, E.G., Sleep, N.H., 2001. The habitat and nature of early life. *Nature* 409, 1083–91. doi:10.1038/35059210
- Nittler, L.R., Dauphas, N., 2006. Meteorites and the Chemical Evolution of the Milky Way, in: Lauretta, D.S., McSween Jr, H.Y. (Eds.), *Meteorites and the Early Solar System II*. University of Arizona Press, Tuscon, pp. 127–146.
- Noack, L., Breuer, D., n.d. Plate tectonics on rocky exoplanets: Influence of initial conditions and mantle rheology. *Planet. Space Sci.* doi:10.1016/j.pss.2013.06.020
- Norman, M.D., Nemchin, A.A., 2014. A 4.2 billion year old impact basin on the Moon: U–Pb dating of zirconolite and apatite in lunar melt rock 67955. *Earth Planet. Sci. Lett.* 388, 387–398. doi:10.1016/j.epsl.2013.11.040
- Nutman, A.P., McGregor, V.R., Friend, C.R.L., Bennett, V.C., Kinny, P.D., 1996. The Itsaq Gneiss Complex of southern West Greenland; the world's most extensive record of early crustal evolution (3900–3600 Ma). *Precambrian Res.* 78, 1–39. doi:10.1016/0301-9268(95)00066-6
- O'Neil, J., Francis, D., Carlson, R.W., 2011. Implications of the Nuvvuagittuq Greenstone Belt for the Formation of Earth's Early Crust. *J. Petrol.* 52, 985–1009. doi:10.1093/petrology/egr014
- O'Neil, J., Maurice, C., Stevenson, R., Larocque, J., Cloquet, C., David, J., Francis, D., 2007. The geology of the 3.8 Ga Nuvvuagittuq (Porpoise Cove) greenstone belt, northeastern Superior Province, Canada, in: Kranendonk, V.M.J., Smithies, R.H., Bennett, V. (Eds.), *Earth's Oldest Rocks*. Elsevier, Amsterdam, pp. 219–254.
- O'Neill, C., Debaille, V., Griffin, W., 2013. Deep earth recycling in the Hadean and constraints on surface tectonics. *Am. J. Sci.* 313, 912–932. doi:10.2475/09.2013.04

- O'Neill, C.J., 2012. Tectonothermal evolution of solid bodies: terrestrial planets, exoplanets and moons. *Aust. J. Earth Sci.* 59, 189–198. doi:10.1080/08120099.2012.644403
- Pace, N.R., 1997. A Molecular View of Microbial Diversity and the Biosphere. *Science* (80-.). 276, 734–740. doi:10.1126/science.276.5313.734
- Pagel, B.E.J., 1997. *Nucleosynthesis and Chemical Evolution of Galaxies*. Cambridge University Press, Cambridge.
- Pahlevan, K., Stevenson, D.J., 2007. Equilibration in the aftermath of the lunar-forming giant impact. *Earth Planet. Sci. Lett.* 262, 438–449. doi:10.1016/j.epsl.2007.07.055
- Palme, H., O'Neill, H.S.C., 2003. Cosmochemical Estimates of Mantle Composition, in: Carlson, R.W. (Ed.), *Treatise on Geochemistry, Volume 2: The Mantle and Core*. Elsevier, pp. 1–38.
- Papineau, D., Mojzsis, S.J., Schmitt, A.K., 2007. Multiple sulfur isotopes from Paleoproterozoic Huronian interglacial sediments and the rise of atmospheric oxygen. *Earth Planet. Sci. Lett.* 255, 188–212. doi:10.1016/j.epsl.2006.12.015
- Pappalardo, R.T., Belton, M.J.S., Breneman, H.H., Carr, M.H., Chapman, C.R., Collins, G.C., Denk, T., Fagents, S., Geissler, P.E., Giese, B., Greeley, R., Greenberg, R., Head, J.W., Helfenstein, P., Hoppa, G., Kadel, S.D., Klaasen, K.P., Klemaszewski, J.E., Magee, K., McEwen, A.S., Moore, J.M., Moore, W.B., Neukum, G., Phillips, C.B., Prockter, L.M., Schubert, G., Senske, D.A., Sullivan, R.J., Tufts, B.R., Turtle, E.P., Wagner, R., Williams, K.K., 1999. Does Europa have a subsurface ocean? Evaluation of the geological evidence. *J. Geophys. Res.* 104, 24015. doi:10.1029/1998JE000628
- Papuc, A.M., Davies, G.F., 2008. The internal activity and thermal evolution of Earth-like planets. *Icarus* 195, 447–458. doi:10.1016/j.icarus.2007.12.016
- Parkinson, C.D., Liang, M.-C., Yung, Y.L., Kirschvink, J.L., 2008. Habitability of Enceladus: Planetary Conditions for Life. *Orig. Life Evol. Biosph.*, *Bulletin of the American Astronomical Society* 38, 355–369. doi:10.1007/s11084-008-9135-4
- Parnell, J., 2004. Plate tectonics, surface mineralogy, and the early evolution of life. *Int. J. Astrobiol.* 3, 131–137. doi:10.1017/S1473550404002101
- Petit, J.-M., Chambers, J., Franklin, F., Nagasawa, M., 2002. Primordial excitation and depletion of the main belt, in: Bottke, W.F., Cellino, A., Paolicchi, P., Binzel, R. (Eds.), *Asteroids III*. University of Arizona Press, Tuscon, AZ, pp. 711–723.
- Plez, B., Hill, V., Cayrel, R., Spite, M., Barbuy, B., Beers, T.C., Bonifacio, P., Primas, F., Nordström, B., 2004. Lead abundance in the uranium star CS 31082-001. *Astron. Astrophys.* 12, 9–12. doi:10.1051/0004-6361

- Reeves, H., 1991. Nucleochronology revisited. *Astron. Astrophys.* 244, 294–297.
- Reid, M.J., 1993. The Distance to the Center of the Galaxy. *Annu. Rev. Astron. Astrophys.* 31, 345–372. doi:10.1146/annurev.aa.31.090193.002021
- Reysenbach, A.-L., Longnecker, K., Kirshtein, J., 2000. Novel Bacterial and Archaeal Lineages from an In Situ Growth Chamber Deployed at a Mid-Atlantic Ridge Hydrothermal Vent. *Appl. Environ. Microbiol.* 66, 3798–3806. doi:10.1128/AEM.66.9.3798-3806.2000
- Riches, A.J.V., Day, J.M.D., Walker, R.J., Simonetti, A., Liu, Y., Neal, C.R., Taylor, L. a., 2012. Rhenium–osmium isotope and highly-siderophile-element abundance systematics of angrite meteorites. *Earth Planet. Sci. Lett.* 353–354, 208–218. doi:10.1016/j.epsl.2012.08.006
- Richter, F.M., 1988. A Major Change in the Thermal State of the Earth at the Archean-Proterozoic Boundary: Consequences for the Nature and Preservation of Continental Lithosphere. *J. Petrol. Special Vo*, 39–52. doi:10.1093/petrology/Special\_Volume.1.39
- Righter, K., Drake, M.J., 1997. Metal-silicate equilibrium in a homogeneously accreting earth: new results for Re. *Earth Planet. Sci. Lett.* 146, 541–553.
- Ringwood, A.E., 1977. Composition of the core and implications for origin of Earth. *Geochem. J.* 11, 111–135.
- Rivkin, A.S., Volquardsen, E.L., Clark, B.E., 2006. The surface composition of Ceres: Discovery of carbonates and iron-rich clays. *Icarus* 185, 563–567. doi:10.1016/j.icarus.2006.08.022
- Rizo, H., Boyet, M., Blichert-Toft, J., O’Neil, J., Rosing, M.T., Paquette, J.-L., 2012. The elusive Hadean enriched reservoir revealed by  $^{142}\text{Nd}$  deficits in Isua Archaean rocks. *Nature* 491, 96–100. doi:10.1038/nature11565
- Robin-Popieul, C.C.M., Arndt, N.T., Chauvel, C., Byerly, G.R., Sobolev, A. V., Wilson, A., 2012. A New Model for Barberton Komatiites: Deep Critical Melting with High Melt Retention. *J. Petrol.* 53, 2191–2229. doi:10.1093/petrology/egs042
- Roth, A.S.G., Bourdon, B., Mojzsis, S.J., Rudge, J.F., Guitreau, M., Blichert-Toft, J., 2014. Combined  $^{147}\text{Sm}$ -  $^{143}\text{Nd}$  constraints on the longevity and residence time of early terrestrial crust. *Geochemistry, Geophys. Geosystems* 15, 2329–2345. doi:10.1002/2014GC005313
- Roth, A.S.G., Bourdon, B., Mojzsis, S.J., Touboul, M., Sprung, P., Guitreau, M., Blichert-Toft, J., 2013. Inherited  $^{142}\text{Nd}$  anomalies in Eoarchean protoliths. *Earth Planet. Sci. Lett.* 361, 50–57. doi:10.1016/j.epsl.2012.11.023

- Rothschild, L.J., Mancinelli, R.L., 2001. Life in Extreme Environments. *Nature* 409, 1092–1101.
- Rudge, J.F., Kleine, T., Bourdon, B., 2010a. Broad bounds on Earth's accretion and core formation constrained by geochemical models. *Nat. Geosci.* 3, 439–443. doi:10.1038/ngeo872
- Rudge, J.F., Kleine, T., Bourdon, B., 2010b. Broad bounds on Earth's accretion and core formation constrained by geochemical models. *Nat. Geosci.* 3, 439–443. doi:10.1038/ngeo872
- Ryder, G., Koeberl, C., Mojzsis, S.J., 2000. Heavy bombardment of the Earth at ~ 3.85 Ga: The search for petrographic and geochemical evidence. *Orig. Earth Moon* 475–492.
- Sagan, C., 1994. *Pale Blue Dot*. Ballantine Books, New York.
- Savard, D., Barnes, S.-J., Meisel, T., 2010. Comparison between Nickel-Sulfur Fire Assay Te Co-precipitation and Isotope Dilution with High-Pressure Asher Acid Digestion for the Determination of Platinum-Group Elements, Rhenium and Gold. *Geostand. Geoanalytical Res.* 34, 281–291. doi:10.1111/j.1751-908X.2010.00090.x
- Schatz, H., Toenjes, R., Pfeiffer, B., Beers, T.C., Cowan, J.J., Hill, V., Kratz, K., 2002. Thorium and Uranium Chronometers Applied to CS 31082-001. *Astrophys. J.* 579, 626–638. doi:10.1086/342939
- Schopf, J.W., 1993. Microfossils of the Early Archean Apex Chert: New Evidence of the Antiquity of Life. *Science* (80-. ). 260, 640–646. doi:10.1126/science.260.5108.640
- Schulze-Makuch, D., Grinspoon, D.H., Abbas, O., Irwin, L.N., Bullock, M. a, 2004. A sulfur-based survival strategy for putative phototrophic life in the venusian atmosphere. *Astrobiology* 4, 11–18.
- Schwamb, M.E., Brown, M.E., Rabinowitz, D.L., Ragozzine, D., 2010. Properties of the distant Kuiper Belt: Results from the Palomar Distant Solar System Survey. *Astrophys. J.* 720, 1691–1707. doi:10.1088/0004-637X/720/2/1691
- Seager, S., Bains, W., Hu, R., 2013. A biomass-based model to estimate the plausibility of exoplanet biosignature gases. *Astrophys. J.* 775, 104–132. doi:10.1088/0004-637X/775/2/104
- Seager, S., Kuchner, M., Hier-Majumder, C.A., Militzer, B., 2007. Mass-Radius Relationships for Solid Exoplanets. *Astrophys. J.* 669, 1279–1297. doi:10.1086/521346
- Shu, F.H., Shang, H., Glassgold, A.E., Lee, T., 1997. X-rays and Fluctuating X-Winds from Protostars. *Science* (80-. ). 277, 1475–1479. doi:10.1126/science.277.5331.1475

- Sleep, N.H., 2007. Plate Tectonics through Time. *Treatise Geophys.* 9, 145–169.  
doi:10.1016/B978-044452748-6.00143-7
- Sleep, N.H., Zahnle, K., Neuhoﬀ, P.S., 2001. Initiation of clement surface conditions on the earliest Earth. *Proc. Natl. Acad. Sci.* 98, 3666–3672.
- Smith, D.E., Zuber, M.T., Phillips, R.J., Solomon, S.C., Hauck, S. a, Lemoine, F.G., Mazarico, E., Neumann, G. a, Peale, S.J., Margot, J.-L., Johnson, C.L., Torrence, M.H., Perry, M.E., Rowlands, D.D., Goossens, S., Head, J.W., Taylor, A.H., 2012. Gravity field and internal structure of Mercury from MESSENGER. *Science* (80-. ). 336, 214–7. doi:10.1126/science.1218809
- Snedden, C., Cowan, J.J., Gallino, R., 2008. Neutron-Capture Elements in the Early Galaxy. *Annu. Rev. Astron. Astrophys.* 46, 241–288.  
doi:10.1146/annurev.astro.46.060407.145207
- Snedden, C., Cowan, J.J., Ivans, I.I., Fuller, G.M., Burles, S., Beers, T.C., Lawler, J.E., 2000. Evidence of Multiple r-Process Sites in the Early Galaxy: New Observations of CS 22892–052. *Astrophys. J.* 533, L139–L142. doi:10.1086/312631
- Snedden, C., Cowan, J.J., Lawler, J.E., Ivans, I.I., Burles, S., Beers, T.C., Primas, F., Hill, V., Truran, J.W., Fuller, G.M., Pfeiffer, B., Kratz, K., 2003. The Extremely Metal-poor, Neutron Capture-rich Star CS 22892–052: A Comprehensive Abundance Analysis. *Astrophys. J.* 591, 936–953. doi:10.1086/375491
- Snedden, C., McWilliam, A., Preston, G.W., Cowan, J.J., Burris, D.L., Armosky, B.J., 1996. The Ultra-Metal-poor, Neutron-Capture-rich Giant Star CS 22892–052. *Astrophys. J.* 467, 819. doi:10.1086/177656
- Snow, J.E., Schmidt, G., 1998. Constraints on Earth accretion deduced from noble metals in the oceanic mantle. *Nature* 391, 166–169.
- Soderblom, D.R., 2010. The Ages of Stars. *Annu. Rev. Astron. Astrophys.* 48, 581–629.  
doi:10.1146/annurev-astro-081309-130806
- Sotin, C., Tobie, G., 2004. Internal structure and dynamics of the large icy satellites. *Comptes Rendus Phys.* 5, 769–780. doi:10.1016/j.crhy.2004.08.001
- Spergel, D.N., Verde, L., Peiris, H. V., Komatsu, E., Nolta, M.R., Bennett, C.L., Halpern, M., Hinshaw, G., Jarosik, N., Kogut, A., Limon, M., Meyer, S.S., Page, L., Tucker, G.S., Weiland, J.L., Wollack, E., Wright, E.L., 2003. First-Year Wilkinson Microwave Anisotropy Probe (WMAP) Observations: Determination of Cosmological Parameters. *Astrophys. J. Suppl. Ser.* 148, 175–194. doi:10.1086/377226



- Spitoni, E., Matteucci, F., Sozzetti, A., 2014. The galactic habitable zone of the Milky Way and M31 from chemical evolution models with gas radial flows. *Mon. Not. R. Astron. Soc.* 440, 2588–2598. doi:10.1093/mnras/stu484
- Spohn, T., Schubert, G., 2003. Oceans in the icy Galilean satellites of Jupiter? *Icarus* 161, 456–467. doi:10.1016/S0019-1035(02)00048-9
- Stein, C., Stein, S., Pelayo, A., 1995. Heat Flow and Hydrothermal Circulation, in: Humphris, S., Zierenberg, R., Mullineaux, L., Thomson, R. (Eds.), *Seafloor Hydrothermal Systems: Physical, Chemical, Biological, and Geological Interactions*. American Geophysical Union, Washington, D.C. doi:10.1029/GM091p0425
- Stevenson, D., 1981. Models of the Earth's Core. *Science* (80-. ). 214, 611–618.
- Stevenson, D., 1999. Life-sustaining planets in interstellar space? *Nature* 400, 32.
- Stevenson, D.J., 1982. Formation of the giant planets. *Planet. Space Sci.* 30, 755–764. doi:10.1016/0032-0633(82)90108-8
- Stewart, S.T., Leinhardt, Z.M., 2012. Collisions between gravity-dominated bodies. II. The diversity of impact outcomes during the end stage of planet formation. *Astrophys. J.* 751, 32–49. doi:10.1088/0004-637X/751/1/32
- Suda, T., Katsuta, Y., Yamada, S., Suwa, T., Ishizuka, C., Komiya, Y., Sorai, K., Aikawa, M., Fujimoto, M.Y., 2008. *Stellar Abundances for the Galactic Archeology (SAGA) Database --- Compilation of the Characteristics of Known Extremely Metal-Poor Stars*. Publ. Astron. Soc. Japan.
- Tera, F., Papanastassiou, D., Wasserburg, G., 1974. Isotopic evidence for a terminal lunar cataclysm. *Earth Planet. Sci. Lett.* 22, 1–21.
- Tinsley, B.M., 1979. Stellar lifetimes and abundance ratios in chemical evolution. *Astrophys. J.* 229, 1046–1056. doi:10.1086/157039
- Tobie, G., Choblet, G., Sotin, C., 2003. Tidally heated convection: Constraints on Europa's ice shell thickness. *J. Geophys. Res.* 108, 5124. doi:10.1029/2003JE002099
- Touboul, M., Puchtel, I.S., Walker, R.J., 2012. 182W evidence for long-term preservation of early mantle differentiation products. *Science* (80-. ). 335, 1065–1069. doi:10.1126/science.1216351
- Turcotte, D.L., Schubert, G., 2002. *Geodynamics*, 2nd ed. Cambridge University Press, New York.



- Urey, H.C., 1956. The Cosmic Abundances of Potassium, Uranium, and Thorium and the Heat Balances of the Earth, the Moon, and Mars. *Proc. Natl. Acad. Sci.* 42, 889–891. doi:10.1073/pnas.42.12.889
- Valencia, D., O’Connell, R.J., 2009. Convection scaling and subduction on Earth and super-Earths. *Earth Planet. Sci. Lett.* 286, 492–502. doi:10.1016/j.epsl.2009.07.015
- Valencia, D., O’Connell, R.J., Sasselov, D., 2006. Internal structure of massive terrestrial planets. *Icarus* 181, 545–554. doi:10.1016/j.icarus.2005.11.021
- Valencia, D., O’Connell, R.J., Sasselov, D.D., 2007. Inevitability of Plate Tectonics on Super-Earths. *Astrophys. J.* 670, L45–L48. doi:10.1086/524012
- Valley, J.W., Cavosie, A.J., Ushikubo, T., Reinhard, D.A., Lawrence, D.F., Larson, D.J., Clifton, P.H., Kelly, T.F., Wilde, S.A., Moser, D.E., Spicuzza, M.J., 2014. Hadean age for a post-magma-ocean zircon confirmed by atom-probe tomography. *Nat. Geosci.* 7, 219–223. doi:10.1038/ngeo2075
- Vance, S., Harnmeijer, J., Kimura, J., Hussmann, H., Demartin, B., Brown, J.M., 2007. Hydrothermal systems in small ocean planets. *Astrobiology* 7, 987–1005. doi:10.1089/ast.2007.0075
- Viljoen, M., Viljoen, R., 1969. The geology and geochemistry of the lower ultramafic unit of the Onverwacht Group and a proposed new class of igneous rocks. *Geol. Soc. S. Africa Spec. Publ.* 2, 55–86.
- Walker, R., Horan, M., Morgan, J., Becker, H., Grossman, J., Rubin, A., 2002. Comparative  $^{187}\text{Re}$ - $^{187}\text{Os}$  systematics of chondrites: Implications regarding early solar system processes. *Geochim. Cosmochim. Acta* 66, 4187–4201. doi:10.1016/S0016-7037(02)01003-7
- Walker, R.J., 2009. Highly siderophile elements in the Earth, Moon and Mars: Update and implications for planetary accretion and differentiation. *Chemie der Erde - Geochemistry* 69, 101–125. doi:10.1016/j.chemer.2008.10.001
- Walker, R.J., Horan, M.F., Shearer, C.K., Papike, J.J., 2004. Low abundances of highly siderophile elements in the lunar mantle: evidence for prolonged late accretion. *Earth Planet. Sci. Lett.* 224, 399–413. doi:10.1016/j.epsl.2004.05.036
- Wasserburg, G.J., Busso, M., Gallino, R., 1996. Abundances of Actinides and Short-lived Nonactinides in the Interstellar Medium: Diverse Supernova Sources for the r-Processes. *Astrophys. J.* 466, L109–L113. doi:10.1086/310177
- Weber, R.C., Lin, P.-Y., Garnero, E.J., Williams, Q., Lognonné, P., 2011. Seismic detection of the lunar core. *Science* (80-. ). 331, 309–312. doi:10.1126/science.1199375

- Weidenschilling, S.J., 1977. Aerodynamics of solid bodies in the solar nebula. *Mon. Not. R. Astron. Soc.* 180, 57–70. doi:10.1093/mnras/180.2.57
- Westin, J., Sneden, C., Gustafsson, B., Cowan, J.J., 2000. The r-Process–enriched Low-Metallicity Giant HD 115444. *Astrophys. J.* 530, 783–799. doi:10.1086/308407
- Wiechert, U., Halliday, A.N., Lee, D.C., Snyder, G.A., Taylor, L.A., Rumble, D., 2001. Oxygen isotopes and the moon-forming giant impact. *Science* (80-. ). 294, 345–348. doi:10.1126/science.1063037
- Willbold, M., Elliott, T., Moorbath, S., 2011. The tungsten isotopic composition of the Earth’s mantle before the terminal bombardment. *Nature* 477, 195–198. doi:10.1038/nature10399
- Wood, B.J., Walter, M.J., Wade, J., 2006. Accretion of the Earth and segregation of its core. *Nature* 441, 825–833. doi:10.1038/nature04763
- Zhang, H.W., Gehren, T., Butler, K., Shi, J.R., Zhao, G., 2006. Potassium abundances in nearby metal-poor stars. *Astron. Astrophys.* 457, 645–650. doi:10.1051/0004-6361:20064909

# Appendix 1: Running the galactic chemical evolution calculations

We use Clayton's models for our Galactic chemical evolution (GCE) calculations. These models are analytic; however, it is difficult to compute the necessary gas consumption rate or yield parameters, and it becomes tedious to compute the species mass fractions at multiple time steps. For this reason, we use *wn\_simple\_gce*, a library of open-source, freely-available C computer codes, to perform all our GCE calculations.

## 1) Install *wn\_simple\_gce*

*wn\_simple\_gce* uses the same libraries as NucNet Tools and NucNet Projects. Thus, to install the necessary libraries, follow the instructions at

<http://sourceforge.net/p/nucnet-projects/wiki/libraries/>

appropriate for your operating system. Once those libraries are installed, follow the Download and Compile tutorials for *wn\_simple\_gce* at

[http://www.webnucleo.org/home/modules/wn\\_simple\\_gce/0.5/html/about\\_this\\_module/tutorials/](http://www.webnucleo.org/home/modules/wn_simple_gce/0.5/html/about_this_module/tutorials/)

Once *wn\_simple\_gce* is installed, try several of the examples to ensure that everything is working correctly.

## 2) Compute the gas consumption rate

The first step in applying *wn\_simple\_gce* to the chemical evolution of the Galaxy is to find the gas consumption rate. The gas fraction (fraction of the mass that is in gas) in the solar neighborhood today is ~0.15-0.25 (e.g., Boissier and Prantzos, 1999). We choose 0.2. We

also choose Clayton parameters  $k$  and  $\Delta$  to be 1 and 0.1, respectively. To compute the gas consumption rate  $\omega$ , in the *examples* directory in our *wn\_simple\_gce* distribution, we type

```
./get_omega_from_gas_fraction 1 0.1 0.2 12.5
```

This returns

For a  $k = 1$  and a  $\Delta = 0.1$ :

To get a gas fraction of 0.2 at  $T = 12.5$  Gyr, you need an  $\omega = 0.211170/\text{Gyr}$ .

This tells us that to get a gas fraction of 0.2 at time 12.5 Gyr after disk formation with  $k = 1$  and  $\Delta = 0.1$ , we need an  $\omega = 0.21117 \text{ Gyr}^{-1}$ . Note that I can always get a usage statement for a *wn\_simple\_gce* example code by typing the executable without arguments. For example, I can type

```
./get_omega_from_gas_fraction
```

This returns

Usage: *./get\_omega\_from\_gas\_fraction* k Delta omega fraction time

$k$  = Clayton infall parameter  $k$

Delta = Clayton infall parameter Delta

Fraction = Gas Fraction

time = time in Gyr at which to determine omega from gas fraction

which tells me I need to supply *get\_omega\_from\_gas\_fraction* with the parameters  $k$ , Delta, gas fraction, and time at which to compute omega. Usage statements for other *wn\_simple\_gce* examples can be obtained similarly.

### 3) Compute the Galactic masses

With the proper  $\omega$ , we now compute the masses of the components of the Galaxy (our Fig. 2). The mass of stars and gas in Galactic disk is estimated to be ~60 billion solar masses (Prantzos and Silk, 1998). We type

```
./gce_masses 1.34e9 1 0.1 0.21117
```

The 1.34e9 is the initial disk mass at the beginning of our calculation (needed since Clayton's standard infall parameterization is in terms of this number). The value 1.34e9 was found by repeated trial to give a Galactic disk total mass of 400 billion solar masses at 12.5 Gyr. Notice that the gas mass is 20% of the total mass at 12.5 Gyr, as expected from our choice of  $\omega$ .

#### 4) Compute Primary Species Yields

We may now compute the yields of primary species. It is first necessary to know the abundances of these species. A convenient way to find these values is with the Solar Abundances Tool at:

[http://www.webnucleo.org/home/online\\_tools/solar\\_abundances/0.3/](http://www.webnucleo.org/home/online_tools/solar_abundances/0.3/)

We use abundances from Anders and Grevesse (1989) at the beginning of the Solar System; thus, we launch the Solar Abundances Tool. In the Tool window, we launch the Upload Tool and choose *Anders\_0.xml* (download this from the supplementary material). We click ok. Once that file is correctly uploaded, click Sort Data and then View Abundance Table. The table will list Solar System abundances and their mass fractions. For example, we see that the mass fraction of  $^{16}\text{O}$  is 9.591826E-03.

We now compute the yield of  $^{16}\text{O}$ . To do this, we type

```
./compute_species_yield_parameters 1 0.1 0.21117 o16 0. 8.0 9.591826E-03
```

which returns

To get a mass fraction 0.00959183 at 8 Gyr:

$$\alpha(\text{o16}) = 0.0112171$$

Our yield of  $^{16}\text{O}$  is thus  $\alpha=0.0112171$ . Notice that we input to *compute\_species\_yield\_parameters* k, Delta, omega, species name, decay rate (per Gyr), time at which species should have the input mass fraction (for us, 8.0 Gyr, since that is the beginning of the Solar System in our model), and the desired mass fraction. We repeat this process for all key primary species (and use the non-zero decay rate for radioactive species).

#### 5) Compute Primary Yield

To compute the yield of secondary species, we need to compute the yield of all the primary species. This, in fact, is the sum of all the alpha's for "metals" ( $^{12}\text{C}$  and heavier mass species). Alternatively, we may compute this as for a particular primary species. The mass fraction of all "metals" is about 0.02, and, since the abundance of primary species dominates those of secondary species, this is, to good approximation, the mass fraction of all primary species; thus, we can run

```
./compute_species_yield_parameters 1 0.1 0.21117 primary 0. 8.0 0.02
```

This gives a total primary yield of  $\alpha=0.0233889$ .

#### 6) Compute Secondary Species Yield

With the total primary species yield available, we may compute the secondary species yield. This is relevant, for example, for  $^{40}\text{K}$ . If we assume  $^{40}\text{K}$  is purely secondary, we may type (all on one line)

```
./compute_species_yield_parameters 1 0.1 0.21117 k40 0.555 8. 5.544642E-09 0.0233889 0.
```

The 0.555 is the  $^{40}\text{K}$  decay rate (per Gyr), 5.544642e-9 is the mass fraction of  $^{40}\text{K}$  at 8.0 Gyr, 0.0233889 is the primary yield, and 0. is the primary part of the  $^{40}\text{K}$  yield. The result is  $\alpha(^{40}\text{K}) = 0$  and  $\beta(^{40}\text{K}) = 1.11595\text{e-}06$ .

We expect  $^{40}\text{K}$  to be partially primary and partially secondary. We infer from data in Woosley and Weaver (1995) that a realistic guess for  $\alpha(^{40}\text{K}) = 5.5\text{e-}9$ ; thus, we type (all on one line)

```
./compute_species_yield_parameters 1 0.1 0.21117 k40 0.555 8. 5.544642E-09 0.0233889 5.5e-9
```

This yields  $\alpha(^{40}\text{K}) = 5.5\text{e-}9$  and  $\beta(^{40}\text{K}) = 7.87411\text{e-}07$ .

In the case  $^{40}\text{K}$  is purely primary, we compute the yield as we did the other primary species (section 4).

## **7) Compute Species Mass Fractions in the Gas vs. Time.**

With yields now available, we can compute the species mass fraction in the gas as a function of time. To do so, we type, for example, all on one line

```
./compute_species_mass_fraction 1 0.1 0.21117 0.0233889 o16 0. 0.0112171 > o16.txt
```

The > redirects the output to the file o16.txt. Plot column 2 vs. column 1 to get the  $^{16}\text{O}$  mass fraction vs. time. For a secondary species, add the beta part. For example, for  $^{40}\text{K}$ , we type (all on one line)

```
./compute_species_mass_fraction 1 0.1 0.21117 0.0233889 k40 0.555 5.5e-9 7.87411e-7 > k40_primary_and_secondary.txt
```

or

```
./compute_species_mass_fraction 1 0.1 0.21117 0.0233889 k40 0.555 0. 1.11595e-06 > k40_secondary_only.txt
```

## **8) Compute the $^{56}\text{Fe}$ Mass Fraction**

Because of the contributions of Type Ia supernovae, the yield function for  $^{56}\text{Fe}$  is more complicated than for a normal primary species. We take the  $^{56}\text{Fe}$  yield to be in two primary

parts,  $\alpha_1$ , which is always present, and  $\alpha_2$ , which turns on at a certain total metallicity. The example code `compute_species_mass_fraction_with_user_function` computes species gas mass fractions with that parameterization, so we type (on one line)

```
./compute_species_mass_fraction_with_user_function 1 0.1 0.21117 0.0233889 fe56 0.3.989e-4 3.889e-3 2.e-2 1.2e-2 > fe56.txt
```

We obtained  $\alpha_1 = 3.989\text{e-}4$  and  $\alpha_2 = 3.889\text{e-}3$  for the metallicity break  $2.\text{e-}2$  and width  $1.\text{e-}2$  by repeated trial. With these parameters, the resulting  $[\text{O}/\text{Fe}]$  vs.  $[\text{Fe}/\text{H}]$  from our calculation matches the data in Bensby et al. (2004) fairly well, and we achieve the Solar System  $^{56}\text{Fe}$  mass fraction of  $1.17\text{e-}3$  at 8 Gyr, as required.

## 9) Get Help

Should you need help with `wn_simple_gce`, we suggest you post a question at

<http://sourceforge.net/p/wn-simple-gce/discussion/>

We will respond as soon as we can.

## References

- Bensby, T., Feltzing, S., and Lundström, I. 2004, *Oxygen trends in the Galactic thin and thick disks*, Astron. Astrophys., 415, 155-170.
- Boissier, S. and Prantzos, N. 1999, *Chemo-spectrophotometric evolution of spiral galaxies - I. The model and the Milky Way*, Monthly Not. Roy. Astr. Soc., 307, 857-876.
- Prantzos, N. and Silk, J. 1998, *Star Formation and Chemical Evolution in the Milky Way: Cosmological Implications*, Astrophys. J., 557, 229-240.
- Weaver, S. E. and Weaver, T. A. 1996, *The Evolution and Explosion of Massive Stars. II. Explosive Hydrodynamics and Nucleosynthesis*, Astrophys. J. Suppl., 101, 181-235.

## Appendix 2: Useable thermal data for exoplanet models

**Table A2.1.** Radiogenic heat production rates for cosmochemically Earth-like exoplanets.

Age Today (Gyr)	<sup>40</sup> K (W kg <sup>-1</sup> )	<sup>232</sup> Th (W kg <sup>-1</sup> )	<sup>235</sup> U (W kg <sup>-1</sup> )	<sup>238</sup> U (W kg <sup>-1</sup> )	Total (W kg <sup>-1</sup> )
12.5					
12.4	1.24E-14	2.62E-12	2.12E-16	1.31E-12	3.94E-12
12.3	1.32E-14	2.63E-12	2.25E-16	1.32E-12	3.97E-12
12.2	1.40E-14	2.64E-12	2.40E-16	1.33E-12	3.99E-12
12.1	1.48E-14	2.65E-12	2.56E-16	1.35E-12	4.01E-12
12	1.58E-14	2.66E-12	2.74E-16	1.36E-12	4.03E-12
11.9	1.67E-14	2.66E-12	2.93E-16	1.37E-12	4.05E-12
11.8	1.78E-14	2.67E-12	3.14E-16	1.39E-12	4.08E-12
11.7	1.88E-14	2.68E-12	3.36E-16	1.40E-12	4.10E-12
11.6	2.00E-14	2.69E-12	3.60E-16	1.42E-12	4.13E-12
11.5	2.12E-14	2.70E-12	3.87E-16	1.43E-12	4.15E-12
11.4	2.25E-14	2.71E-12	4.15E-16	1.45E-12	4.17E-12
11.3	2.39E-14	2.71E-12	4.46E-16	1.46E-12	4.20E-12
11.2	2.53E-14	2.72E-12	4.79E-16	1.48E-12	4.22E-12
11.1	2.68E-14	2.73E-12	5.15E-16	1.49E-12	4.25E-12
11	2.84E-14	2.74E-12	5.54E-16	1.51E-12	4.28E-12
10.9	3.02E-14	2.75E-12	5.96E-16	1.52E-12	4.30E-12
10.8	3.20E-14	2.76E-12	6.41E-16	1.54E-12	4.33E-12
10.7	3.39E-14	2.77E-12	6.90E-16	1.55E-12	4.35E-12
10.6	3.59E-14	2.77E-12	7.44E-16	1.57E-12	4.38E-12
10.5	3.81E-14	2.78E-12	8.01E-16	1.59E-12	4.41E-12



10.4	4.03E-14	2.79E-12	8.64E-16	1.60E-12	4.43E-12
10.3	4.27E-14	2.80E-12	9.31E-16	1.62E-12	4.46E-12
10.2	4.53E-14	2.81E-12	1.00E-15	1.64E-12	4.49E-12
10.1	4.79E-14	2.82E-12	1.08E-15	1.65E-12	4.52E-12
10	5.08E-14	2.83E-12	1.17E-15	1.67E-12	4.55E-12
9.9	5.38E-14	2.83E-12	1.26E-15	1.69E-12	4.58E-12
9.8	5.70E-14	2.84E-12	1.37E-15	1.70E-12	4.61E-12
9.7	6.04E-14	2.85E-12	1.48E-15	1.72E-12	4.64E-12
9.6	6.39E-14	2.86E-12	1.59E-15	1.74E-12	4.67E-12
9.5	6.77E-14	2.87E-12	1.72E-15	1.76E-12	4.70E-12
9.4	7.17E-14	2.88E-12	1.87E-15	1.78E-12	4.73E-12
9.3	7.59E-14	2.89E-12	2.02E-15	1.80E-12	4.76E-12
9.2	8.03E-14	2.89E-12	2.18E-15	1.81E-12	4.79E-12
9.1	8.51E-14	2.90E-12	2.36E-15	1.83E-12	4.82E-12
9	9.00E-14	2.91E-12	2.56E-15	1.85E-12	4.86E-12
8.9	9.53E-14	2.92E-12	2.77E-15	1.87E-12	4.89E-12
8.8	1.01E-13	2.93E-12	3.00E-15	1.89E-12	4.92E-12
8.7	1.07E-13	2.94E-12	3.25E-15	1.91E-12	4.96E-12
8.6	1.13E-13	2.94E-12	3.53E-15	1.93E-12	4.99E-12
8.5	1.20E-13	2.95E-12	3.82E-15	1.95E-12	5.03E-12
8.4	1.27E-13	2.96E-12	4.15E-15	1.97E-12	5.06E-12
8.3	1.34E-13	2.97E-12	4.50E-15	1.99E-12	5.10E-12
8.2	1.42E-13	2.98E-12	4.88E-15	2.01E-12	5.14E-12
8.1	1.50E-13	2.99E-12	5.29E-15	2.03E-12	5.17E-12
8	1.59E-13	2.99E-12	5.74E-15	2.05E-12	5.21E-12
7.9	1.68E-13	3.00E-12	6.23E-15	2.08E-12	5.25E-12
7.8	1.78E-13	3.01E-12	6.77E-15	2.10E-12	5.29E-12
7.7	1.88E-13	3.02E-12	7.35E-15	2.12E-12	5.33E-12
7.6	1.99E-13	3.03E-12	7.98E-15	2.14E-12	5.37E-12
7.5	2.10E-13	3.04E-12	8.67E-15	2.16E-12	5.42E-12
7.4	2.22E-13	3.04E-12	9.42E-15	2.19E-12	5.46E-12
7.3	2.35E-13	3.05E-12	1.02E-14	2.21E-12	5.50E-12
7.2	2.49E-13	3.06E-12	1.11E-14	2.23E-12	5.55E-12
7.1	2.63E-13	3.07E-12	1.21E-14	2.25E-12	5.60E-12
7	2.78E-13	3.08E-12	1.32E-14	2.28E-12	5.64E-12
6.9	2.94E-13	3.08E-12	1.43E-14	2.30E-12	5.69E-12
6.8	3.11E-13	3.09E-12	1.56E-14	2.32E-12	5.74E-12
6.7	3.29E-13	3.10E-12	1.69E-14	2.35E-12	5.79E-12
6.6	3.48E-13	3.11E-12	1.84E-14	2.37E-12	5.85E-12
6.5	3.68E-13	3.12E-12	2.00E-14	2.40E-12	5.90E-12
6.4	3.89E-13	3.12E-12	2.18E-14	2.42E-12	5.96E-12
6.3	4.11E-13	3.13E-12	2.37E-14	2.45E-12	6.01E-12
6.2	4.34E-13	3.14E-12	2.58E-14	2.47E-12	6.07E-12

6.1	4.59E-13	3.15E-12	2.81E-14	2.50E-12	6.13E-12
6	4.86E-13	3.15E-12	3.06E-14	2.52E-12	6.19E-12
5.9	5.13E-13	3.16E-12	3.33E-14	2.55E-12	6.26E-12
5.8	5.43E-13	3.17E-12	3.63E-14	2.57E-12	6.32E-12
5.7	5.74E-13	3.18E-12	3.95E-14	2.60E-12	6.39E-12
5.6	6.06E-13	3.19E-12	4.31E-14	2.63E-12	6.46E-12
5.5	6.41E-13	3.19E-12	4.69E-14	2.65E-12	6.54E-12
5.4	6.77E-13	3.20E-12	5.11E-14	2.68E-12	6.61E-12
5.3	7.16E-13	3.21E-12	5.57E-14	2.71E-12	6.69E-12
5.2	7.56E-13	3.22E-12	6.07E-14	2.74E-12	6.77E-12
5.1	7.99E-13	3.22E-12	6.62E-14	2.77E-12	6.85E-12
5	8.45E-13	3.23E-12	7.22E-14	2.79E-12	6.94E-12
4.9	8.93E-13	3.24E-12	7.87E-14	2.82E-12	7.03E-12
4.8	9.43E-13	3.25E-12	8.58E-14	2.85E-12	7.13E-12
4.7	9.97E-13	3.25E-12	9.35E-14	2.88E-12	7.22E-12
4.6	1.05E-12	3.26E-12	1.02E-13	2.91E-12	7.33E-12
4.5	1.11E-12	3.27E-12	1.11E-13	2.94E-12	7.43E-12
4.4	1.18E-12	3.28E-12	1.21E-13	2.97E-12	7.54E-12
4.3	1.24E-12	3.28E-12	1.32E-13	3.00E-12	7.66E-12
4.2	1.31E-12	3.29E-12	1.44E-13	3.03E-12	7.78E-12
4.1	1.39E-12	3.30E-12	1.58E-13	3.06E-12	7.91E-12
4	1.47E-12	3.31E-12	1.72E-13	3.09E-12	8.04E-12
3.9	1.55E-12	3.31E-12	1.88E-13	3.13E-12	8.18E-12
3.8	1.64E-12	3.32E-12	2.05E-13	3.16E-12	8.32E-12
3.7	1.73E-12	3.33E-12	2.23E-13	3.19E-12	8.47E-12
3.6	1.83E-12	3.34E-12	2.44E-13	3.22E-12	8.63E-12
3.5	1.93E-12	3.34E-12	2.66E-13	3.26E-12	8.80E-12
3.4	2.04E-12	3.35E-12	2.91E-13	3.29E-12	8.97E-12
3.3	2.15E-12	3.36E-12	3.17E-13	3.32E-12	9.15E-12
3.2	2.28E-12	3.37E-12	3.47E-13	3.36E-12	9.35E-12
3.1	2.40E-12	3.37E-12	3.78E-13	3.39E-12	9.55E-12
3	2.54E-12	3.38E-12	4.13E-13	3.43E-12	9.76E-12
2.9	2.68E-12	3.39E-12	4.51E-13	3.46E-12	9.99E-12
2.8	2.83E-12	3.40E-12	4.93E-13	3.50E-12	1.02E-11
2.7	2.99E-12	3.40E-12	5.38E-13	3.54E-12	1.05E-11
2.6	3.16E-12	3.41E-12	5.88E-13	3.57E-12	1.07E-11
2.5	3.34E-12	3.42E-12	6.43E-13	3.61E-12	1.10E-11
2.4	3.53E-12	3.43E-12	7.02E-13	3.65E-12	1.13E-11
2.3	3.73E-12	3.43E-12	7.67E-13	3.69E-12	1.16E-11
2.2	3.94E-12	3.44E-12	8.39E-13	3.72E-12	1.19E-11
2.1	4.16E-12	3.45E-12	9.16E-13	3.76E-12	1.23E-11
2	4.40E-12	3.46E-12	1.00E-12	3.80E-12	1.27E-11
1.9	4.64E-12	3.47E-12	1.09E-12	3.84E-12	1.30E-11

1.8	4.91E-12	3.47E-12	1.20E-12	3.88E-12	1.35E-11
1.7	5.18E-12	3.48E-12	1.31E-12	3.92E-12	1.39E-11
1.6	5.47E-12	3.49E-12	1.43E-12	3.96E-12	1.44E-11
1.5	5.78E-12	3.50E-12	1.56E-12	4.01E-12	1.49E-11
1.4	6.11E-12	3.51E-12	1.71E-12	4.05E-12	1.54E-11
1.3	6.45E-12	3.51E-12	1.87E-12	4.09E-12	1.59E-11
1.2	6.82E-12	3.52E-12	2.04E-12	4.14E-12	1.65E-11
1.1	7.20E-12	3.53E-12	2.24E-12	4.18E-12	1.71E-11
1	7.61E-12	3.54E-12	2.45E-12	4.22E-12	1.78E-11
0.9	8.04E-12	3.55E-12	2.67E-12	4.27E-12	1.85E-11
0.8	8.49E-12	3.55E-12	2.93E-12	4.31E-12	1.93E-11
0.7	8.97E-12	3.56E-12	3.20E-12	4.36E-12	2.01E-11
0.6	9.47E-12	3.57E-12	3.50E-12	4.41E-12	2.10E-11
0.5	1.00E-11	3.58E-12	3.83E-12	4.45E-12	2.19E-11
0.4	1.06E-11	3.59E-12	4.19E-12	4.50E-12	2.29E-11
0.3	1.12E-11	3.60E-12	4.59E-12	4.55E-12	2.39E-11
0.2	1.18E-11	3.61E-12	5.02E-12	4.60E-12	2.50E-11
0.1	1.25E-11	3.62E-12	5.49E-12	4.65E-12	2.62E-11
0	1.32E-11	3.62E-12	6.01E-12	4.70E-12	2.75E-11

**Table A2.2.** Heat production rates in cosmochemically Earth-like planets at the time of their formation in galactic history.

Time after galaxy formation (Gyr)	$^{40}\text{K}$ (W kg $^{-1}$ )	$^{232}\text{Th}$ (W kg $^{-1}$ )	$^{235}\text{U}$ (W kg $^{-1}$ )	$^{238}\text{U}$ (W kg $^{-1}$ )	Total (W kg $^{-1}$ )
0.0					
0.1	1.21E-11	4.84E-12	4.27E-11	8.94E-12	6.85E-11
0.2	1.21E-11	4.83E-12	4.11E-11	8.88E-12	6.69E-11
0.3	1.22E-11	4.82E-12	3.97E-11	8.83E-12	6.55E-11
0.4	1.22E-11	4.81E-12	3.84E-11	8.78E-12	6.43E-11
0.5	1.23E-11	4.80E-12	3.72E-11	8.73E-12	6.31E-11
0.6	1.24E-11	4.79E-12	3.61E-11	8.69E-12	6.19E-11
0.7	1.24E-11	4.78E-12	3.50E-11	8.64E-12	6.09E-11
0.8	1.25E-11	4.77E-12	3.40E-11	8.59E-12	5.98E-11
0.9	1.25E-11	4.76E-12	3.30E-11	8.55E-12	5.89E-11
1.0	1.25E-11	4.76E-12	3.21E-11	8.50E-12	5.79E-11
1.1	1.26E-11	4.75E-12	3.12E-11	8.46E-12	5.70E-11
1.2	1.26E-11	4.74E-12	3.04E-11	8.42E-12	5.62E-11
1.3	1.27E-11	4.73E-12	2.96E-11	8.37E-12	5.54E-11
1.4	1.27E-11	4.72E-12	2.88E-11	8.33E-12	5.46E-11
1.5	1.27E-11	4.71E-12	2.81E-11	8.28E-12	5.38E-11
1.6	1.28E-11	4.70E-12	2.74E-11	8.24E-12	5.31E-11
1.7	1.28E-11	4.70E-12	2.67E-11	8.20E-12	5.24E-11
1.8	1.29E-11	4.69E-12	2.61E-11	8.16E-12	5.18E-11
1.9	1.29E-11	4.68E-12	2.55E-11	8.11E-12	5.11E-11
2.0	1.29E-11	4.67E-12	2.49E-11	8.07E-12	5.05E-11
2.1	1.29E-11	4.66E-12	2.43E-11	8.03E-12	4.99E-11
2.2	1.30E-11	4.65E-12	2.37E-11	7.99E-12	4.94E-11
2.3	1.30E-11	4.64E-12	2.32E-11	7.95E-12	4.88E-11
2.4	1.30E-11	4.63E-12	2.27E-11	7.91E-12	4.83E-11
2.5	1.31E-11	4.63E-12	2.22E-11	7.87E-12	4.78E-11
2.6	1.31E-11	4.62E-12	2.17E-11	7.83E-12	4.73E-11
2.7	1.31E-11	4.61E-12	2.13E-11	7.79E-12	4.68E-11
2.8	1.31E-11	4.60E-12	2.08E-11	7.75E-12	4.63E-11
2.9	1.32E-11	4.59E-12	2.04E-11	7.71E-12	4.59E-11
3.0	1.32E-11	4.58E-12	2.00E-11	7.67E-12	4.54E-11
3.1	1.32E-11	4.57E-12	1.96E-11	7.63E-12	4.50E-11
3.2	1.32E-11	4.56E-12	1.92E-11	7.59E-12	4.46E-11
3.3	1.33E-11	4.55E-12	1.88E-11	7.55E-12	4.42E-11
3.4	1.33E-11	4.55E-12	1.85E-11	7.51E-12	4.38E-11
3.5	1.33E-11	4.54E-12	1.81E-11	7.47E-12	4.34E-11
3.6	1.33E-11	4.53E-12	1.78E-11	7.44E-12	4.31E-11

3.7	1.33E-11	4.52E-12	1.75E-11	7.40E-12	4.27E-11
3.8	1.34E-11	4.51E-12	1.71E-11	7.36E-12	4.24E-11
3.9	1.34E-11	4.50E-12	1.68E-11	7.32E-12	4.20E-11
4.0	1.34E-11	4.49E-12	1.65E-11	7.28E-12	4.17E-11
4.1	1.34E-11	4.48E-12	1.63E-11	7.25E-12	4.14E-11
4.2	1.34E-11	4.47E-12	1.60E-11	7.21E-12	4.11E-11
4.3	1.34E-11	4.46E-12	1.57E-11	7.17E-12	4.08E-11
4.4	1.34E-11	4.45E-12	1.54E-11	7.13E-12	4.05E-11
4.5	1.34E-11	4.44E-12	1.52E-11	7.10E-12	4.02E-11
4.6	1.35E-11	4.43E-12	1.49E-11	7.06E-12	3.99E-11
4.7	1.35E-11	4.42E-12	1.47E-11	7.02E-12	3.96E-11
4.8	1.35E-11	4.41E-12	1.45E-11	6.99E-12	3.93E-11
4.9	1.35E-11	4.40E-12	1.42E-11	6.95E-12	3.91E-11
5.0	1.35E-11	4.39E-12	1.40E-11	6.92E-12	3.88E-11
5.1	1.35E-11	4.38E-12	1.38E-11	6.88E-12	3.86E-11
5.2	1.35E-11	4.37E-12	1.36E-11	6.84E-12	3.83E-11
5.3	1.35E-11	4.36E-12	1.34E-11	6.81E-12	3.81E-11
5.4	1.35E-11	4.35E-12	1.32E-11	6.77E-12	3.78E-11
5.5	1.35E-11	4.34E-12	1.30E-11	6.74E-12	3.76E-11
5.6	1.35E-11	4.33E-12	1.28E-11	6.70E-12	3.74E-11
5.7	1.35E-11	4.32E-12	1.26E-11	6.67E-12	3.71E-11
5.8	1.35E-11	4.31E-12	1.24E-11	6.63E-12	3.69E-11
5.9	1.36E-11	4.30E-12	1.23E-11	6.60E-12	3.67E-11
6.0	1.36E-11	4.29E-12	1.21E-11	6.56E-12	3.65E-11
6.1	1.36E-11	4.28E-12	1.19E-11	6.53E-12	3.63E-11
6.2	1.36E-11	4.27E-12	1.18E-11	6.50E-12	3.61E-11
6.3	1.36E-11	4.26E-12	1.16E-11	6.46E-12	3.59E-11
6.4	1.36E-11	4.25E-12	1.14E-11	6.43E-12	3.57E-11
6.5	1.36E-11	4.24E-12	1.13E-11	6.39E-12	3.55E-11
6.6	1.36E-11	4.23E-12	1.11E-11	6.36E-12	3.53E-11
6.7	1.36E-11	4.22E-12	1.10E-11	6.33E-12	3.51E-11
6.8	1.36E-11	4.21E-12	1.08E-11	6.29E-12	3.49E-11
6.9	1.36E-11	4.20E-12	1.07E-11	6.26E-12	3.47E-11
7.0	1.36E-11	4.19E-12	1.06E-11	6.23E-12	3.46E-11
7.1	1.36E-11	4.18E-12	1.04E-11	6.19E-12	3.44E-11
7.2	1.36E-11	4.17E-12	1.03E-11	6.16E-12	3.42E-11
7.3	1.36E-11	4.16E-12	1.02E-11	6.13E-12	3.40E-11
7.4	1.36E-11	4.14E-12	1.01E-11	6.10E-12	3.39E-11
7.5	1.35E-11	4.13E-12	9.93E-12	6.06E-12	3.37E-11
7.6	1.35E-11	4.12E-12	9.81E-12	6.03E-12	3.35E-11
7.7	1.35E-11	4.11E-12	9.70E-12	6.00E-12	3.34E-11
7.8	1.35E-11	4.10E-12	9.58E-12	5.97E-12	3.32E-11
7.9	1.35E-11	4.09E-12	9.47E-12	5.94E-12	3.30E-11

8.0	1.35E-11	4.08E-12	9.36E-12	5.91E-12	3.29E-11
8.1	1.35E-11	4.07E-12	9.25E-12	5.87E-12	3.27E-11
8.2	1.35E-11	4.06E-12	9.14E-12	5.84E-12	3.26E-11
8.3	1.35E-11	4.05E-12	9.04E-12	5.81E-12	3.24E-11
8.4	1.35E-11	4.04E-12	8.94E-12	5.78E-12	3.23E-11
8.5	1.35E-11	4.03E-12	8.84E-12	5.75E-12	3.21E-11
8.6	1.35E-11	4.02E-12	8.74E-12	5.72E-12	3.20E-11
8.7	1.35E-11	4.00E-12	8.64E-12	5.69E-12	3.18E-11
8.8	1.35E-11	3.99E-12	8.55E-12	5.66E-12	3.17E-11
8.9	1.35E-11	3.98E-12	8.46E-12	5.63E-12	3.15E-11
9.0	1.35E-11	3.97E-12	8.37E-12	5.60E-12	3.14E-11
9.1	1.35E-11	3.96E-12	8.28E-12	5.57E-12	3.13E-11
9.2	1.35E-11	3.95E-12	8.19E-12	5.54E-12	3.11E-11
9.3	1.34E-11	3.94E-12	8.10E-12	5.52E-12	3.10E-11
9.4	1.34E-11	3.93E-12	8.02E-12	5.49E-12	3.09E-11
9.5	1.34E-11	3.92E-12	7.93E-12	5.46E-12	3.07E-11
9.6	1.34E-11	3.91E-12	7.85E-12	5.43E-12	3.06E-11
9.7	1.34E-11	3.90E-12	7.77E-12	5.40E-12	3.05E-11
9.8	1.34E-11	3.89E-12	7.69E-12	5.37E-12	3.04E-11
9.9	1.34E-11	3.88E-12	7.62E-12	5.35E-12	3.02E-11
10.0	1.34E-11	3.87E-12	7.54E-12	5.32E-12	3.01E-11
10.1	1.34E-11	3.86E-12	7.47E-12	5.29E-12	3.00E-11
10.2	1.34E-11	3.85E-12	7.39E-12	5.26E-12	2.99E-11
10.3	1.34E-11	3.84E-12	7.32E-12	5.24E-12	2.98E-11
10.4	1.34E-11	3.83E-12	7.25E-12	5.21E-12	2.96E-11
10.5	1.33E-11	3.82E-12	7.18E-12	5.18E-12	2.95E-11
10.6	1.33E-11	3.81E-12	7.11E-12	5.16E-12	2.94E-11
10.7	1.33E-11	3.80E-12	7.05E-12	5.13E-12	2.93E-11
10.8	1.33E-11	3.79E-12	6.98E-12	5.11E-12	2.92E-11
10.9	1.33E-11	3.78E-12	6.92E-12	5.08E-12	2.91E-11
11.0	1.33E-11	3.77E-12	6.85E-12	5.06E-12	2.90E-11
11.1	1.33E-11	3.76E-12	6.79E-12	5.03E-12	2.89E-11
11.2	1.33E-11	3.75E-12	6.73E-12	5.01E-12	2.88E-11
11.3	1.33E-11	3.74E-12	6.67E-12	4.98E-12	2.87E-11
11.4	1.33E-11	3.73E-12	6.61E-12	4.96E-12	2.86E-11
11.5	1.33E-11	3.72E-12	6.55E-12	4.93E-12	2.84E-11
11.6	1.32E-11	3.71E-12	6.49E-12	4.91E-12	2.83E-11
11.7	1.32E-11	3.70E-12	6.43E-12	4.88E-12	2.83E-11
11.8	1.32E-11	3.69E-12	6.38E-12	4.86E-12	2.82E-11
11.9	1.32E-11	3.68E-12	6.32E-12	4.84E-12	2.81E-11
12.0	1.32E-11	3.67E-12	6.27E-12	4.81E-12	2.80E-11
12.1	1.32E-11	3.66E-12	6.22E-12	4.79E-12	2.79E-11
12.2	1.32E-11	3.65E-12	6.16E-12	4.77E-12	2.78E-11

12.3	1.32E-11	3.64E-12	6.11E-12	4.75E-12	2.77E-11
12.4	1.32E-11	3.63E-12	6.06E-12	4.72E-12	2.76E-11
12.5	1.32E-11	3.62E-12	6.01E-12	4.70E-12	2.75E-11
12.6	1.32E-11	3.62E-12	5.96E-12	4.68E-12	2.74E-11
12.7	1.32E-11	3.61E-12	5.92E-12	4.66E-12	2.73E-11
12.8	1.31E-11	3.60E-12	5.87E-12	4.63E-12	2.72E-11
12.9	1.31E-11	3.59E-12	5.82E-12	4.61E-12	2.72E-11
13.0	1.31E-11	3.58E-12	5.77E-12	4.59E-12	2.71E-11
13.1	1.31E-11	3.57E-12	5.73E-12	4.57E-12	2.70E-11
13.2	1.31E-11	3.56E-12	5.68E-12	4.55E-12	2.69E-11
13.3	1.31E-11	3.55E-12	5.64E-12	4.53E-12	2.68E-11
13.4	1.31E-11	3.55E-12	5.60E-12	4.51E-12	2.68E-11
13.5	1.31E-11	3.54E-12	5.55E-12	4.49E-12	2.67E-11
13.6	1.31E-11	3.53E-12	5.51E-12	4.47E-12	2.66E-11
13.7	1.31E-11	3.52E-12	5.47E-12	4.45E-12	2.65E-11
13.8	1.31E-11	3.51E-12	5.43E-12	4.43E-12	2.64E-11
13.9	1.31E-11	3.51E-12	5.39E-12	4.41E-12	2.64E-11
14.0	1.31E-11	3.50E-12	5.35E-12	4.39E-12	2.63E-11
14.1	1.30E-11	3.49E-12	5.31E-12	4.37E-12	2.62E-11
14.2	1.30E-11	3.48E-12	5.27E-12	4.35E-12	2.62E-11
14.3	1.30E-11	3.47E-12	5.24E-12	4.33E-12	2.61E-11
14.4	1.30E-11	3.47E-12	5.20E-12	4.31E-12	2.60E-11
14.5	1.30E-11	3.46E-12	5.16E-12	4.30E-12	2.59E-11
14.6	1.30E-11	3.45E-12	5.12E-12	4.28E-12	2.59E-11
14.7	1.30E-11	3.44E-12	5.09E-12	4.26E-12	2.58E-11
14.8	1.30E-11	3.44E-12	5.05E-12	4.24E-12	2.57E-11
14.9	1.30E-11	3.43E-12	5.02E-12	4.22E-12	2.57E-11
15.0	1.30E-11	3.42E-12	4.98E-12	4.21E-12	2.56E-11
15.1	1.30E-11	3.41E-12	4.95E-12	4.19E-12	2.55E-11
15.2	1.30E-11	3.41E-12	4.92E-12	4.17E-12	2.55E-11
15.3	1.30E-11	3.40E-12	4.88E-12	4.15E-12	2.54E-11
15.4	1.30E-11	3.39E-12	4.85E-12	4.14E-12	2.54E-11
15.5	1.30E-11	3.39E-12	4.82E-12	4.12E-12	2.53E-11
15.6	1.30E-11	3.38E-12	4.79E-12	4.10E-12	2.52E-11
15.7	1.30E-11	3.37E-12	4.76E-12	4.09E-12	2.52E-11
15.8	1.30E-11	3.36E-12	4.73E-12	4.07E-12	2.51E-11
15.9	1.30E-11	3.36E-12	4.70E-12	4.05E-12	2.51E-11
16.0	1.29E-11	3.35E-12	4.67E-12	4.04E-12	2.50E-11
16.1	1.29E-11	3.34E-12	4.64E-12	4.02E-12	2.50E-11
16.2	1.29E-11	3.34E-12	4.61E-12	4.01E-12	2.49E-11
16.3	1.29E-11	3.33E-12	4.58E-12	3.99E-12	2.48E-11
16.4	1.29E-11	3.32E-12	4.55E-12	3.97E-12	2.48E-11
16.5	1.29E-11	3.32E-12	4.52E-12	3.96E-12	2.47E-11

16.6	1.29E-11	3.31E-12	4.49E-12	3.94E-12	2.47E-11
16.7	1.29E-11	3.30E-12	4.47E-12	3.93E-12	2.46E-11
16.8	1.29E-11	3.30E-12	4.44E-12	3.91E-12	2.46E-11
16.9	1.29E-11	3.29E-12	4.41E-12	3.90E-12	2.45E-11
17.0	1.29E-11	3.29E-12	4.39E-12	3.88E-12	2.45E-11
17.1	1.29E-11	3.28E-12	4.36E-12	3.87E-12	2.44E-11
17.2	1.29E-11	3.27E-12	4.33E-12	3.85E-12	2.44E-11
17.3	1.29E-11	3.27E-12	4.31E-12	3.84E-12	2.43E-11
17.4	1.29E-11	3.26E-12	4.28E-12	3.82E-12	2.43E-11
17.5	1.29E-11	3.25E-12	4.26E-12	3.81E-12	2.42E-11
17.6	1.29E-11	3.25E-12	4.23E-12	3.80E-12	2.42E-11
17.7	1.29E-11	3.24E-12	4.21E-12	3.78E-12	2.41E-11
17.8	1.29E-11	3.24E-12	4.19E-12	3.77E-12	2.41E-11
17.9	1.29E-11	3.23E-12	4.16E-12	3.75E-12	2.40E-11
18.0	1.29E-11	3.22E-12	4.14E-12	3.74E-12	2.40E-11
18.1	1.29E-11	3.22E-12	4.12E-12	3.73E-12	2.39E-11
18.2	1.29E-11	3.21E-12	4.09E-12	3.71E-12	2.39E-11
18.3	1.29E-11	3.21E-12	4.07E-12	3.70E-12	2.38E-11
18.4	1.29E-11	3.20E-12	4.05E-12	3.69E-12	2.38E-11
18.5	1.29E-11	3.20E-12	4.03E-12	3.67E-12	2.38E-11
18.6	1.29E-11	3.19E-12	4.00E-12	3.66E-12	2.37E-11
18.7	1.29E-11	3.18E-12	3.98E-12	3.65E-12	2.37E-11
18.8	1.29E-11	3.18E-12	3.96E-12	3.63E-12	2.36E-11
18.9	1.29E-11	3.17E-12	3.94E-12	3.62E-12	2.36E-11
19.0	1.28E-11	3.17E-12	3.92E-12	3.61E-12	2.35E-11
19.1	1.29E-11	3.16E-12	3.90E-12	3.59E-12	2.35E-11
19.2	1.28E-11	3.16E-12	3.88E-12	3.58E-12	2.35E-11
19.3	1.28E-11	3.15E-12	3.86E-12	3.57E-12	2.34E-11
19.4	1.28E-11	3.14E-12	3.84E-12	3.56E-12	2.34E-11
19.5	1.28E-11	3.14E-12	3.82E-12	3.54E-12	2.33E-11
19.6	1.28E-11	3.13E-12	3.80E-12	3.53E-12	2.33E-11
19.7	1.28E-11	3.13E-12	3.78E-12	3.52E-12	2.33E-11
19.8	1.28E-11	3.12E-12	3.76E-12	3.51E-12	2.32E-11
19.9	1.28E-11	3.12E-12	3.74E-12	3.50E-12	2.32E-11
20.0	1.28E-11	3.11E-12	3.72E-12	3.48E-12	2.31E-11